Customer	**:**	**ESRIN**	**Document Ref**	**:**	**SST_CCI-ATBD-UOR-203**
Contract No	**:**	**4000109848/13/I-NB**	**Issue Date**	**:**	**6 May 2019**
WP No	**:**	**30**	**Issue**	**:**	**3**

Project : **SST-CCI-Phase-II**

Title : **Algorithm Theoretical Basis Document (v2 Reprocessing)**

Abstract : This is the Algorithm Theoretical Basis Document (ATBD) for the Sea Surface Temperature Climate Change Initiative project. This version covers the principles of algorithms selected within the project to obtain sea surface temperature (SST), in terms of retrieval of skin SST from satellite radiances, physically based estimation of SST depth, and analysis (interpolation) of SST to spatially complete products.

This ATBD corresponds to the algorithms underpinning v2.0 and v2.1.

Author : C J Merchant
and SST CCI team

Checked : Hugh Kelliher
Space Connexions Ltd

esa
Digitally signed by Craig Donlon
Date: 2019.07.04 10:44:27 +02'00'

Accepted : Craig Donlon
ESA

Distribution : SST_cci team members

Craig Donlon (ESA)

EUROPEAN SPACE AGENCY
CONTRACT REPORT

The work described in this report was done under ESA contract. Responsibility for the contents resides in the author or organisation that prepared it.

AMENDMENT RECORD

This document shall be amended by releasing a new edition of the document in its entirety. The Amendment Record Sheet below records the history and issue status of this document.

AMENDMENT RECORD SHEET

ISSUE	DATE	REASON FOR CHANGE
A	31-01-15	1st draft issue for internal review.
B	06-05-15	2nd draft issue for internal review, with new ATSR algorithms.
C	15-05-15	3rd draft issue for review by ESA.
1	04-08-15	First issue incorporating ESA comments.
1A	04-03-16	Draft second issue 1A. New section 6.2 and 6.3 edits.
2	21-04-16	Second issue incorporating ESA comments.
2A	28-02-19	Draft third issue. Updates for version 2.1.
3	06-06-19	Third issue incorporating ESA comments.

TABLE OF CONTENTS

1. INTRODUCTION

1.1 Purpose and Scope

This Algorithm Theoretical Basis Document (ATBD) describes and justifies the algorithms used for obtaining sea surface temperature (SST) estimates within the ESA SST Climate Change Initiative project's prototype processor, as configured for the version 2 (v2) climate data records generated at the end of SST CCI Phase II.

Relative to the previous ATBD (addressing the mid-Phase reprocessing), this report includes the following:

- Updated quality and cloud thresholds for v2
- Updated SST-level harmonisation description for AVHRR SSTs
- Section describing improved uncertainty propagation to L4 and improved L4 analysis method
- Updates to information where needed throughout

1.2 Referenced Documents

The following is a list of documents with a direct bearing on the content of this report. Where referenced in the text, these are identified as RD.n, where 'n' is the number in the list below:

RD.38 Berrisford, P., et al (2009), The ERA-Interim archive, European Centre for Medium Range Weather Forecasts, Reading.

RD.43 Eastwood S., K. R. Larsen, T. Lavergne, E. Nielsen, and R. Tonboe (2010), Global Sea Ice Concentration Reprocessing Product User Manual, Met Norway/Danish Meteorological Institute, EUMETSAT Ocean and Sea Ice SAF.

RD.175 CCI Phase 1 (SST), Product Specification Document

RD.181 Merchant C J, C P Old, O Embury and S N MacCallum (2008), Generalized Bayesian Cloud Screening: Algorithm Theoretical Basis version 2.1, School of GeoSciences, University of Edinburgh. Available from: http://www.geos.ed.ac.uk/gbcs/ATBv2.1c.pdf and via http://www.esa-sst-cci.org

RD.184 Embury, O., C. J. Merchant and G. K. Corlett (2012), A Reprocessing for Climate of Sea Surface Temperature from the Along-Track Scanning Radiometers: Initial validation, accounting for skin and diurnal variability, Rem. Sens. Env., pp62 - 78. DOI:10.1016/j.rse.2011.02.028

RD.185 Embury, O. and C. J. Merchant (2012), A Reprocessing for Climate of Sea Surface Temperature from the Along-Track Scanning Radiometers: A New Retrieval Scheme, Rem. Sens. Env., pp 47 - 61, DOI: 10.1016/j.rse.2010.11.020

RD.186 Embury, O., C. J. Merchant and M. J. Filipiak (2012), A Reprocessing for Climate of Sea Surface Temperature from the Along-Track Scanning Radiometers: Basis in Radiative Transfer, Rem. Sens. Env., pp32 - 46, DOI: 10.1016/j.rse.2010.10.016

RD.213 Donlon, C.J., M. Martin, J. Stark, J. Roberts-Jones, E. Fiedler and W. Wimmer (2012). The Operational Sea Surface Temperature and Sea Ice Analysis (OSTIA) system, Remote Sensing of the Environment, 116, 140-158.

RD.221 Merchant C J, P Le Borgne, A Marsouin and H Roquet (2008), Optimal estimation of sea surface temperature from split-window observations, Rem. Sens. Env., 112 (5), 2469-2484. doi:10.1016/j.rse.2007.11.011

RD.222 Gentemann, C. L., P. J. Minnett, and B. Ward (2009), Profiles of ocean surface heating (POSH): A new model of upper ocean diurnal warming, J. Geophys. Res., 114, C07017, doi:10.1029/2008JC004825.

RD.226 MacCallum and Merchant (2012), SST CCI Algorithm Selection Report, http://www.esa-sst-cci.org

RD.227 Fairall, C., E. Bradley, J. Godfrey, G. Wick, J. Edson, and G. Young (1996), Cool-skin and warm-layer effects on sea surface temperature, J. Geophys. Res., 101(C1), 1295-1308.

RD.231 CLAVR-X installation instructions, https://groups.ssec.wisc.edu/users/wstraka/aix-clavr-x-code/installing-clavr-x-on-your-own-machine

RD.232 SST_CCI Multi-sensor Match-up Dataset Specification, SST_CCI-REP-UoL-001

RD.239 Roberts-Jones, J., Fiedler, E. K. and M. Martin (2012), Daily, global, high-resolution SST and sea-ice reanalysis for 1985-2007 using the OSTIA system, J. Climate, doi:10.1175/JCLI-D-11-00648.1, in press.

RD.253 Merchant, C. J., & Le Borgne, P. (2004). Retrieval of sea surface temperature from space based on modeling of infrared radiative transfer: Capabilities and limitations. *Journal of Atmospheric and Oceanic Technology*, 22(11), 1734−1746.

RD.262 Horrocks L. A., Candy B., Nightingale T. J., Saunders R. W., O'Carroll A., and Harris A. R., Parameterisations of the ocean skin effect and implications for satellite-based measurement of sea surface temperature. J. Geophys. Res., Vol. 108(C3), 3096, doi:10.1029/2002JC001503, 2003

RD.263 Kantha L.H., and Clayson C.A., An improved mixed layer model for geophysical applications. J. Geophys. Res. Vol. 99 (C12), 25235–25266, 1994.

RD.264 Lisa A. Horrocks, Andrew R. Harris, and Roger W. Saunders, Modelling the diurnal thermocline for daytime bulk SST from AATSR, NWP FRTR No. 418, UKMO, 2003.

RD.265 Gentemann, C. L., P. J. Minnett, P. Le Borgne, and C. J. Merchant (2008), Multi-satellite measurements of large diurnal warming events, Geophys. Res. Lett., 35, L22602, doi:10.1029/2008GL035730.

RD.266 Mark Filipiak, Diurnal Adjustment Model Selection, 2010

RD.273 Merchant C J, Algorithm Theoretical Basis Document 0, 2012, SST-CCI-ATBDv0-UOE-004-Issue 1 (Accept-Signed).pdf

RD.274 Killie, M. A., Ø. Godøy, S. Eastwood and T. Lavergne: ATBD for EUMETSAT OSI SAF Regional Ice Edge Product, v1.1, 2011. http://osisaf.met.no/docs/osisaf_ss2_atbd_ice-edge-reg_v1p1.pdf

RD.275 Roberts-Jones, J., Fiedler, E. K. and M. Martin (2011), Met Office Technical Report 561: Description and assessment of the OSTIA reanalysis, Met Office.

RD.276 Daley, R. (1991), Atmospheric data analysis. Cambridge University Press.

RD.278 Hollingsworth, A. and P. Lonnberg (1986). The statistical structure of short-range forecast errors as determined from radiosonde data. Part 1: The wind field. Tellus, 38A, 111-136.

RD.280 Bell, M.J., A. Hines and M.J. Martin (2003). Variational assimilation evolving individual observations and their error estimates. Met Office Ocean Applications technical note no. 32. Available from Met Office, Fitzroy Rd, Exeter, UK.

RD.294 Jonah Roberts-Jones, Emma Fiedler, Matthew Martin, Alison McLaren, Improvements to the Operational Sea Surface Temperature and Sea Ice Analysis (OSTIA) system, UKMO Tech Document SST_CCI_TN_UKMO_002

RD.295 Merchant, C. J., P. LeBorgne, H. Roquet and G. Legendre, Extended optimal estimation techniques for sea surface temperature from the Spinning Enhanced Visible and Infra--Red Imager (SEVIRI), Rem. Sens. Env., 131, 287-297, 2013, http://dx.doi.org/10.1016/j.rse.2012.12.019

RD.296 Merchant, C. J., O. Embury, N. A. Rayner, D. I. Berry, G. Corlett, K. Lean, K. L. Veal, E. C. Kent, D. Llewellyn-Jones, J. J. Remedios, and R. Saunders (2012), A twenty-year independent record of sea surface temperature for climate from Along Track Scanning Radiometers, J. Geophys. Res., 117, C12013, doi:10.1029/2012JC008400.

RD.297 Watts, PD; Allen, MR; Nightingale, TJ, (1996) Wind speed effects on sea surface emission and reflection for the Along Track Scanning Radiometer JOURNAL OF ATMOSPHERIC AND OCEANIC TECHNOLOGY Volume: 13 Issue: 1 Pages: 126-141 DOI: 10.1175/1520-0426(1996)013<0126:WSEOSS>2.0.CO;2

RD.298 Mittaz J and A Harris, A physical method for the calibration of the AVHRR/3 thermal IR channels Part II: in orbit comparison of the AVHRR longwave thermal IR channels on board MetOp-A with IASI, J Atmosph Oceanic Technol, 28, 1072, 10.1175/2011JTECHA1517.1

RD.300 Stamnes, K., SC. Tsay, W. Wiscombe and K. Jayaweera, Numerically stable algorithm for discrete-ordinate-method radiative transfer in multiple scattering and emitting layered media, Appl Opt 27 (1988) (12), pp. 2502–2509.

RD.301 Sea Surface Temperature (SLSTR) Algorithm Theoretical Basis Document, SLSTR-ATBD-L2SST-v2.4, August 2012

RD.302 Chevallier, F., Sampled databases of 60-level atmospheric profiles from the ECMWF analyses, SAF Programme: Research Report No. 4, EUMETSAT/ECMWF, 2001.

RD.303 Tobin, D. & L. L. Strow (1994) A Compilation of First-order Line-mixing Coefficients for CO2 Q-branches, J. Quant. Spectrosc. Radiat. Transfer, 52, 281.

RD.304 Deshler, T., Hervig, M.E., Hofmann, D.J., Rosen, J.M. and Liley, J.B. (2003). Thirty years of in situ stratospheric aerosol size distribution measurements from Laramie, Wyoming (41N), using balloon-borne instruments. Journal of Geophysical Research 108(D5): doi: 10.1029/2002JD002514. issn: 0148-0227

RD.306 SST CCI Uncertainty Characterisation Report v2, SST_CCI-UCR-UOE-002, 2013. Available from www.esa-sst-cci.org

RD.307 Rodgers C D, Inverse Methods for Atmospheric Sounding, World Scientific, Singapore, ISBN 981-02-2740-X, 2000.

RD.308 Bulgin C E, Eastwood S, Embury O, Merchant C J, Donlon C, (2014). The Sea Surface Temperature Climate Change Initiative: Alternative Image Classification Algorithms for Sea-Ice Affected Oceans. Remote Sensing of Environment. ISSB 0034-4257 doi:10.1016/j.rse.2013.11.022.

RD.309 Hocking J, Rayer P, Saunders R, Matricardi M, Geer A and Brunel P. RTTOV v10 Users Guide. NWP SAF, The EUMETSAT Network of Satellite Application Facilities. NWPSAF-MO-UD-023. Version 1.5. Date 12/01/2011

RD.310 Thomas S M, Heidinger, A K, Pavolonis M J, Comparison of NOAA's Operational AVHRR-Derived Cloud Amount to Other Satellite-Derived Cloud Climatologies, Journal of Climate, American Meteorological Society, Volume 17, pages 4805-4822, 2004

RD.311 Heidinger A. K., Evan A. T., Foster, M. J. and Walther, A. A Naïve Bayesian Cloud-Detection Scheme Derived from CALIPSO and Applied within PATMOS-x, Journal of Applied Meteorology and Climatology, Volume 51, Pages 1129-1144, 2012.

RD.312 NOAA Satellite and Information Service, National Environmental Satellite, Data and Information Service (NESDIS), US Department of Commerce, Camp Springs, noaasis.noaa.gov/NOAASIS/ml/avhrr.html, last modified 03/07/2013.

RD.318 Hyvärinen, O., Karlsson, K-G. and Dybbroe, A. (1999), Investigations of NOAA AVHRR/3 1.6 imagery for snow, cloud and sunglint discrimination. Nowcasting SAF Visiting scientist report, SMHI, http://www.nwcsaf.org/HD/files/vsadoc/ottohyvarinen_vsa_report_full.pdf

RD.319 Saunders, P. M., (1967), The temperature at the ocean-air interface, Journal of Atmospheric Science, 24, 269-273.

RD.320 Fillipiak, M., (2008), Refractive indices (500-3500 cm^{-1}) and emissivity (600-3350 cm^{-1}) of pure water and seawater, Dataset, http://hdl.handle.net/10283717

RD.321 Závody, A. M., Mutlow, C. T., Llewellyn-Jones, D. T., (1995), A radiative transfer model for sea surface temperature retrieval for the along-track scanning radiometer, Journal of Geophysical Research: Oceans, 100, C1, 937-952.

RD.372 Bulgin, C. E., Merchant, C. J., and Donlon, C. (2-15). Sampling Uncertainty in Global Area Coverage (GAC) and Gridded Sea Surface Temperature Retrievals. Remote Sensing of Environment

RD.385 SST_CCI User Requirements Document (URD), SST_CCI-URD-UKMO-201, Issue 2.1, 13 January 2017.

RD.387 CCI-SST Algorithm Theoretical Basis Document (ATBD) SST_CCI-ATBDv2-UOE-001, Issue 1, 17 May 2013.

RD.395 Baran, A. J., and J. S. Foot, 1994: New Application of the Operational Sounder HIRS in determining a climatology of sulfuric acid aerosol from the Pinatubo eruption. *Journal of Geophysical Research-Atmospheres*, **99,** 25673-25679. 10.1029/94jd02044

RD.396 Morak-Bozzo, S., Merchant, C. J., Kent, E. C., Berry, D. I. and Carella, G. (2016) Climatological diurnal variability in sea surface temperature characterized from drifting buoy data. Geoscience Data Journal, 3 (1). pp. 20-28. ISSN 2049-6060 doi: 10.1002/gdj3.35

RD.397 AATSR 12 um Anomaly Review Board (2013) IDEAS-VEG-OQC-REP-1274, https://earth.esa.int/web/guest/document-library/browse-document-library/-/asset_publisher/lDo6/content/aatsr-12-micron-anomaly-review-board-final-report

RD.400 SST CCI User Requirements Document (2017) SST_CCI-URD-UKMO-201, http://www.esa-sst-cci.org/PUG/documents

RD.407 Improvements to feature resolution in the OSTIA sea surface temperature analysis using the NEMOVAR assimilation scheme E. K. Fiedler, C. Mao, S. A. Good, J. Waters and M. J. Martin, in preparation for QJRMS.

RD.410 Bulgin, C. E., Mittaz, J. P. D., Embury, O., Eastwood, S., Merchant, C. J. (2018). Bayesian Cloud Detection for 37 Years of Advanced Very High Resolution Radiometer (AVHRR) Global Area Coverage (GAC) Data, Remote Sensing, 10(1), 97

1.3 Definitions of Terms

The following terms have been used in this report with the meanings shown.

Term	Definition
(A)ATSR	(Advanced) Along track scanning radiometer
AOD	Aerosol optical depth
ARB	Anomaly Review Board
ARC	ATSR Reprocessing for Climate
AVHRR	Advanced Very High Resolution Radiometer
ARGO	Global array of observational profiling floats
BT	Brightness Temperature
CCI	Climate Change Initiative
CLAVR-x	Clouds from AVHRR Extended
DJF	December, January, February
ECMWF	European Centre for Medium-range Weather Forecasting
EN3	Quality controlled subsurface temperature and salinity data set [RD.282]
ERA-40	ECMWF Re-analysis covering 40 years
FFM	Fast Forward Model
GAC	Global Area Coverage
GADS	Global Aerosol Data Set
GCOS	Global Climate Observing System
HadISST1	UKMO Hadley Centre Sea Ice and Sea Surface Temperature data set (version 1)
JJA	June, July, August
LSD	Local Standard Deviation
LUTS	Look-Up Tables
MAP	Maximum a posteriori
MD	Match-up dataset
ML	Maximum Likelihood
NRT	Near Real Time

NSIDC	National Snow and Ice Data Center
NOAA	National Oceanic and Atmospheric Administration
NWP	Numerical Weather Prediction
O-B	Observation minus Background
OE	Optimal Interpolation
OPAC	the Optical Properties of Aerosols and Clouds dataset
OSI-SAF	Ocean and Sea Ice Satellite Application Facility (EUMETSAT)
OSTIA	Operational Sea Surface Temperature and Sea Ice Analysis
PDF	Probability distribution function
QC	Quality Control
RMSE	Root Mean Square Error
RTM	Radiative Transfer Model
RTTOV	Radiative Transfer for the Television and Infrared Orbiting Satellite Operational Vertical Sounder
SADIST	Synthesis of ATSR Data Into Sea-surface Temperature.
SMMR	Scanning multichannel microwave radiometer
S-O	Simulation minus Observation
SOAR	Second Order Auto-Regressive
SOZ	Solar Zenith Angle
SSM/I	Special Sensor Microwave/Imager
SST-CCI	Sea Surface Temperature Climate Change Initiative
TCWV	Total Column Water Vapour
TOA	Top Of Atmosphere
VisRTM	Visible Radiative Transfer Model

2. OVERVIEW OF PROCESSING TO DERIVE SEA SURFACE TEMPERATURE

Deriving sea surface temperature (SST) products from imagery of visible and infra-red radiometers comprises the following conceptual steps:

- Preparatory processing. This includes orbit file reading, validity checks, association of auxiliary information to the orbit file being processed (including prior fields from numerical weather prediction, where relevant), and any pre-processing adjustment to the data themselves.
- Classification to identify valid pixels for SST retrieval. Although sometimes referred to as cloud detection, this also involves identifying which image pixels are cover only sea, and exclusion of pixels affected by sea ice or excessive aerosol.
- Retrieval of SST (geophysical inversion). Generally, SST is derived as a weighted combination of observed brightness temperatures. The weights are either extracted appropriately to the context from pre-defined coefficient files, or are calculated dynamically given prior information (in the case of optimal estimation). Estimation of the retrieval uncertainty at pixel level is also part of this step. The prime retrieval is of the radiometric temperature of the ocean, which is taken as equivalent to the skin temperature.
- Estimation of standardized SSTs. This is less common outside of SST CCI. An estimate is made, by geophysical modelling of near surface conditions, of SST at standard depth and time, given the retrieval skin SST at its observation time. An uncertainty in this adjustment is also estimated.
- Gridding / averaging. This is relevant where L3 products are derived from full resolution imagery. Uncertainty estimates from full resolution need to be propagated properly to the L3 resolution, and additionally an estimate of the sampling uncertainty (arising from incomplete observation of cells) needs to be added.
- Spatially complete interpolation (production of an L4 product). Combination of data from multiple sensors to derive a best estimate, including gap-filling by interpolation.

2.1 Algorithm differences relative to v1.1

Updated radiative transfer simulations, particularly capability to simulate atmospheric aerosol in the fast forward model RTTOV v11.3, used to include marine and stratospheric volcanic aerosol in cloud detection and optimal estimation steps.

Bayesian Cloud Detection has replaced CLAVR-x cloud detection for AVHRRs, including use of pixel-level noise estimates to help account for “noisy” periods and sensors.

Prior information on stratospheric volcanic aerosol loadings have been extended to the El Chichon period in addition to the Mt Pinatubo period, using HIRS data.

The quality level assignment algorithm has been updated, and use of quality level in atmospheric correction smoothing and regridding steps refined.

Extension to 1980s AVHRRs including per-pixel noise estimates and improved detection and adjustment of solar contamination relative to operational methods, with additional AVHRR SST-level harmonisation.

Improved uncertainty propagation and configuration of L4 processing.

3. ALGORITHMS USED IN PREPARATORY PROCESSING

Preparatory processing algorithms are the steps applied to imagery before geophysical algorithms are applied, to handle data issues.

In this reprocessing, the only preparatory algorithm is shifting of the forward view of ATSR sensors to be better collocated with nadir view.

This reprocessing is using the ESA v3 Level 2 archive for the ATSRs, for which it was hoped that no forward shifting would be necessary. However, small shifts appear to be required still, and this section presents the shifts are that are applied.

3.1 Method to estimate offsets

ATSR forward view offsets are estimated from the ATSR ultra-clear match-up dataset (MD), since parallax effects mean that only surface patterns should be used to match forward and nadir views.

From the MD file we select targets which are:

1. Fully clear according to the Bayesian Dual-Max mask
2. Have a local standard deviation of nadir-view BT11 > 0.05 for the central 3x3 pixels

For all selected targets we calculate the standard deviation of the nadir-forward BT11 difference using the central 3x3 pixels in the nadir view and all 25 3x3 boxes from the forward view:

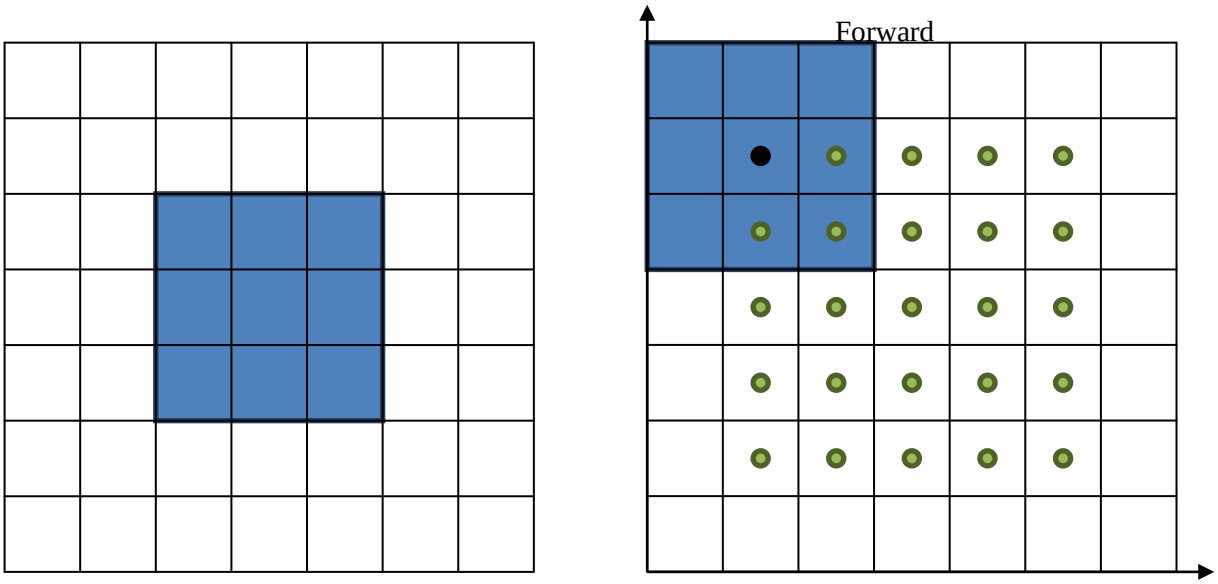

The forward view offset is estimated as the forward view box with the lowest total standard deviation summed over all matches in a year. Offsets are given as across track (element / x), along track (line, y) such that:

- (-2,-2) means the centre-nadir matches with the forward view offset by 2 pixels towards lower indices in both directions i.e. elements 0-2 and lines 0-2
- (0,0) means the centre-nadir matches with the centre of the forward view (no offset) i.e. elements 2-4 and lines 2-4

- (2,2) means the centre-nadir matches with the forward view offset by 2 pixels towards higher indices in both directions i.e. elements 4-6 and lines 4-6

3.2 Results

The offsets in the tables in the following sections are applied as a pre-processing step. The results are calculated for each year of each sensor mission. Some variation in the best offsets are found, the biggest trend found in the best fit offset across track in the case of ATSR-2. Nonetheless, all the offsets are of -1, 0, or 1 pixel, which represents a distinct improvement from the situation in the previous reprocessing on L1b v2.0.

3.2.1 ATSR1

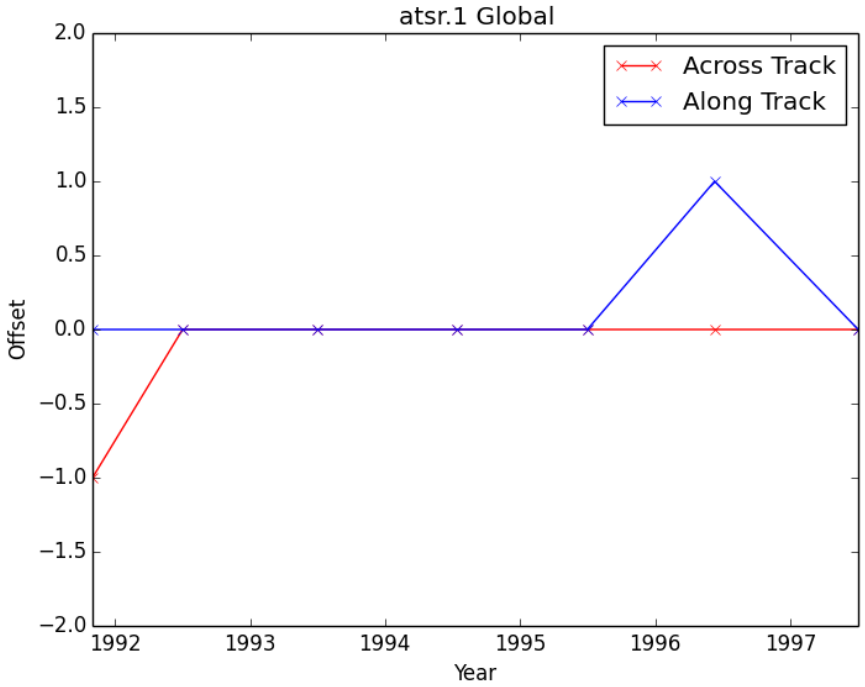

Year	Across track	Along track
1991	-1	0
1992	0	0
1993	0	0
1994	0	0
1995	0	0
1996	0	1
1997	0	0

3.2.2 ATSR2

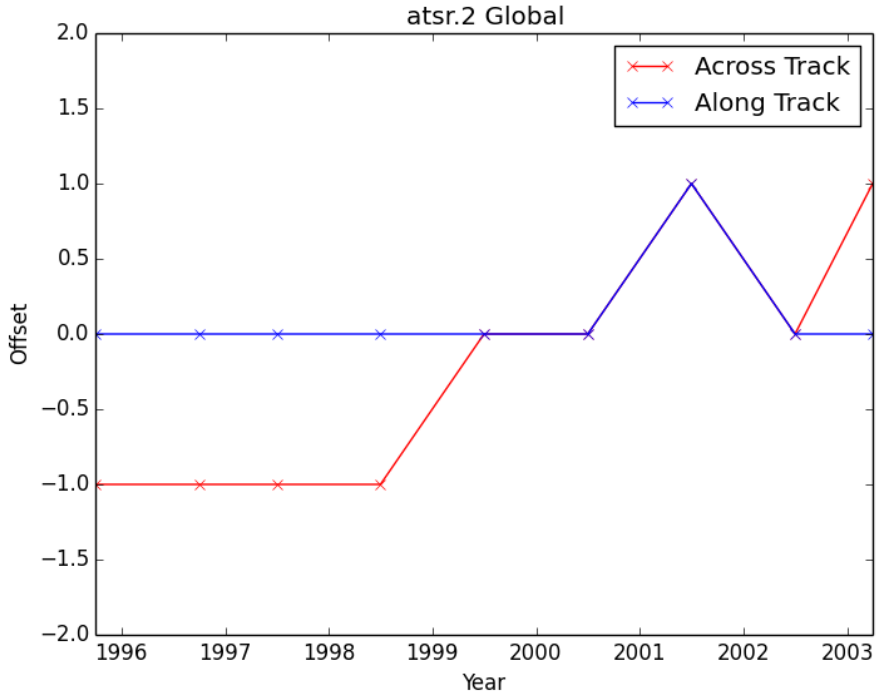

Year	Across track	Along track
1995	-1	0
1996	-1	0
1997	-1	0
1998	-1	0
1999	0	0
2000	0	0
2001	1	1
2002	0	0
2003	1	0

3.2.3 AATSR

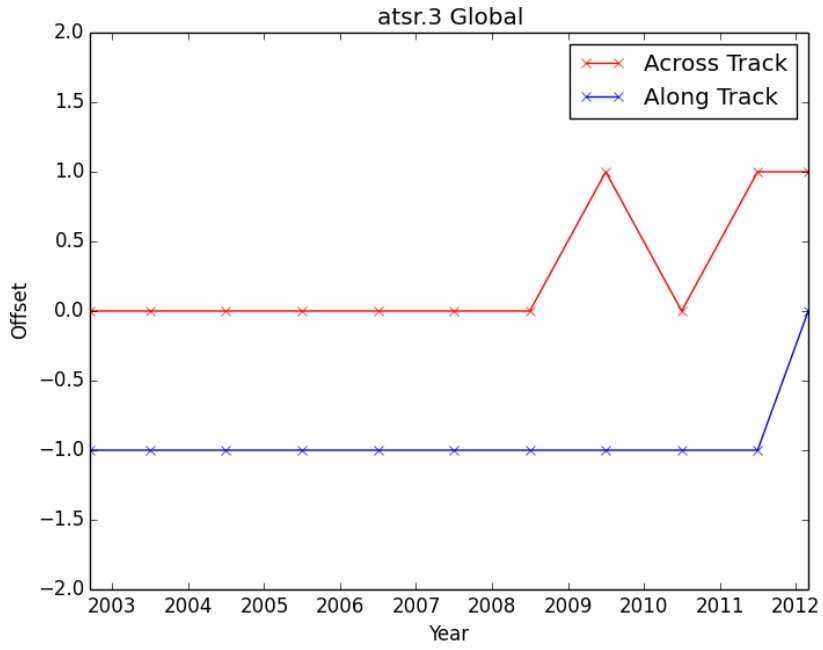

Year	Across track	Along track
2002	0	-1
2003	0	-1
2004	0	-1
2005	0	-1
2006	0	-1
2007	0	-1
2008	0	-1
2009	1	-1
2010	0	-1
2011	1	-1
2012	1	0

4. IDENTIFICATION OF OBSERVATIONS VALID FOR SEA SURFACE TEMPERATURE ESTIMATION

Cloud screening is a fundamental pre-processing step for sea surface temperature (SST) retrieval. Traditionally, threshold based techniques have been used to detect cloud but these often fail under difficult circumstances -- for example, in the detection of thin cirrus or low-level fog.

The Bayesian cloud detection algorithms presented here was developed original for ATSR instruments, and is now with v2 extended also to AVHRR instruments. The posteriori probability of clear sky is calculated, and retrievals are performed for pixels where this exceeds 90%.

4.1 General Overview of Bayesian Classifier

4.1.1 Applicability of Bayes' Theorem

The Bayesian classifier calculates a probability of clear-sky for any given pixel based on the satellite observations, prior information about the atmosphere and surface conditions and the respective errors in these variables. This is done based on Bayes' theorem.

In discussing Bayes' theorem, notation for conditional probability is used. Thus $P(A|B,C)$ is the probability density for condition or observation A given the assumption that conditions/observations B and C are the case. In this notation, cloud detection is the calculation of $P(c|\boldsymbol{y}^o,\boldsymbol{x}^b)$ -- i.e., the probability of the clear-sky condition, given the observations $\boldsymbol{y}^o$ and the prior information we have brought to the problem, $\boldsymbol{x}^b$. The Bayesian classifier calculates the likelihood that a pixel is a clear-sky ($P(c|\boldsymbol{y}^o,\boldsymbol{x}^b)$) based on the satellite observations and prior information. Formally Bayes theorem applied to the problem of cloud detection can be written:

$$P(c|\boldsymbol{y}^o,\boldsymbol{x}^b)=\frac{P(\boldsymbol{y}^o|\boldsymbol{x}^b,c)P(\boldsymbol{x}^b|c)P(c)}{P(\boldsymbol{y}^o|\boldsymbol{x}^b)P(\boldsymbol{x}^b)} \quad \textbf{(4-1)}$$

where:

c	denotes clear-sky
$\boldsymbol{y}^o$	is the observation vector
$\boldsymbol{x}^b$	is the state vector.

The assumption can be made that the background state is independent of the clear-sky probability at the satellite pixel scale (1x1 km). Assuming $P(\boldsymbol{x}^b|c)=P(\boldsymbol{x}^b)$, then equation 4-1 can be simplified to give:

$$P(c|\boldsymbol{y}^o,\boldsymbol{x}^b)=\frac{P(\boldsymbol{y}^o|\boldsymbol{x}^b,c)P(c)}{P(\boldsymbol{y}^o|\boldsymbol{x}^b)} \quad \textbf{(4-2)}$$

The probability of the observations given the background state, $P(\boldsymbol{y}^o|\boldsymbol{x}^b)$, can be expressed as the sum of the probabilities for each possible state (cloud $\bar{c}$ and clear c).

$$P(\boldsymbol{y}^o|\boldsymbol{x}^b)=P(c)P(\boldsymbol{y}^o|\boldsymbol{x}^b,c)+P(\bar{c})P(\boldsymbol{y}^o|\boldsymbol{x}^b,\bar{c}) \quad \textbf{(4-3)}$$

This can be rearranged to give the form of the equation used in the clear-sky probability calculation.

$$P(c|\boldsymbol{y}^o, \boldsymbol{x}^b) = \left[1 + \frac{P(\bar{c})P(\boldsymbol{y}^o|\boldsymbol{x}^b, \bar{c})}{P(c)P(\boldsymbol{y}^o|\boldsymbol{x}^b, c)}\right]^{-1} \quad \textbf{(4-4)}$$

$P(\bar{c})$ is the prior probability of cloud and is equal to one minus the prior probability of clear-sky.

$$P(\bar{c}) = 1 - P(c) \quad \textbf{(4-5)}$$

4.1.2 Overview of flow of Bayesian processing

Figure 4-1 shows a high level overview of the classification process. The Bayesian classifier for the SST CCI processing takes European Centre for Medium-range Weather Forecasting (ECMWF) numerical weather prediction (NWP) reanalysis data as input to simulate clear sky brightness temperatures and top of the atmosphere reflectance. The other inputs are ATSR satellite observations and cloudy PDF LUTs. The Bayesian classifier provides the probability of clear-sky as output on a per pixel basis for use in conjunction with the SST data.

Figure 4.2 gives a more detailed overview of the steps involved in the Bayesian classification. The inputs, auxiliary data, calculations and outputs are described in the following sections, firstly for ATSR sensors, and then for AVHRR sensors.

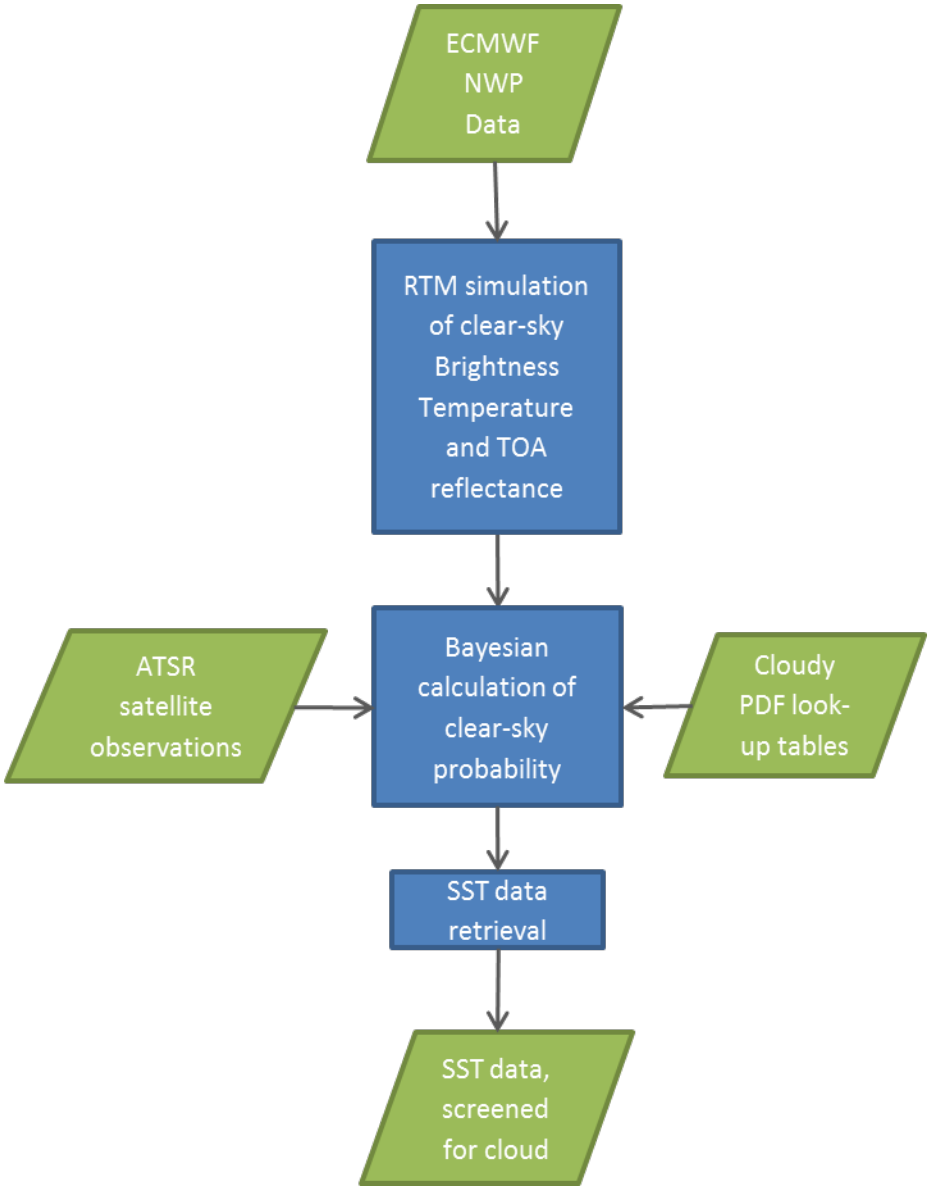

Figure 4-1. Flow chart showing overview of the classification process. Green parallelograms indicate input data, blue squares indicate processing steps.

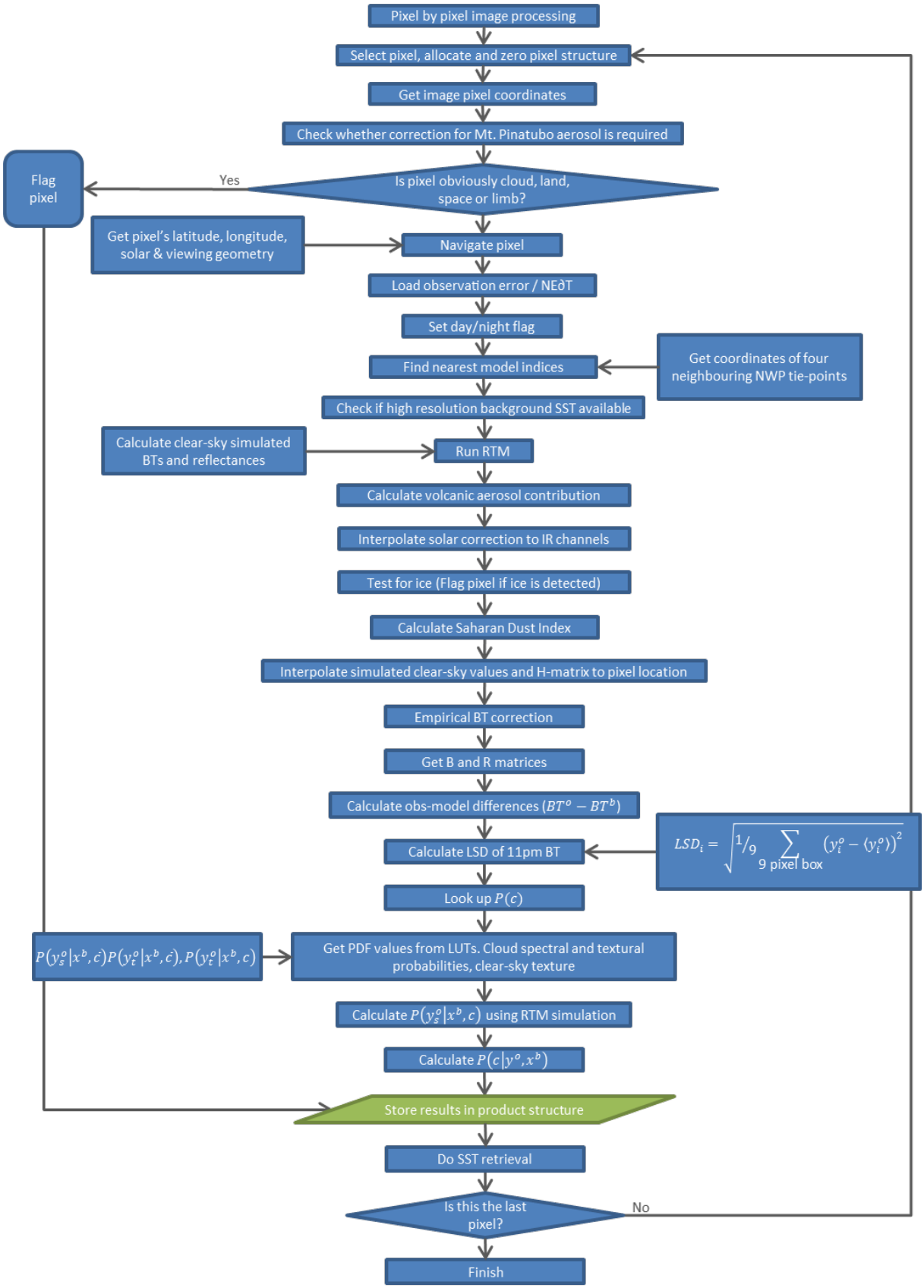

Figure 4-2. Bayesian classification steps for calculating clear-sky probability prior to SST retrieval. Blue rectangles denote processing steps, blue diamonds decision making steps and green parallelograms data storage.

4.1.3 Equations for elements of probability calculation

The probability of the observations given the background state for either class (cloud or clear) is split into a spectral and textural component denoted by subscripts 's' and 't'. These are assumed to be independent.

$$P(\boldsymbol{y}^o|\boldsymbol{x}^b, c) = P(\boldsymbol{y}_s^o|\boldsymbol{x}^b, c)P(\boldsymbol{y}_t^o|\boldsymbol{x}^b, c) \quad \textbf{(4-6)}$$

For the cloud class the spectral component of this equation is calculated from a probability density function (PDF) look up table as described in section 4.2.1.2. For clear-sky this is calculated using the radiative transfer model where the distribution is assumed to be Gaussian. The spectral probability for clear-sky is defined as follows:

$$P(\boldsymbol{y}_s^o|\boldsymbol{x}^b, c) = \frac{e^{\left(-\frac{1}{2}\Delta y^t(\boldsymbol{H}^t\boldsymbol{B}\boldsymbol{H}+\boldsymbol{R})^{-1}\Delta y\right)}}{2\pi|\boldsymbol{H}^t\boldsymbol{B}\boldsymbol{H}+\boldsymbol{R}|^{0.5}} \quad \textbf{(4-7)}$$

$\boldsymbol{H}^t\boldsymbol{B}\boldsymbol{H}$ is the error covariance in the background state vector propagated through the fast forward model. The $\boldsymbol{H}$ matrix contains the tangent linear of the forward model.

$$\boldsymbol{H} = \frac{\partial \boldsymbol{y}_s^b}{\partial \boldsymbol{x}^b} \quad \textbf{(4-8)}$$

This expresses the sensitivity of the forward model radiance (brightness temperature or reflectance) to changes in the reduced state vector ($\boldsymbol{x}^b$).

The matrices for the Bayesian calculation depend on the uncertainty in NWP, forward modelling and the results of forward modelling. The H matrix is defined as follows for the case of three thermal channels. Equivalents for other channel selections follow the same construction in an obvious way.

$$\boldsymbol{H} = \begin{bmatrix} \frac{\partial BT_{3.7}}{\partial SST^b} & \frac{\partial BT_{10.8}}{\partial SST^b} & \frac{\partial BT_{12.0}}{\partial SST^b} \\ \frac{\partial BT_{3.7}}{\partial TCWV^b} & \frac{\partial BT_{10.8}}{\partial TCWV^b} & \frac{\partial BT_{12.0}}{\partial TCWV^b} \\ \frac{\partial BT_{3.7}}{\partial \boldsymbol{u}_{10}^b} & \frac{\partial BT_{10.8}}{\partial \boldsymbol{u}_{10}^b} & \frac{\partial BT_{12.0}}{\partial \boldsymbol{u}_{10}^b} \\ \frac{\partial BT_{3.7}}{\partial AOD^b} & \frac{\partial BT_{10.8}}{\partial AOD^b} & \frac{\partial BT_{12.0}}{\partial AOD^b} \end{bmatrix} \quad \textbf{(4-9)}$$

Under nighttime conditions the tangent linears with respect to wind speed and aerosol optical depth are set to zero. $\boldsymbol{B}$ is the background error covariance matrix and contains the errors of the components in the reduced state vector. This can be specified as follows:

$$\boldsymbol{B} = \begin{bmatrix} (\varepsilon_{SST}^{b})^2 & 0.0 & 0.0 & 0.0 \\ 0.0 & (\varepsilon_{TCWV}^{b})^2 & 0.0 & 0.0 \\ 0.0 & 0.0 & \left(\varepsilon_{\boldsymbol{u}_{10}}^{b}\right)^2 & 0.0 \\ 0.0 & 0.0 & 0.0 & (\varepsilon_{AOD}^{b})^2 \end{bmatrix} \quad \textbf{(4-10)}$$

Matrix $\boldsymbol{R}$ is the error covariance matrix of the differences between the model and observed values. The model component, $\boldsymbol{R}^m$, can be derived as:

$$\boldsymbol{R}^m = \begin{bmatrix} (\varepsilon_i^m)^2 & r^2(\varepsilon_i^m)(\varepsilon_j^m) \\ r^2(\varepsilon_i^m)(\varepsilon_j^m) & \left(\varepsilon_j^m\right)^2 \end{bmatrix} \quad \textbf{(4-11)}$$

where the diagonal terms describe the FFM error in the given channel and the off-diagonal terms the co-variance in that error. The observational component of this error is defined as the 'noise' in the observations or noise-equivalent delta brightness temperature (NEdT) in the thermal channels. This is assumed to be diagonal:

$$\boldsymbol{R}^o = \begin{bmatrix} (\varepsilon_i^o)^2 & 0.0 \\ 0.0 & \left(\varepsilon_j^o\right)^2 \end{bmatrix} \quad \textbf{(4-12)}$$

$\boldsymbol{R}^o$ and $\boldsymbol{R}^m$ are combined to define the **R** matrix. We assume that r^2 is equal to zero for the model error and therefore the off-diagonal terms of this matrix remain as zero.

$$\boldsymbol{R} = \boldsymbol{R}^m + \boldsymbol{R}^o = \begin{bmatrix} (\varepsilon_i^m)^2 + (\varepsilon_i^o)^2 & r^2(\varepsilon_i^m)(\varepsilon_j^m) \\ r^2(\varepsilon_i^m)(\varepsilon_j^m) & \left(\varepsilon_j^o\right)^2 + \left(\varepsilon_j^m\right)^2 \end{bmatrix} \quad \textbf{(4-13)}$$

For both clear and cloud classes the textural component is the local standard deviation of the 10.8 μm channel in the nine surrounding pixels (equation 2.3). All textural probabilities are stored in PDF LUTs.

4.1.4 Additional steps to account for volcanic stratospheric aerosol

The eruptions of Mount Pinatubo (and Mount Hudson) in 1991 and of El Chichon injected significant amounts of sulfur dioxide gas into the stratosphere. This gas hydrolysed to an aerosol of sulfuric acid droplets that then decayed over a period of several years while spreading latitudinally. The aerosol has an impact at infrared wavelengths and a correction is made to the simulated brightness temperatures to account for this [RD.186] during cloud detection.

Stratospheric aerosol is included in the forward model (RTTOV11.3) by adding a uniform later of sulphate aerosol between 20 and 24 km altitude. The aerosol number density for the layer is proportional to the infrared aerosol index (section 4.2.1.4).

(4-14)

$$n_0 = 32800 \times \text{aerosol\_index}$$

This aerosol index, and therefore the adjustment, goes to zero outside of the volcanic aerosol periods, and therefore the adjustment is also then zero.

4.1.5 Auxiliary data for cloud detection used for all sensors

4.1.5.1 Prior probability of clear sky

The NWP total cloud cover, $\boldsymbol{t}$, informs is the basis for the prior probability of clear, which is:

$$\boldsymbol{P(c) = 1 - \begin{cases} \mathbf{0.5}, \boldsymbol{t} < 0.5 \\ \boldsymbol{t}, \mathbf{0.5} \leq \boldsymbol{t} < 0.95 \\ \mathbf{0.95}, \boldsymbol{t} > 0.95 \end{cases}}$$

The truncation of the range is designed to compensate for expected uncertainties in the NWP data, such as frontal regions being misplaced, and cloud gaps not being resolved.

4.1.5.2 Stratospheric Volcanic Aerosol Index

The aerosol index represents the effective sulphate aerosol number density in the stratospheric layer for the two main eruption periods (post-Mount Pinatubo and post-El Chichón). The auxiliary data daily zonal (1 degree resolution) fields. These have been derived from HIRS observations shown in, using an update of the method of RD.395. The method exploits the differential sensitivity to aerosol of the 8.7 um channel of HIRS. To create continuous data from the HIRS orbit data, the complete field was estimated using a Kalman smoother applied daily to the day's retrievals plus the value of the field on adjacent days advected using ERA-interim stratospheric winds between 20 and 25 km.

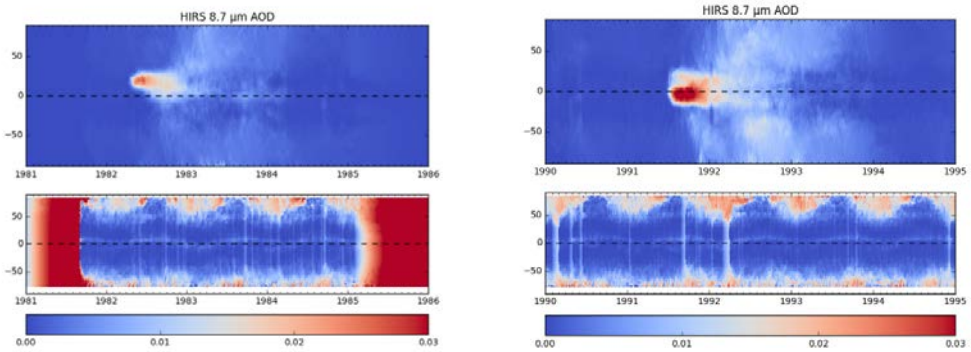

Figure 4-3. Stratospheric AOD calculated from HIRS. Left: El Chichón; Right: Mount Pinatubo; Top: IR AOD; Bottom: IR AOD uncertainty

Given this aerosol index information, stratospheric aerosol is included in the forward model simulations (RTTOV) and it applies to both Bayesian Cloud detection and Optimal Estimation SST retrievals.

4.1.6 Result of Bayesian Cloud Detection

The cloud detection algorithm outputs a probability of clear-sky for each pixel processed. SST retrieval is also done for each pixel so that the user on an application specific basis can determine the stringency of the cloud screening. Within the CCI project the SST retrieval is applied to pixels with a clear-sky probability greater than 0.1; however pixels with clear-sky probability less than 0.9 are considered low quality and not recommended for quantitative purposes.

4.1.7 Assumptions and Limitations

This section describes the current performance of the Bayesian cloud detection, considers assumptions and limitations and future enhancements to the algorithm

4.1.7.1 Current Performance

Over the ocean the Bayesian cloud detection performs better than the threshold based operational cloud mask. This is evidenced in the reduction of the standard deviation of the AATSR satellite minus in-situ SST differences between July 2002 and December 2007 when using the Bayesian cloud detection compared to SADIST [RD.184].

There are known regions and particular cloud types where cloud detection is more difficult. The easiest cloud to detect is that which is 'bright' and 'white' providing a distinct signal at both visible and infrared wavelengths that differs from that of the dark underlying ocean surface. Low-level fog is often dark making it difficult to distinguish at visible wavelengths and has a temperature close to the SST. Thin or semi-transparent ice cirrus often has a sub-pixel extent and is also difficult to detect.

At high latitudes cloud detection is also more difficult in regions of sea-ice. Newly formed sea-ice is close in temperature to the neighbouring open-water pixel and the surface is dark. Over the sea-ice surface, melt ponds can also make it difficult to identify whether the surface is water or ice. Sea-ice pixels mistakenly classified as open water, will bias the SST retrieval.

4.1.7.2 Assumptions Made

Within the Bayesian cloud detection independence is assumed between the infrared and visible channel probabilities of clear and cloud observations. In the context of the reduced state vector, TOA reflectance is assumed independent of prior SST. This assumption is made to simplify the forward modelling. Spectral and textural probabilities are also assumed to be independent allowing the extraction of two pieces of information from the observations.

In the $\boldsymbol{R}^m$ matrix an $\boldsymbol{r}^2$ value of zero is assumed in the off-diagonal term giving no covariance between channels. In reality there will be a strong error covariance between the 10.8 and 12 μm channels (and the 3.7 μm channel at night). Further research is needed to correctly determine the off-diagonal terms of this matrix.

In the cloud detection scheme the assumption is made that the pixel will either be 'clear over ocean' or 'cloud'. Sea-ice pixels are unlikely to be well represented in the cloudy PDFs and therefore are more likely to be misclassified.

4.1.8 Future Enhancements

Using a three-way image classifier could enhance cloud detection at high latitudes. Each pixel would be classified as 'clear-over-water', 'clear-over-ice' or cloud. The sea-ice surface could be modelled using the FFMs to help distinguish between open-water and ice pixels. Work was undertaken as part of SST CCI in parallel with the high latitude extension developed for the AVHRR instruments [RD.308]. This showed particular benefits for AATSR where visible channel information were always available during the day, but more development is required for a consistent application across all ATSR instruments so as not to introduce a bias in the retrieved SSTs.

4.2 Clear-sky Detection for Along Track Scanning Radiometers (ATSRs)

This section addresses implementation aspects for Bayesian Cloud Detection specific to ATSRs.

The Along Track Scanning Radiometer (ATSR) instruments make observations at infrared and visible wavelengths at two viewing angles: the nadir view between 0-22° and the forward view between 52-55°. Both views can be exploited to give additional information for cloud detection purposes. ATSR-1 made measurements in spectral bands centred at 1.6, 3.7, 10.8 and 12 μm, whilst ATSR-2 and AATSR instruments had additional visible wavelength channels centred at 0.55, 0.66 and 0.87 μm. The probability of clear sky is calculated by assessing the likelihood that the pixel is clear given the observations, background information, cloudy probability density function (PDF) look-up tables (LUTs) and simulations of clear-sky conditions.

4.2.1 Inputs to Bayesian Classifier

The Bayesian classifier uses a number of inputs including sensor data, numerical weather prediction data, radiative transfer model output and cloud.

4.2.1.1 Sensor Data - Brightness Temperature, Reflectance

The ATSR observations used in the Bayesian classifier form the observation vector, $\boldsymbol{y}^o$. The subset of channels used in the observation vector is dependent on time of day.

The channels used in the cloud detection algorithm are present on all ATSR sensors and give consistency over the dataset time series. The cloud detection algorithm is a dual view retrieval using data in the channels specified from both the nadir and forward views. The observation vector, $\boldsymbol{y}^o$, is defined under day conditions as,

$$\boldsymbol{y}^o = \begin{bmatrix} RE_{1.6} \\ BT_{10.8} \\ BT_{12.0} \\ LSD_{3x3}(BT_{10.8}) \end{bmatrix} \quad \textbf{(4-9)}$$

under night conditions as,

$$\boldsymbol{y}^o = \begin{bmatrix} BT_{3.7} \\ BT_{10.8} \\ BT_{12.0} \\ LSD_{3x3}(BT_{10.8}) \end{bmatrix} \quad \textbf{(4-10)}$$

and under twilight conditions as,

$$\boldsymbol{y}^o = \begin{bmatrix} BT_{10.8} \\ BT_{12.0} \\ LSD_{3x3}(BT_{10.8}) \end{bmatrix} \quad \textbf{(4-11)}$$

where:

BT	denotes brightness temperature
LSD	is the local standard deviation over a 3x3 pixel box

RE denotes reflectance

1.6, 3.7, 10.8, 12.0 subscripts define the ATSR channel.

The 10.8 and 12 μm brightness temperatures are used under all conditions and the 1.6 and 3.7 μm channels are alternated on the basis of the solar zenith angle. Daytime conditions are defined by a solar zenith angle less than 87.5 degrees, and nighttime conditions by solar zenith angles above 92.5 degrees. The twilight condition is between 87.5 and 92.5 degrees where a minimum set of channels is used. In addition to the spectral information, the local standard deviation in the 10.8 μm brightness temperature is used as a textural measure in the observational data.

$$LSD_i = \sqrt{{}^1\!/_9 \sum_{9 \text{ pixel box}} (y_i^o - \langle y_i^o \rangle)^2} \qquad \textbf{(4-12)}$$

where:

$\boldsymbol{y_i^o}$ is the 10.8 μm brightness temperature for a given observation.

$< \boldsymbol{y_i^o} >$ is the mean 10.8 μm brightness temperature across the 3x3 pixel box.

4.2.1.2 Auxiliary Data and Look-Up Tables

NWP data from the ECMWF are used in the radiative transfer forward modelling (section 4.2.1.3) to simulate clear sky brightness temperatures and top of the atmosphere (TOA) reflectance. The full background state vector contains all surface and atmospheric variables that can influence the calculated radiance. For the characterisation of the uncertainty in the clear-sky simulation results that is needed for the Bayesian calculation, only the dominant terms need be considered. These terms are shown in the reduced state vector, $\boldsymbol{x}^b$, shown below. At nighttime (when only infra-red channels are used), the uncertainty with respect to windspeed and aerosol optical depth (AOD) is set to zero. For ATSR-1 during the period of elevated stratospheric aerosol from the eruption of Mt Pinatubo, a fifth element describing the stratospheric aerosol is included in the state vector. For the rest of the record, the reduced state vector is:

$$\boldsymbol{x}^b = \begin{bmatrix} SST^b \\ TCWV^b \\ \boldsymbol{u}_{10}^b \\ AOD^b \end{bmatrix} \qquad \textbf{(4-13)}$$

where:

SST is sea surface temperature

TCWV is total column water vapour

$\boldsymbol{u}_{10}$ is the 10 m wind vector

AOD is aerosol optical depth.

Reflectance/BT distributions given cloud probabilities are stored as empirical PDFs as these are difficult to model and cannot be assumed to be Gaussian. The PDFs are generated using the entire ATSR time series of observations initially bootstrapped using the operational SADIST cloud mask to identify cloudy pixels. Subsequently these were iterated once using the Bayesian cloud detection scheme as part of the ATSR Reprocessing for Climate (ARC) project. This iteration enabled the inclusion of dual view data and refinement of the PDF dimensions.

The probability density function (PDF) given the background state for each class of observation (clear or cloud) is expressed as a 'spectral' and 'textural' component (outlined in section 4.1.3), which are assumed to be independent. For both cloud and clear classes, the textural component is an empirical PDF (captured as a look up table, LUT) generated as explained above. This is also the case for the spectral component for the cloud class. The clear-sky spectral PDF is calculated using the forward models based on the uncertainty of the elements in $\boldsymbol{x}^b$. The dimensions, range and binsize of the respective PDFs (LUTs) are shown in the tables below. These are chosen so that the resulting PDF is adequately smooth, for which we required that the numbers of observations used to build the LUTs was at least three orders of magnitude larger than the number of LUT bins. The satellite zenith angle dimension is used to separate the nadir and forward view PDFs. Observations that fall outside the PDF dimensions are fixed to the edge of the PDFs for the Bayesian cloud detection.

For the spectral probability under nighttime conditions a three channel brightness temperature PDF is used. This includes a day/night flag as it is also used in conjunction with a visible channel PDF during the day.

Table 4-1. Cloud Nighttime Spectral PDF

Dimension	Unit	Upper limit	Lower limit	Bin size	Number of bins
11µm BT – NWP SST	K	10.00	-20.00	2.0	15
11-12µm BT difference	K	9.0	-1.00	0.2	50
3.7-11µm BT	K	10.00	-6.00	0.2	80
NWP SST	K	310.00	260.00	2.5	20
Satellite zenith angle	°	60.00	0.0	30.0	2
Day/Night	°	180.00	0.0	90.0	2

Figure 4- shows some slices of the spectral PDF described in Table 4-1. The PDFs are three-dimensional in brightness temperature space (11 μm BT–NWP SST, 11–12 μm BT and 3.7–11 μm BT). For visualization purposes the PDFs have been collapsed along one of these dimensions and presented for nadir only data for two different NWP SST values. The 11–12 μm BT is plotted as a function of 11 μm BT–NWP SST in the top panel, and as a function of the 11-3.7 μm BT in the bottom panel. The PDF shape and orientation shifts significantly between the two NWP SSTs in the slices presented indicating the importance of constraining the PDF as a function of all the constituent dimensions.

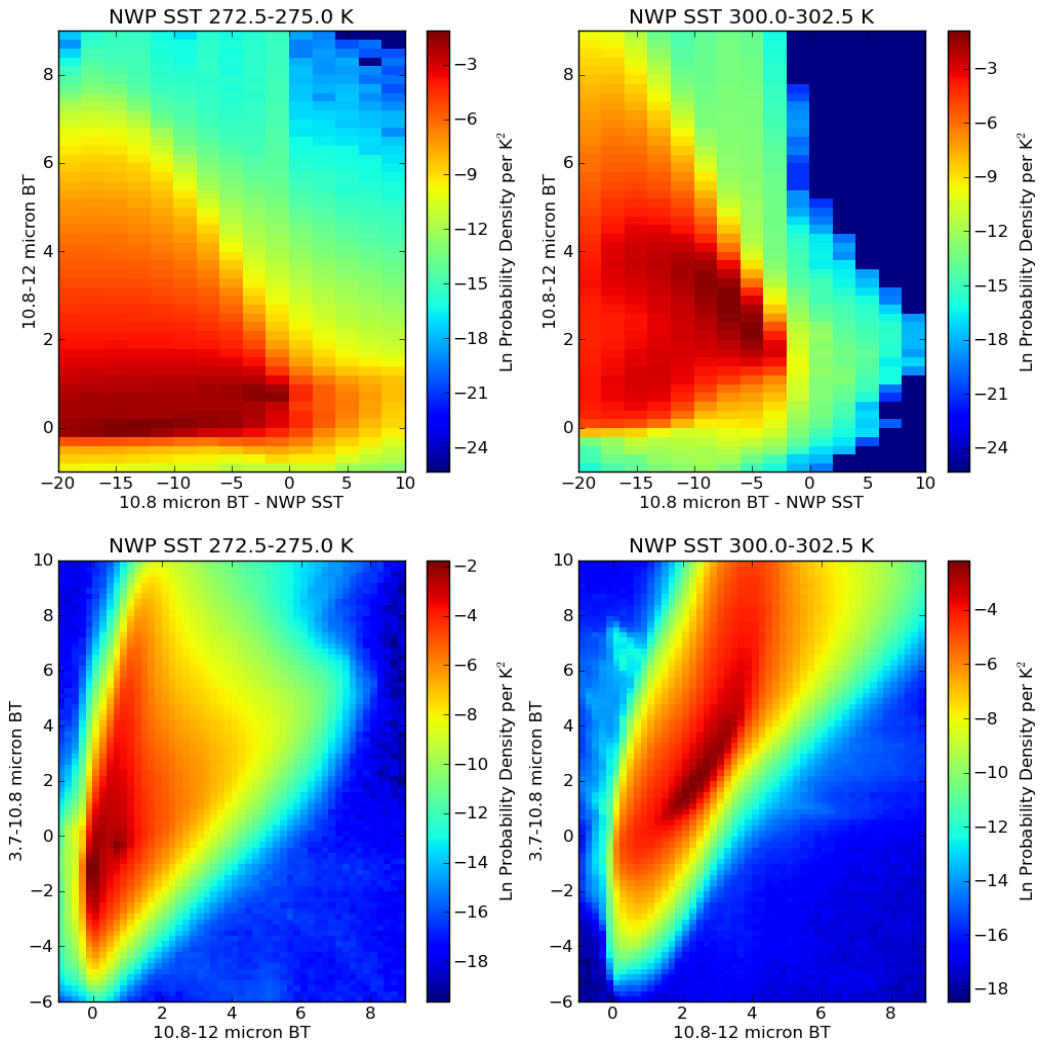

Figure 4-5. Example thermal spectral PDFs for two NWP SST values. The top panel shows the 10.8 micron BT minus the NWP SST against the 10.8 minus 12 micron BT. The lower panel shows the 3.7 minus 10.8 micron BT against the 10.8 minus 12 micron BT. PDF shapes show significant variation as a function of SST.

During the day, the observation vector includes both infrared and visible channel data. The PDFs for the infrared and visible components are assumed to be independent which is justified by the different physical processes determining radiance in the reflectance compared to thermal bands. A reduced thermal spectral PDF based on the 10.8 and 12 μm channels only is used in conjunction with a visible PDF based on the 1.6 μm channel.

Table 4-2. Daytime two-channel thermal cloudy spectral PDF

Dimension	Unit	Upper limit	Lower limit	Bin size	Number of bins
11μm BT – NWP SST	K	10.00	-20.00	1.0	30
11-12μm BT difference	K	9.0	-1.00	0.2	50
NWP SST	K	310.00	260.00	1.0	20
Satellite zenith angle	°	60.00	0.0	30.0	2
Day/Night	°	180.00	0.0	90.0	2

Table 4-3. Daytime reflectance cloudy spectral PDF

Dimension	Unit	Upper limit	Lower limit	Bin size	Number of bins
1.6µm reflectance		1.00	0.0	0.01	100
Solar zenith angle	°	95.00	0.0	2.5	38
Satellite zenith angle	°	60.00	0.0	30.0	2

Figure 4-4 shows a graphical representation of the dual view PDF for the 1.6 µm channel. The two panels show the dual view data for different solar zenith angles. As the solar zenith angle increases the PDF becomes more spread out with a tendency towards higher reflectance in the nadir view. At lower solar zenith angles the 1.6 µm nadir versus forward view PDF is closer to the 1:1 line. The reflectance peak for relatively dark clouds may be the result of partially filled pixels flagged as cloud where some of the darker underlying ocean surface is also visible.

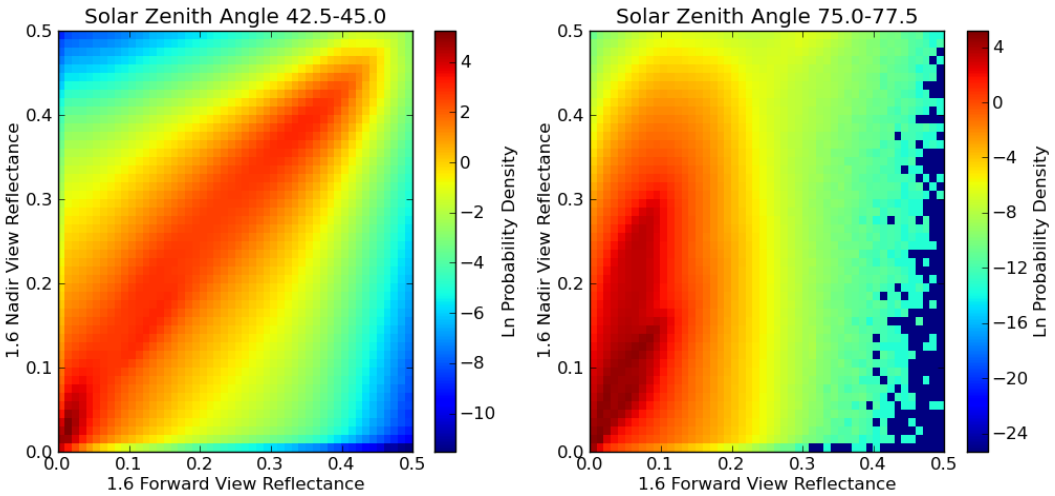

Figure . Visible spectral dual view PDFs showing the 1.6 micron nadir versus forward view reflectance given cloudy conditions.

A 10.8 µm textural PDF is a useful tool for cloud detection and is used alongside the spectral PDF for all classifications [Table 4-4]. Figure 4-5 shows the textural PDF under day and nighttime conditions for the nadir view data. The cloudy PDF is much broader than the clear-sky PDF as cloud surfaces are more heterogeneous than the underlying sea surface over a 3x3 pixel [3x3 km] surface area.

Table 4-4. Textural PDF construction. Separate PDFs are generated for clear-sky and cloudy conditions.

Dimension	Unit	Upper limit	Lower limit	Bin size	Number of bins
11 µm texture	K	2.0	0.0	0.005	400
Satellite zenith	°	60.0	0.0	30.0	2
Day/Night	°	180.0	0.0	90.0	2

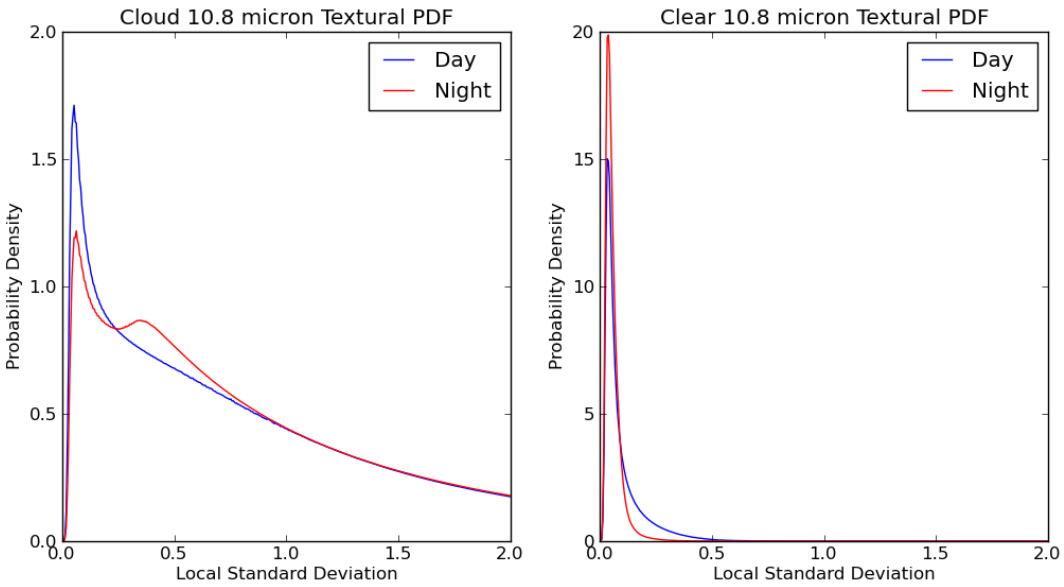

Figure 4-4. 11 micron textural PDFs dependent upon time of day for cloud and clear-sky observations (nadir view only)

4.2.1.3 Forward model

A single forward model is used for the cloud detection scheme. RTTOV 11.2 supports both channels at infrared wavelengths (3.7, 11, and 12 um) and solar channels (1.6 um). Solar corrections are included for the 3.7 um channel, although the current version of the processor does not yet use the processor during the day. Tangent linears are calculated with respect to elements of the reduced state vector (xb) for the calculated brightness temperature or reflectance.

RTTOV 11.2 is the most recent edition of a fast forward model (FFM) developed at the EUMETSAT NWP Satellite Application Facility to calculate atmospheric radiative transfer at infrared and visible wavelengths [RD.309]. NWP atmospheric profile and surface conditions are used as input and the model is run at the ATSR geolocation tie-points at a resolution of 25 x 32 km. The outputs are then interpolated to the pixel location.

4.3 Clear-sky Detection for Advanced Very High Resolution Radiometers (AVHRRs)

This section addresses implementation aspects for Bayesian Cloud Detection specific to AVHRRs, published in RD.410.

The Advanced Very High Resolution Radiometer (AVHRR) instruments make observations at visible and infrared wavelengths. AVHRR instruments have a single view, with satellite zenith angles ranging between 0-55.4°. Data are processed at two resolutions: Full Resolution Area Coverage (FRAC) and Global Area Coverage (GAC). Clear-sky detection is based on the Bayesian classifier described in Section 4.1.

4.3.1 Inputs to Bayesian Classifier

The Bayesian classifier uses a number of inputs including sensor data, numerical weather prediction data, radiative transfer model simulations and auxiliary PDFs for cloud detection.

4.3.1.1 Sensor Data – Brightness Temperature and Reflectance

Three different AVHRR instruments (1-3) have been operational during the AVHRR data record between 1979-2016, with different numbers of channels available. The wavelength bands and channel numbers for the AVHRR instruments are provided below in Table 4-5 to Table 4-7 [RD.312].

Table 4-5 AVHRR-1 Channel Wave Bands

Channel number	Wave Band (μm)
1	*0.58 – 0.68*
2	*0.725 – 1.0*
3	*3.55 – 3.93*
4	*10.3 – 11.3*

Table 4-6 AVHRR-2 Channel Wave Bands

Channel number	Wave Band (μm)
1	*0.58 – 0.68*
2	*0.725 – 1.0*
3	*3.55 – 3.93*
4	*10.3 – 11.3*
5	*11.5 – 12.5*

Table 4-7 AVHRR-3 Channel Wave Bands

Channel number	Wave Band (μm)
1	*0.58 – 0.68*
2	*0.725 – 1.0*
3A	*1.58 – 1.64*
3B	*3.55 – 3.93*
4	*10.3 – 11.3*
5	*11.5 – 12.5*

The instrument type of each member of the AVHRR series is given in Table 4-8. For AVHRR-3 instruments, data are only transmitted from either channel 3A or 3B at any given time, with the intention to relay channel 3A data during the daytime and channel 3B data at night. For some AVHRR-3 instruments channel 3A information is not consistently transmitted during the day and channel 3B data are provided for the entire instrument record. Subsets of the available channels are used in the cloud detection algorithm depending on the instrument and time of day.

Table 4-8 AVHRR instrument types

Instrument	Instrument Number
AVHRR-1	6,8,10
AVHRR-2	7,9,11,12,14
AVHRR-3	15,16,17,18,19, Metop-A, Metop-B

FRAC data have a nominal spatial resolution of 1.1 km at nadir. GAC data are an average of the data from four pixels across track, used to represent a footprint of five pixels across track by three pixels along track. GAC data are sampled by averaging four pixels along track, missing one pixel and then averaging four more pixels, for every third scan line. They have a nominal resolution of 4 km at nadir.

The AVHRR observations used in the Bayesian classifier form the observation vector, $\boldsymbol{y}^o$. For AVHRR-1 instruments the observation vector is defined under day conditions as:

$$y_o = \begin{bmatrix} RE_{0.6} \\ RE_{0.8} \\ BT_{10.8} \\ LSD_{3x3}(BT_{10.8}) \end{bmatrix}$$

and under night conditions as:

$$y_o = \begin{bmatrix} BT_{3.7} \\ BT_{10.8} \\ LSD_{3x3}(BT_{10.8}) \end{bmatrix}$$

where:

BT	denotes brightness temperature
LSD	is the local standard deviation over a 3x3 pixel box
RE	denotes reflectance

0.6, 0.8, 3.7, 10.8, 12.0 subscripts define the AVHRR channel.

For AVHRR 2 and 3 instruments the observation vector is defined under daytime conditions as:

$$y_o = \begin{bmatrix} RE_{0.6} \\ RE_{0.8} \\ BT_{10.8} \\ BT_{12.0} \\ LSD_{3x3}(BT_{10.8}) \end{bmatrix}$$

and under nighttime conditions as:

$$y_o = \begin{bmatrix} BT_{3.7} \\ BT_{10.8} \\ BT_{12.0} \\ LSD_{3x3}(BT_{10.8}) \end{bmatrix}$$

4.3.2 Auxiliary Data and Look-Up Tables

The background state vector for AVHRR clear-sky detection is the same as that specified for the ATSR instruments, and is described in section 4.2.1.2.

Probability density functions (PDFs) of reflectance and brightness temperature distributions under cloud conditions are generated empirically as these are difficult to model and cannot be assumed to be Gaussian. Separate PDFs are generated for AVHRR FRAC and AVHRR GAC data due to resolution and calibration differences.

4.3.2.1 Look-Up Table Specification

AVHRR FRAC and AVHRR GAC look-up tables both have the same specifications. We define look up tables for spectral and textural components of the observations, which we assume to be independent in the Bayesian probability calculation. We define a single channel PDF using the 11 μm channel for use by AVHRR-1 instruments during the day (as these do not have a 12 μm channel).

Table 4-9: Single channel thermal spectral PDF specification.

Dimension	Unit	Upper Limit	Lower Limit	Bin Size	Number of Bins
11 μm BT	K	305.0	260.0	1.0	45
NWP SST	K	310.0	260.0	1.0	50
Path Length	-	2.4	1.0	0.35	4
Day/Night	Degrees	180.0	0.0	90.0	2

We define two thermal spectral PDFs that use two channels. The 11 and 12 μm PDF is used by AVHRR-2 and AVHRR-3 instruments, whilst the 3.7 and 11 μm PDF by the AVHRR-1 instruments.

Table 4-10: Two channel (11, 12 μm) thermal spectral PDF specification.

Dimension	Unit	Upper Limit	Lower Limit	Bin Size	Number of Bins
11 μm BT – NWP SST	K	10.0	-20.0	1.0	30
11-12 μm BT	K	9.0	-1.0	0.2	50
NWP SST	K	310.0	260.0	1.0	50
Path Length	-	2.4	1.0	0.35	4
Day/Night	Degrees	180.0	0.0	90.0	2

Table 4-11: Two channel (3.7, 11 µm) thermal spectral PDF specification.

Dimension	Unit	Upper Limit	Lower Limit	Bin Size	Number of Bins
11 µm BT – NWP SST	K	10.0	-20.0	1.0	30
3.7-11 µm BT	K	10.0	-6.0	0.2	80
NWP SST	K	310.0	260.0	1.0	50
Path Length	-	2.4	1.0	0.35	4
Day/Night	Degrees	180.0	0.0	90.0	2

The three-channel thermal spectral PDF is used when processing AVHRR-2 and AVHRR-3 data at nighttime.

Table 4-12: Three channel thermal spectral PDF specification.

Dimension	Unit	Upper Limit	Lower Limit	Bin Size	Number of Bins
11 µm BT – NWP SST	K	10.0	-20.0	1.0	30
11-12 µm BT	K	9.0	-1.0	0.2	50
3.7-11 µm BT	K	10.0	-6.0	0.2	80
NWP SST	K	310.0	260.0	2.5	20
Path Length	-	2.4	1.0	0.35	4
Day/Night	Degrees	180.0	0.0	90.0	2

All AVHRR sensors use the two-channel visible PDF using the 0.6 and 0.8 µm reflectance during the day. The 1.6 µm channel is not used in the visible cloud detection as it is rarely available throughout the AVHRR data record.

Table 4-13: Two channel visible spectral PDF specification.

Dimension	Unit	Upper Limit	Lower Limit	Bin Size	Number of Bins
0.6 µm refl	-	1.0	0.0	0.01	100
0.8 µm refl	-	1.0	0.0	0.01	100
Solar Zenith Angle	Degrees	95.0	0.0	2.5	38
Path Length	-	2.4	1.0	0.35	4

The 11 µm textural PDF is used day and night for all AVHRR sensors. For the AVHRR GAC PDFs we use the daytime cloudy PDF texture both day and night.

Table 4-14: 11 µm textural PDF specification.

Dimension	Unit	Upper Limit	Lower Limit	Bin Size	Number of Bins
11 µm texture	K	2.0	0.0	0.005	400
Path Length	-	2.4	1.0	0.35	4
Day/Night	Degrees	180.0	0.0	90.0	2

4.3.2.2 AVHRR FRAC Look-Up Tables

AVHRR FRAC probability density functions (PDFs) are initial derived using the EUMETSAT operational cloud mask and five years of data (2008-2013) during which this masking is known to be consistent. The PDFs are then iterated for a second time using the output of Bayesian cloud detection using the EUMETSAT-based PDFs as auxiliary input over the full data record (2006-2016).

The following figures show slices through some of the PDFs defined in the specification above. Figure 4-6 is a slice though the two-channel (10.8 and 12 µm) thermal PDF at a path length of 1-1.35 and NWP SST of 2808-281 K. The figure shows the differences between the day and nighttime PDFs. The distributions are similar, but with the nighttime PDF showing larger 10.8 µm – NWP SST differences.

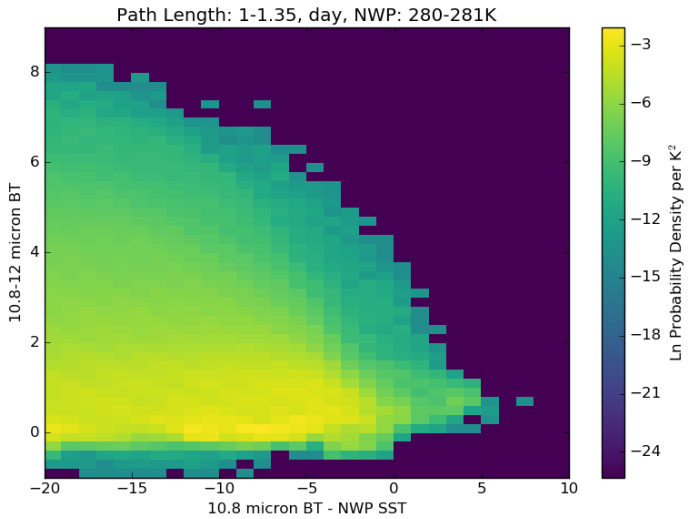

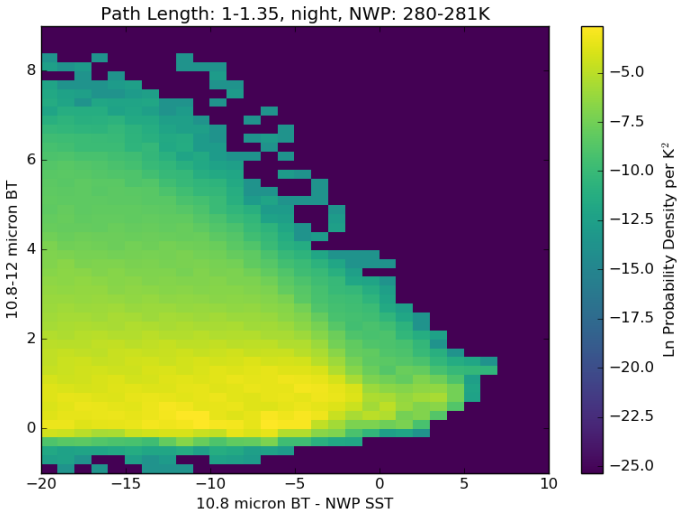

Figure 4-5: AVHRR FRAC two channel (10.8 and 12 µm) PDFs for daytime (top) and nighttime (bottom) for atmospheric path length of 1-1.35 and NWP SST of 280-281 K.

Figure 4-7 shows slices through the three-channel thermal PDFs for two different NWP SST bins (275-277.5 K and 290-292.5 K). The extent of the PDFs varies with NWP SST, with a reduction in the range of 10.8 µm - NWP SST differences at the positive end for higher NWP SST bins.

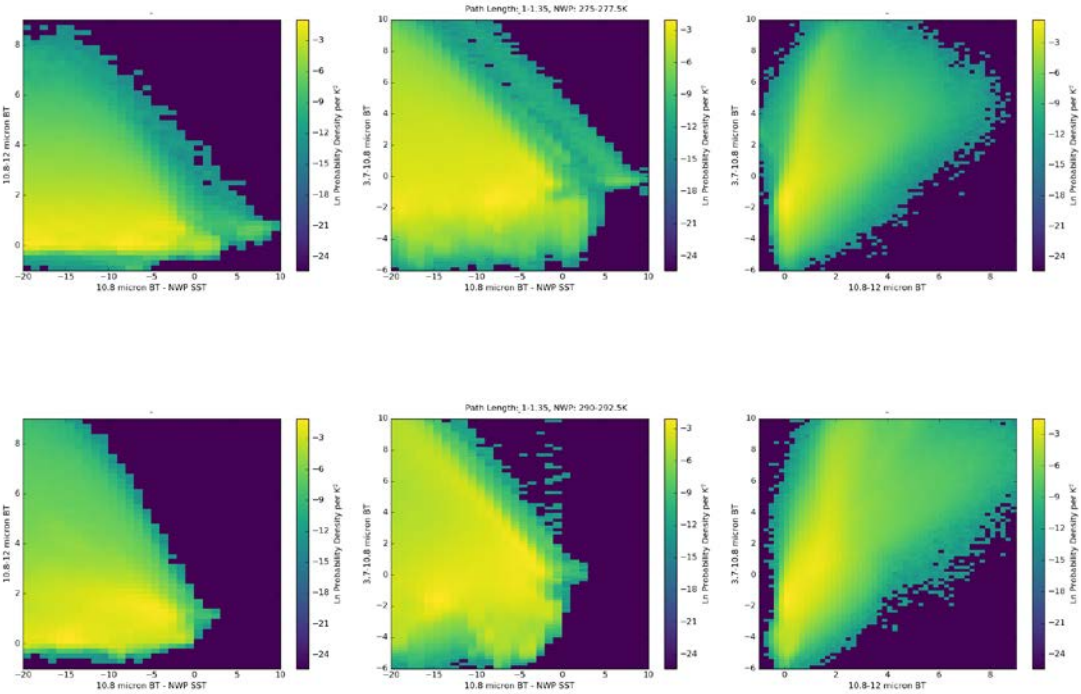

Figure 4-6: AVHRR FRAC three-channel (3.7, 10.8 and 12 µm) PDFs for two different NWP SST bins (275-277.5 K and 290-292.5 K). Atmospheric path length is constant at 1-1.35.

Figure 4-8 shows a slice through the two channel visible PDF (0.6 and 0.8 µm) for two different atmospheric path lengths (1-1.35 and 2.05-2.4) for a solar zenith angle of 37.5-40 degrees. At higher path lengths, the PDF is more compressed with fewer observations at high reflectance.

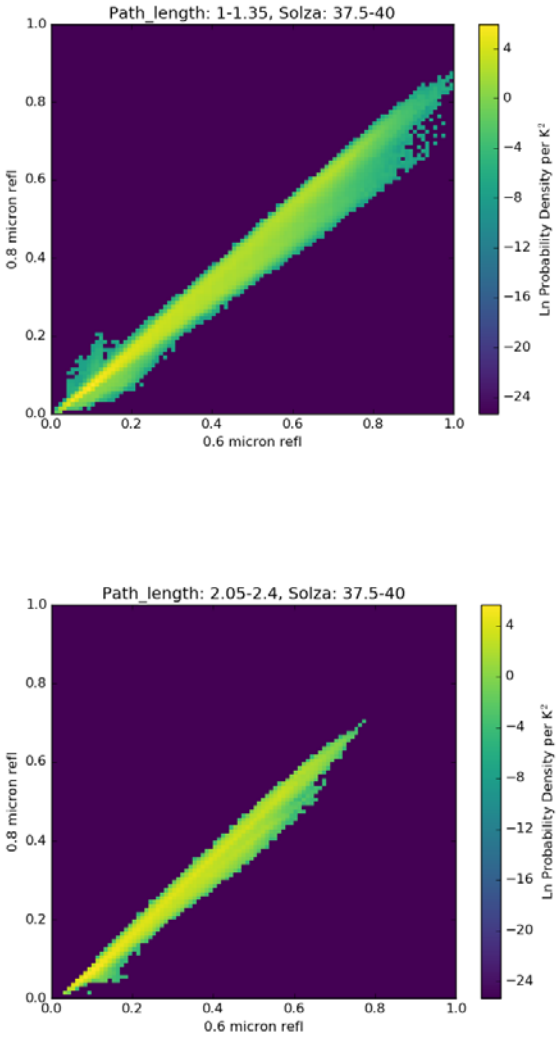

Figure 4-7: AVHRR FRAC two-channel visible PDFs for the 0.6 and 0.8 µm channels at two different path lengths (1-1.35 (top) and 2.05-2.4(bottom)), at a solar zenith angle of 37.5-40 degrees.

Figure 4-9 shows the textural PDFs for the 11 µm local standard deviation across 3x3 pixels for both clear-sky and cloudy observations. The plots show cloud (left), clear-sky (centre) and the ratio between them (right) for both day and night time observations. Some digitization is obvious at lower standard deviations, most clearly seen in the ratios at values < 0.2.

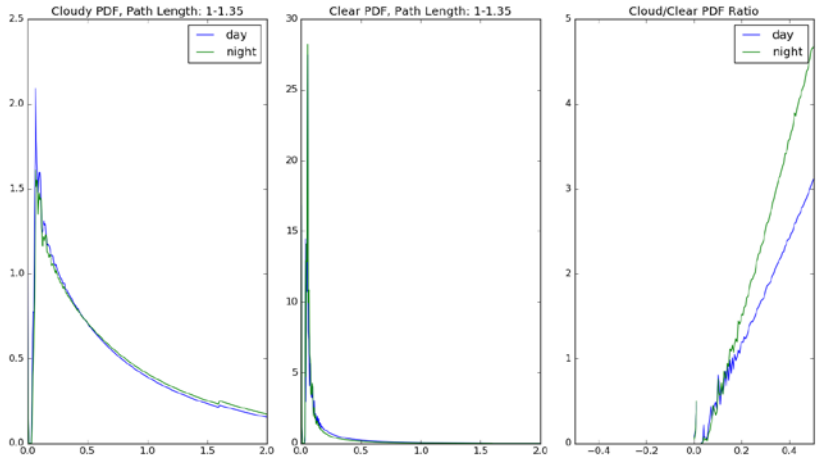

Figure 4-8: AVHRR FRAC 11 µm local standard deviation PDFs for cloud (left), clear-sky (centre), and the ratio (right).

4.3.2.3 AVHRR GAC Look-Up Tables

AVHRR GAC PDFs are generated from Metop-A data using the AATSR look-up tables. A brightness temperature shift is derived using RTTOV 11.3 infrared simulations to make the Metop-A GAC data 'look like' AATSR data at the point of performing the cloudy PDF look-up. This shift takes the form of a cubic, defined for two atmospheric path lengths (1.0 and 1.8) as a function of total column water vapour. A linear interpolation between the two sets of coefficients is implemented dependent on the path length of the given observation. The shifts are channel specific as defined below:

Figure 4-9: Brightness temperature shifts from Metop-A to AATSR.

Wavelength (µm)	Path Length	a3	a2	a1	a0
3.7	1.0	-7.13e-07	7.81e-05	-0.0029	0.0495
10.8	1.0	4.33e-07	-6.37e-05	0.0016	-0.0059
12.0	1.0	5.53e-07	3.69e-06	-0.014	-0.31
3.7	1.8	-1.19e-06	0.00013	-0.0044	0.094
10.8	1.8	7.14e-07	-9.71e-05	0.0025	-0.0094
12.0	1.8	3.21e-06	-0.00021	-0.0099	-0.47

AVHRR GAC PDFs generated from Metop-A data are used for cloud detection with GAC data from all the AVHRR sensors. The equator overpass time of the different AVHRR sensors is variable according to whether they are morning or afternoon satellites and orbit drift over the instrument lifetime. Figure X below shows the equator overpass time for the different AVHRR sensors.

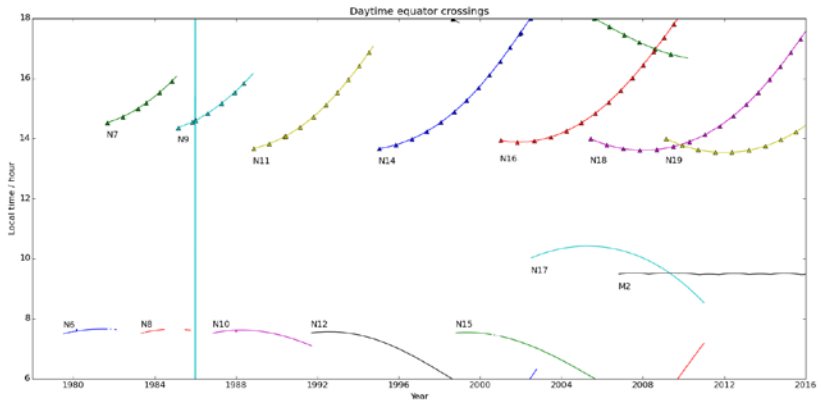

Figure 4-10: AVHRR equator overpass times

Metop-A remains in a stable orbit over its lifetime and as a consequence does not make observations at solar zenith angle below ~32.5 degrees (dependent on path length), and a consequence, some bins of the visible channel PDF remain unpopulated. To enable these PDFs to be used with other instruments, these unpopulated bins are modified by extrapolation from well-populated solar zenith angle bins for each given path length.

A brightness temperature shift (similar to the one described above in the PDF generation) is also required to use Metop-A PDFs with other AVHRR instruments. These shifts are cubic in form and channel dependent as a function of total column water vapour (Table 4-15). The coefficients were obtained using radiative transfer simulation to relate expected clear-sky brightness temperatures for other AVHRRs to Metop-A for the equivalent channels. Shifts are not required when using the visible channel look-up tables or textural PDFs.

Table 4-15: Brightness temperature shifts for all AVHRR sensors to Metop-A for cloudy PDF look-up.

Instrument	Wavelength (μm)	Path Length	a3	a2	a1	a0
NOAA-19	3.7	1.0	2.56e-07	-3.34e-05	0.00016	-0.027
	10.8	1.0	1.29e-07	-2.27e-05	3.57e-05	-0.0011
	12.0	1.0	-1.07e-07	-2.91e-05	0.12	0.21
	3.7	1.8	3.73e-07	-4.76e-05	0.00017	-0.037
	10.8	1.8	3.04e-07	-4.31e-05	0.0057	-0.0064
	12.0	1.8	-2.17e-06	0.00014	0.0073	0.32
NOAA-18	3.7	1.0	-4.61e-07	2.86e-05	-0.0031	0.031
	10.8	1.0	1.047e-07	-2.01e-05	0.00013	-0.00896
	12.0	1.0	-2.13e-07	-2.45e-06	0.0067	0.131
	3.7	1.8	-7.95e-07	5.66e-05	-0.0048	0.058
	10.8	1.8	2.598e-07	-3.9996e-05	0.00082	-0.023
	12.0	1.8	-1.61e-06	0.00012	0.0037	0.211

Instrument	Wavelength (μm)	Path Length	a3	a2	a1	a0
NOAA-17	3.7	1.0	1.53e-07	-2.42e-05	-0.00034	-0.019
	10.8	1.0	2.38e-08	-6.99e-06	-0.00025	-0.00015
	12.0	1.0	8.3e-08	-1.95e-05	2.45e-05	-0.031
	3.7	1.8	1.88e-07	-3.03e-05	-0.00065	-0.023
	10.8	1.8	1.26e-07	-1.75e-05	-1.25e-05	-0.0028
	12.0	1.8	5.38e-07	-7.44e-05	0.0022	-0.068
NOAA-16	3.7	1.0	3.36e-06	-0.00032	0.013	-0.33
	10.8	1.0	-2.99e-07	1.068e-05	0.00059	0.021
	12.0	1.0	-8.48e-08	-3.52e-05	0.0079	0.11
	3.7	1.8	5.12e-06	-0.00049	0.019	-0.504
	10.8	1.8	-9.81e-07	0.00015	-0.0016	0.06
	12.0	1.8	-9.498e-07	1.71e-05	0.0075	0.16
NOAA-15	3.7	1.0	3.15e-06	-0.000298	0.118	-0.315
	10.8	1.0	-3.11e-08	6.43e-06	-0.0002	-0.0016
	12.0	1.0	8.13e-08	-1.78e-05	-0.00029	-0.031
	3.7	1.8	4.796e-06	-0.00046	0.017	-0.479
	10.8	1.8	-6.8e-08	1.14e-05	-0.00034	-0.0021
	12.0	1.8	5.71e-07	-7.63e-05	0.0019	-0.068
NOAA-14	3.7	1.0	-9.168e-07	7.01e-05	-0.0057	0.0398
	10.8	1.0	3.49e-07	-5.83e-05	0.00104	0.01398
	12.0	1.0	-4.88e-08	-1.29e-05	0.0047	0.0837
	3.7	1.8	-1.67e-06	0.00014	-0.0092	0.085
	10.8	1.8	7.35e-07	-0.0001	0.0022	0.018
	12.0	1.8	-8.87e-07	5.91e-05	0.0029	0.137
NOAA-12	3.7	1.0	-1.09e-06	8.42e-05	-0.007	0.039
	10.8	1.0	-1.795e-07	3.86e-05	0.00068	0.036
	12.0	1.0	6.86e-08	-2.97e-05	0.0038	0.041
	3.7	1.8	-1.98e-06	0.00017	-0.11	0.086
	10.8	1.8	-6.35e-07	8.899e-05	-0.00058	0.0697
	12.0	1.8	-1.84e-07	-2.07e-05	0.0042	0.049
NOAA-11	3.7	1.0	7.52e-07	-7.62e-05	0.0029	-0.062
	10.8	1.0	-.23e-08	-1.69e-05	-0.0003	-0.0069

Instrument	Wavelength (μm)	Path Length	a3	a2	a1	a0
	12.0	1.0	2.93e-07	-4.56e-05	-0.0011	-0.068
	3.7	1.8	1.15e-06	-0.0012	0.0043	-0.093
	10.8	1.8	2.62e-07	-3.48e-05	4.75e-05	-0.017
	12.0	1.8	1.40e-06	-0.00017	0.0032	-0.14
NOAA-10	3.7	1.0	2.56e-07	-3.31e-05	3.06e-05	-0.039
	10.8	1.0	-1.08e-06	0.00021	-0.0023	0.041
	3.7	1.8	3.15e-07	-4.13e-05	-0.00021	-0.04996
	10.8	1.8	-2.79e-06	0.000401	-0.0076	0.115
NOAA-09	3.7	1.0	9.61e-07	-9.17e-05	0.0039	-0.081
	10.8	1.0	1.91e-07	-3.66e-05	-0.00026	-0.009
	12.0	1.0	3.81e-07	-6.296e-05	-0.00199	-0.118
	3.7	1.8	1.47e-06	-0.00014	0.0057	-0.123
	10.8	1.8	5.37e-07	-7.45e-05	0.0006	-0.025
	12.0	1.8	2.16e-06	-0.00026	0.0048	-0.243
NOAA-08	3.7	1.0	-8.08e-07	5.83e-05	-0.006	0.0069
	10.8	1.0	-6.82e-07	0.00013	-0.0092	0.0299
	3.7	1.8	-1.51e-06	0.00012	-0.0096	0.035
	10.8	1.8	-1.95e-06	0.00028	-0.0046	0.081
NOAA-07	3.7	1.0	4.54e-07	-4.78e-05	0.0016	-0.042
	10.8	1.0	2.85e-08	-1.16e-05	-9.51e-05	-0.003
	12.0	1.0	2.11e-07	-4.55e-05	0.0013	-0.032
	3.7	1.8	6.52e-07	-6.87e-05	0.0022	-0.059
	10.8	1.8	1.58e-07	-2.29e-05	0.00015	-0.00897
	12.0	1.8	8.19e-07	-0.00012	0.0045	-0.083
NOAA-06	3.7	1.0	-2.39e-06	0.00021	-0.013	0.128
	10.8	1.0	-7.47e-07	0.00015	-0.0012	0.031
	3.7	1.8	-4.38e-06	0.0004	-0.021	0.243
	10.8	1.8	-2.17e-06	0.00031	-0.0055	0.09

Figure 4-12 shows the brightness temperature shifts from all AVHRR sensors to Metop-A as given in Table 1.12, as a function of total column water vapour and for the two different path lengths. Shifts for three channels are shown: 3.7 μm (left), 10.8 μm (centre) and 12 μm (right).

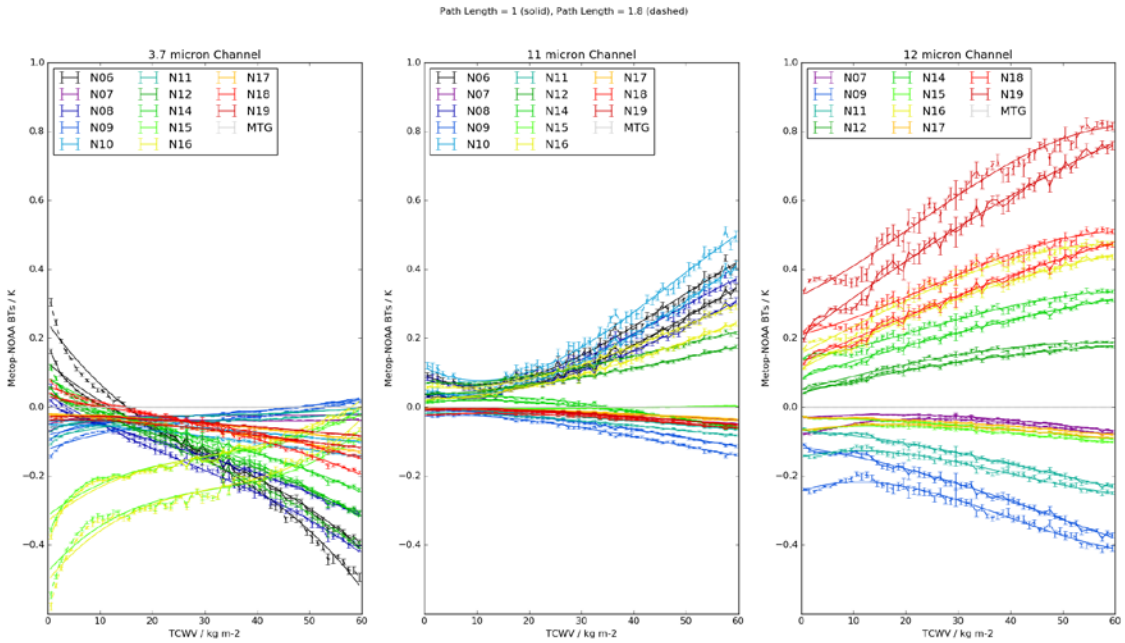

Figure 4-11: Brightness temperature shifts for all AVHRR sensors to Metop-A for three infrared channels; 3.7, 10.8 and 12 µm. Bars, +/-1 sigma range of simulated differences. Lines, fitted transformation function.

The following figures show some slices through the AVHRR GAC PDFs. Figure 4-13 compares the PDF of the 10.8-12 µm and 10.8 µm – NWP SST differences between day and night. The atmospheric path length bin is 1-1.35 and the NWP SST is 280-281 K. The PDFs are consistent between day and night as would be expected for infrared wavelengths.

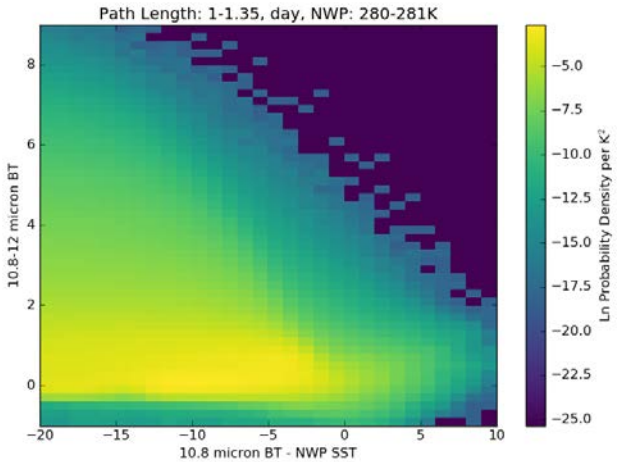

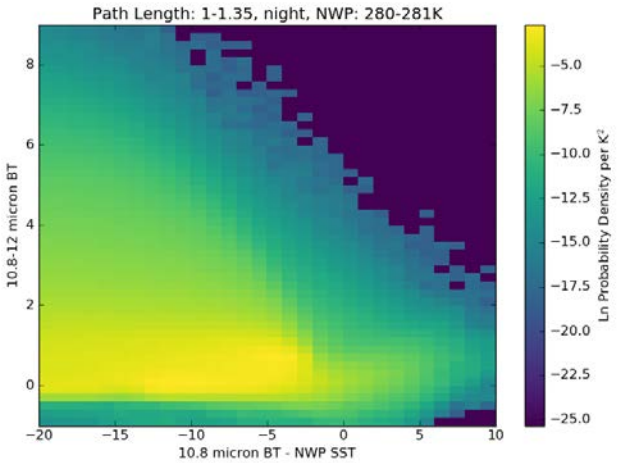

Figure 4-12: AVHRR GAC two channel (10.8 and 12 µm) PDFs for daytime (top) and nighttime (bottom) for atmospheric path length of 1-1.35 and NWP SST of 280-281 K.

Figure 4-14 shows slices three different slices through the three channel (3.7, 10.8 and 12 µm) thermal PDFs for two different NWP SSTs (275-277.5 K and 290-292.5 K). The PDF changes shape with variation in the NWP SST.

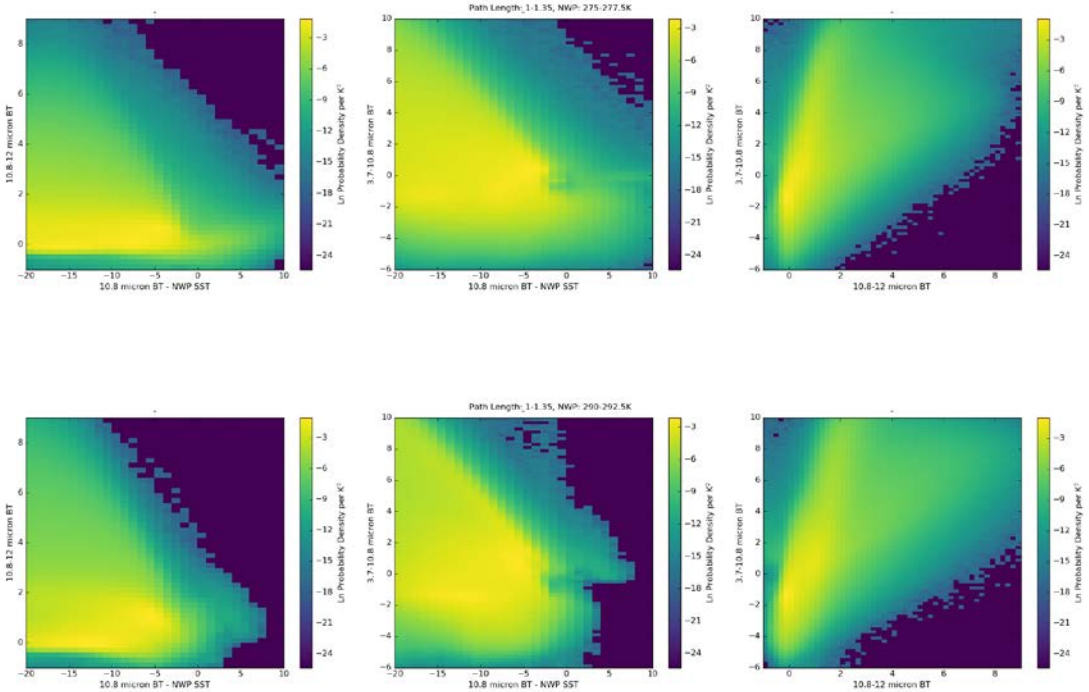

Figure 4-13: AVHRR GAC three-channel (3.7, 10.8 and 12 µm) PDFs for two different NWP SST bins (275-277.5 K and 290-292.5 K). Atmospheric path length is constant at 1-1.35.

Figure 4-15 shows the 0.6 and 0.8 µm visible channel PDFs for two different path lengths (1-1.35 and 2.05-2.4). At longer path lengths, the PDF is compressed, with lower maximum reflectance observed.

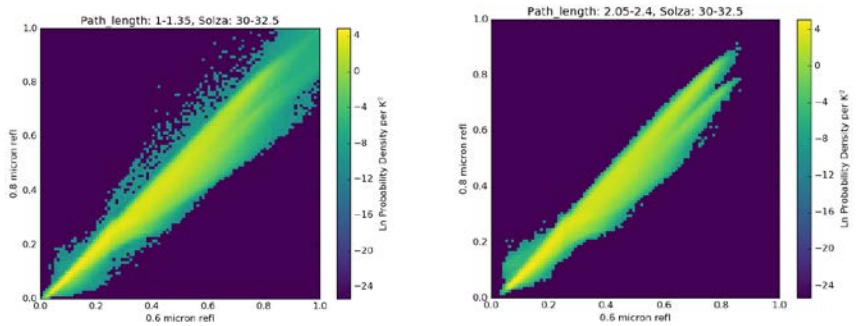

Figure 4-14: AVHRR GAC two-channel visible PDFs for the 0.6 and 0.8 µm channels at two different path lengths (1-1.35 (top) and 2.05-2.4(bottom)), at a solar zenith angle of 30-32.5 degrees.

Figure 4-16 shows the textural PDFs for cloud (left), clear-sky (centre) and the ratio between the two (right). The daytime PDFs are used at night. The PDFs show some digitization, particularly at low 11 µm 3x3 pixel standard deviations. The digitization effects are less apparent in the ratio above ~0.1.

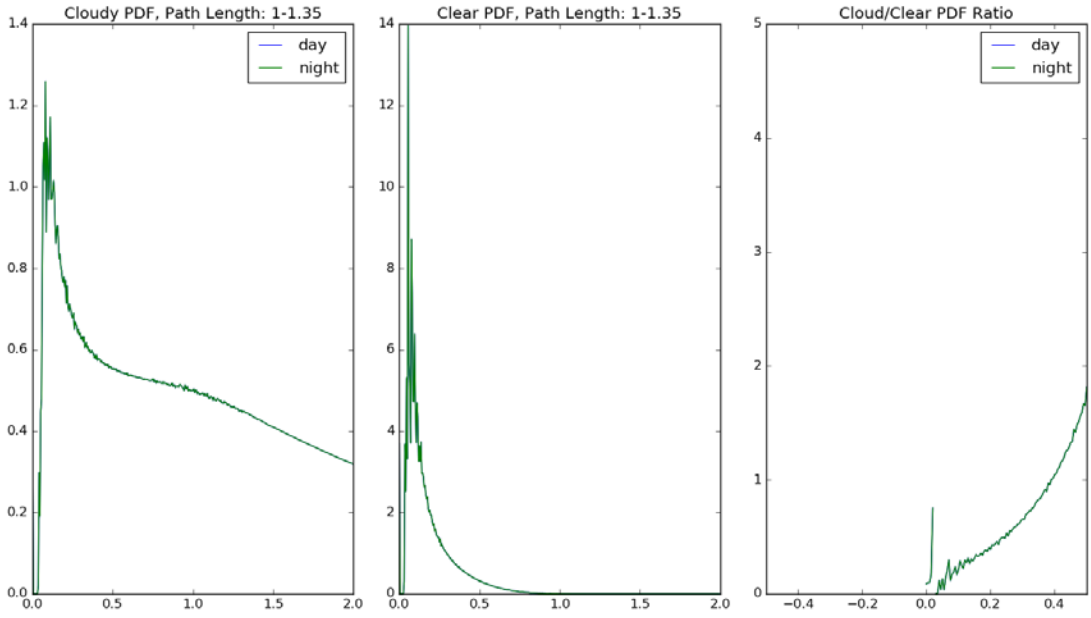

Figure 4-15: AVHRR GAC 11 µm local standard deviation PDFs for cloud (left), clear-sky (centre), and the ratio (right).

The prior clear-sky probability is calculated using 1 – Total Cloud Cover (TCC) as specified in the ECMWF ERA-Interim data. This provides a more dynamic specification of prior clear-sky probability than a static map including seasonal variability. Limits are placed on the prior clear-sky probabilities of 0.1 and 0.5 where 1 – ECMWF TCC exceeds these values.

4.3.2.4 Forward Model

A single forward model is used in the cloud detection scheme, supporting both infrared and visible wavelength radiative transfer simulations, a capability of the RTTOV 11.3 released currently used. NWP atmospheric profile and surface conditions are used as input and the model is run at AVHRR geolocation tie-points. The outputs are then interpolated to the pixel location. Tangent linears are calculated with respect to the elements of the reduced state vector ($\mathbf{x}_b$) for the calculated brightness temperature or reflectance.

$$\boldsymbol{x}^b = \begin{bmatrix} SST^b \\ TCWV^b \\ \boldsymbol{u}_{10}^b \\ AOD^b \end{bmatrix}$$

where:

SST	is sea surface temperature
TCWV	is total column water vapour
$\boldsymbol{u}_{10}$	is the 10 m wind vector
AOD	is aerosol optical depth.

Forward model performance in the visible channels (0.6, 0.8 μm) was assessed using test scenes from FRAC data and clear-sky matches from a match up dataset (MMD). The Bayesian cloud detection for the ATSR instruments did not routinely use the short wave visible channels and until the release of RTTOV v11, this did not support visible channel simulations. Comparisons were made between the observed and simulated reflectance using the MMD. The visible channel observations use the 2015 CSSP calibration coefficients. It was found that RTTOV consistently underestimated reflectance in the 0.6 and 0.8 μm channels for all AVHRR sensors in glint free regions (< 0.12 reflectance) as shown in Figure 4-17.

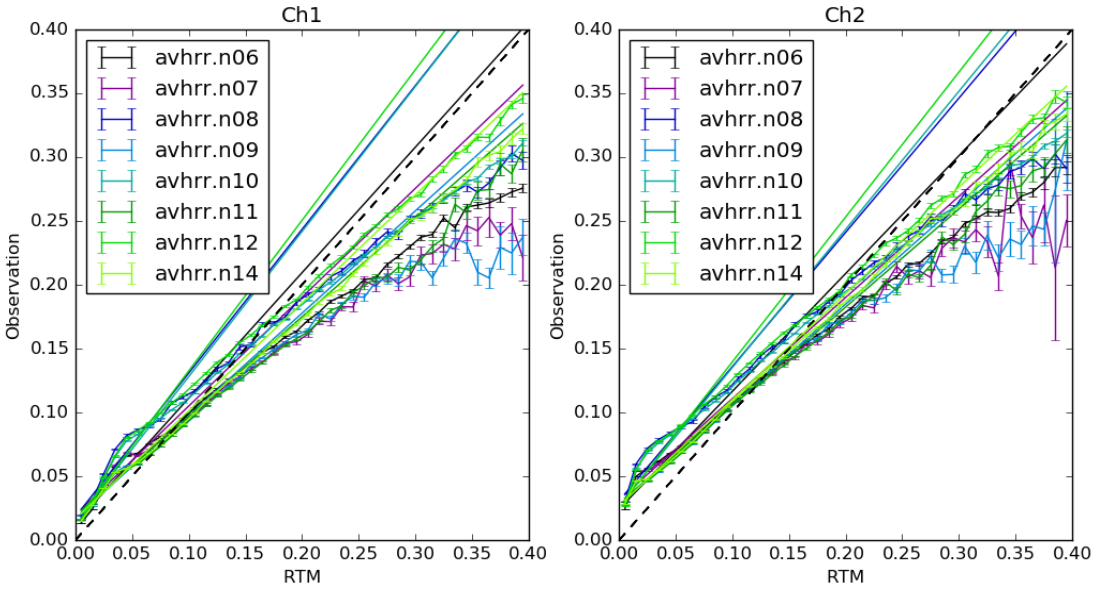

Figure 4-16 RTTOV 11.3 comparisons to observations in the 0.6 and 0.8 µm for all AVHRR sensors using a match-up dataset. Bars, +/- 1 sigma robust standard error in mean of observed reflectance in bins of simulated reflectance. Coloured straight lines, weighted ordinary least squares best fit to data in bins of low (<0.12) RTM reflectance, for individual AVHRRs. Black line: fit applied for all AVHRRs.

The underestimation is consistent across all AVHRR sensors, so a single correction is applied to the RTTOV simulation of the 0.6 and 0.8 µm channels for all AVHRR instruments. The corrections are as follows:

$$RTTOV_{0.6} = (RTTOV_{0.6} * 0.88697) + 0.016$$

$$RTTOV_{0.8} = (RTTOV_{0.8} * 0.84455) + 0.011$$

The clear-sky match-ups were also used to determine the diagonal terms of the forward model covariance matrix (**S**) using robust statistics to minimize the influence of any undetected cloud in the match-ups. The off-diagonal terms of this matrix between the 0.6 and 0.8 µm channels was also calculated using these matches giving a high correlation between the two channels of 0.96. This was tested using regions of sunglint and shallow water where the ocean colour at the two different wavelengths may be expected to differ. Figure 4-18 below shows an example of a sunglint region, giving the 0.6 µm data, the 0.6 µm RTTOV simulation.

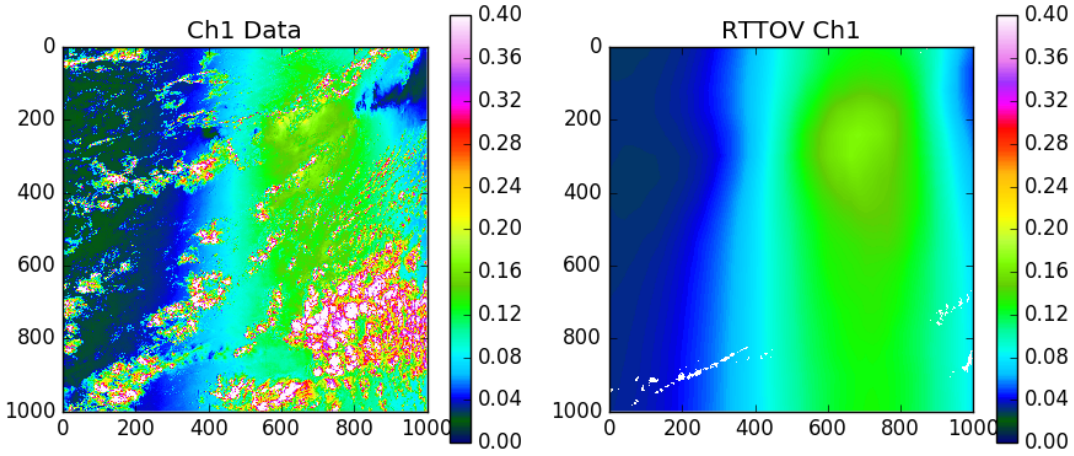

Figure 4-17: Observations (including clear and cloudy areas) and simulations (based on clear sky assumption) of the 0.6 um channel in a sunglint region.

Figure 4-19 below shows the corresponding cloud detection (using all channels in the observation vector). The plot on the left uses a high correlation between the visible channels in the forward model covariance matrix, **S**, whilst in the right-hand plot this correlation is relaxed to 0.5. We find that relaxing the off-diagonal correlation term significantly improves the cloud detection skill in sunglint regions, particularly where the glint is weaker.

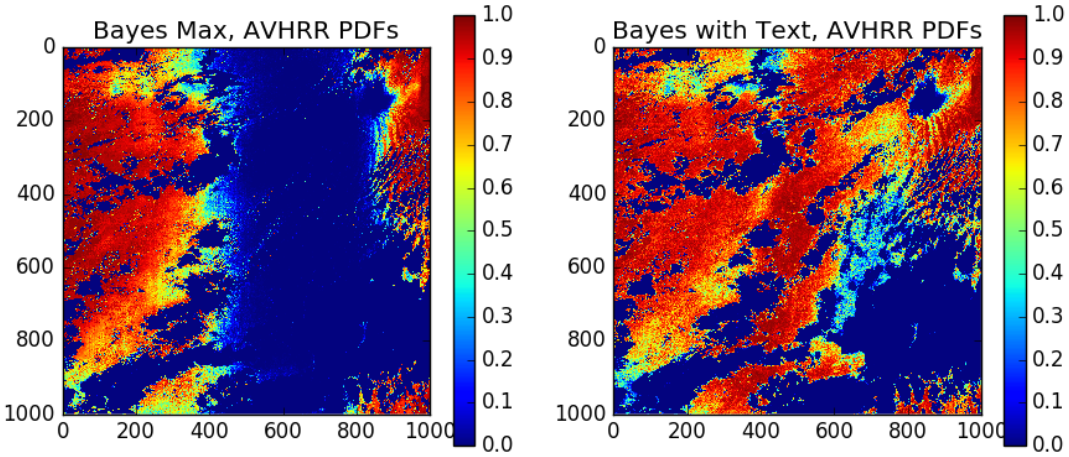

Figure 4-18: Cloud detection in a sunglint region assuming high error correlation (r = 0.96) between the visible channels (left) and a relaxed correlation (r = 0.5) between visible channels (right). The relaxed assumption is seen to be needed to avoid the over-masking of the sunglint area.

The forward model covariance matrix used for the 0.6 and 0.8 μm channels for all AVHRR sensors is as follows:

$$\mathbf{S}_{0.6,0.8} = \begin{bmatrix} 0.000032801 & 0.000014358 \\ 0.000014358 & 0.000025138 \end{bmatrix}$$

4.3.2.5 Cloud Detection Performance

Implementation of the Bayesian cloud detection for the AVHRR instruments was undertaken in order to improve the cloud detection skill over the operational cloud masking schemes. Performance has been scrutinised in a range of conditions swath data, for FRAC and GAC. As a means of assessing the overall performance for SST retrieval, we compare validation statistics using two cloud masks.

Our previous observation was that for some AVHRRs, CLAVR-x was passing too much cloud as clear. We expect, therefore, the Bayesian detection to reduce the number of matches, as cloud pixels are eliminated. If the "correct" pixels are being eliminated, measures of scatter of the SST retrievals should also reduce, whereas if the additional exclusions were effectively random, the spread would stay the same.

Therefore, in Tables 1.13, 1.14 and 1.15 we show the ratios of the number of matches, of the standard deviation (SD) and the robust standard deviation (RSD). Ideally, all these ratios should be below 1.

Typically, we find that Bayesian cloud detection reduces by 15% the total number of matches compared to CLAVR-X; at the same time, there is a significant reduction in the standard deviation and robust standard deviation, as shown by ratios less than 1. In some cases, the robust standard deviation does not show an improvement (ratio ~1), but the standard deviation does, showing a reduction in outliers caused by cloud contamination in the match-ups, but no improvement in the spread of the majority of data. In other cases, the two cloud detection systems seem to be comparable in performance.

These statistics were compiled using processing earlier than EXP 1.8 with a less good set of AVHRR calibrations. Since the Bayesian method depends on the degree of discrepancy between simulations and observations and these discrepancies should be reduced by improved calibration, the results may be pessimistic relative to the true EXP 1.8 performance.

Table 4-16: N2 daytime retrieval statistics, Bayesian/CLAVR-X for AVHRR GAC instruments (N4 for AHVRR-1 instruments).

Instrument	Ratio of matches	Ratio of Standard Deviation	Ratio of Robust Standard Deviation
NOAA-19	0.83	0.68	0.85
NOAA-18	0.85	0.62	0.88
NOAA-17	0.97	0.99	1.02
NOAA-16	0.99	0.87	1.008
NOAA-15	0.93	0.77	0.97
NOAA-14	0.96	0.93	0.97
NOAA-12	1.05	0.82	0.995
NOAA-11	0.84	0.87	0.94
NOAA-10	0.81	0.72	0.93
NOAA-09	0.87	0.86	0.91
NOAA-08	0.73	0.72	0.99
NOAA-07	0.82	0.83	0.91
NOAA-06	0.87	0.57	0.85

Table 4-17: N2 nighttime retrieval statistics, Bayesian/CLAVR-X for AVHRR GAC instruments (N4 for AHVRR-1 instruments).

Instrument	Ratio of matches	Ratio of Standard Deviation	Ratio of Robust Standard Deviation
NOAA-19	0.92	0.68	0.92
NOAA-18	0.88	0.72	0.96
NOAA-17	0.85	0.92	0.98
NOAA-16	0.92	0.96	1.05
NOAA-15	0.82	0.94	0.98
NOAA-14	0.96	1.004	1.02
NOAA-12	1.06	0.99	1.03
NOAA-11	0.79	0.92	0.95
NOAA-10	0.72	0.88	0.999
NOAA-09	0.66	0.78	0.93
NOAA-08	0.74	0.97	0.97
NOAA-07	0.43	0.77	0.92
NOAA-06	0.62	0.63	0.76

Table 4-18: N3 nighttime retrieval statistics, Bayesian/CLAVR-X for AVHRR GAC instruments (N2 for AHVRR-1 instruments).

Instrument	Ratio of matches	Ratio of Standard Deviation	Ratio of Robust Standard Deviation
NOAA-19	0.92	0.67	0.95
NOAA-18	0.88	0.7	0.98
NOAA-17	0.85	0.88	0.97
NOAA-16	0.92	0.88	1.04
NOAA-15	0.82	0.89	1.007
NOAA-14	0.96	0.93	1.04
NOAA-12	1.06	0.86	0.99
NOAA-11	0.79	0.88	1.004
NOAA-10	0.72	0.44	0.74
NOAA-09	0.66	0.71	0.87
NOAA-08	0.74	0.89	0.80
NOAA-07	0.43	0.54	0.58
NOAA-06	0.62	0.36	0.68

4.4 Clear-sky Detection for Advanced Very High Resolution Radiometers – High Latitudes Extension

This subsection gives details of the SST-CCI cloud-clearing algorithm extension at high latitudes for AVHRR instruments. The cloud clearing step prior to SST calculation is based on Bayesian cloud probability calculation as described in the previous section. After the cloud clearing step an additional Bayesian ice and cloud masking step is applied under conditions where sea ice might be expected.

At high latitudes it can be difficult to distinguish between open water that often contains strong thermal gradients and sea ice, especially where the surface temperature is close to the point of phase change between open water and ice. The additional clear-over-ice class improves the skill of the algorithm to identify open ocean cases required for SST retrieval purposes. It also enables identification of sea-ice surfaces for potential ice surface temperature retrieval.

4.4.1 Algorithm Description

4.4.1.1 Algorithm Overview

This chapter describes the AVHRR cloud and ice mask algorithm to be applied in the SST-CCI SST retrieval following the SST calculation. It describes an algorithm that classifies each AVHRR GAC swath pixel as clear-open-water, ice covered or cloudy. These three classes are represented using PDFs. These PDFs are used in a naive Bayesian approach to calculate the probability of these three classes, for each pixel.

4.4.1.2 Processing Outline

The cloud and ice masking for the AVHRR retrieval is split in two stages. CLAVR-x described in section 4.2, and the high-latitude extension described here. The high latitude step can be run either directly after the cloud detection step, or at a later stage, and is run on all pixels which have been classified as clear-open-water by the cloud detection step. A flow chart for the high latitude extensions is shown below (Figure 4-20).

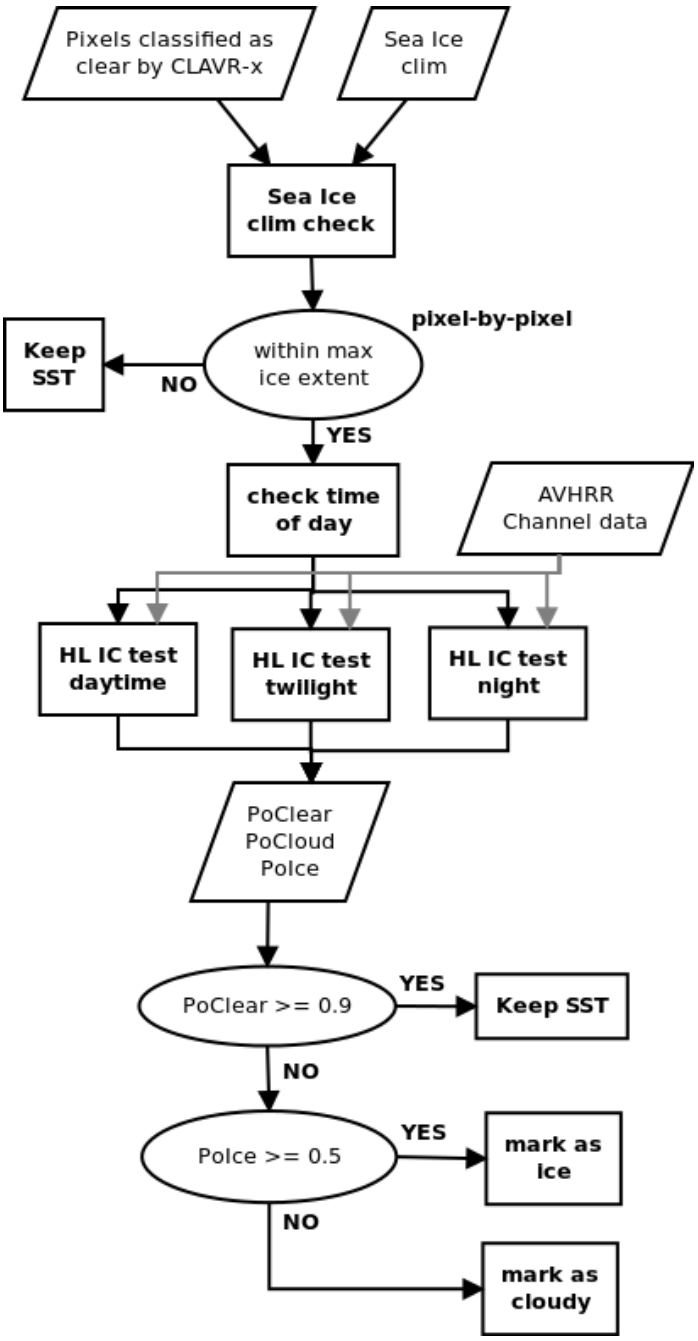

Figure 4-19. Flow chart for high latitude ice and cloud masking.

4.4.1.3 High Latitude cloud and ice masking step

The High Latitude cloud and ice masking shown in the flow chart in Figure 4-8 has been developed in the SST-CCI project. It is described in full detail here.

The High Latitude step is run on all pixels classified as clear-open-water by cloud detection. The pixel is checked against a monthly maximum sea ice extent climatology, which is described in section 4.4.2.2. If the pixel is outside the area of maximum sea ice extent for the relevant month, no further tests are performed on that pixel and the estimated SST value is kept.

For those pixels that fall within the maximum sea ice extent, the time of day is checked and a daytime, twilight or nighttime ice and cloud probability calculation test is run. The outputs from these tests are the same; the probability of pixel being clear-open-water, cloud covered and ice covered (Po_{Clear}, Po_{Cloud}, Po_{Ice}). These probabilities are calculated using a naive Bayesian approach, as described in more detail in RD.274.

Finally, if Po_{Clear} is larger than 0.9, the pixel is regarded as clear of cloud and ice, and the SST estimate is kept. If not, it is regarded as cloud covered or ice covered. If Po_{Ice} is larger than 0.5 the pixel is classified as ice, otherwise it is classified as cloud.

4.4.2 Inputs to AVHRR High Latitude Extension

4.4.2.1 Primary Sensor Data

The satellite data used are AVHRR-GAC data from the satellites NOAA-12, 14, 15, 16, 17, 18, 19 and METOP-2, and include satellite and sun geometry data. The channel combinations used are as follows:

$re_{0.9}/re_{0.6}$ ratio between the reflectance in the 0.9 µm and 0.6 µm channels (AVHRR channel 2 and AVHRR channel 1)

$re_{1.6}/re_{0.6}$ ratio between the reflectance in the 1.6 µm and 0.6 µm channels (AVHRR channel 3A and AVHRR channel 1). [Not available for AVHRR-1 and AVHRR-2 sensors, and NOAA 12 and 14].

$bt_{3.7} - bt_{11}$ difference in brightness temperature of the 3.7 µm and 11 µm channels, (AVHRR channel 3/3B and channel 4)

$bt_{3.7} - bt_{12}$ difference in brightness temperature of the 3.7 µm and 12 µm channels, (AVHRR channel 3/3B and channel 5)

$LSD(bt_{3.7} - bt_{12})$ local standard deviation in the difference between the 3.7 µm and 11 µm channels.

The LSD operator is described in section 2.3.3.1.

In addition the following satellite geometry data are used:

- SOZ – solar zenith angle.

4.4.2.2 Ancillary Data

The cloud and ice masking algorithm takes as input monthly maximum sea ice extent climatology to define the area across which sea ice detection is attempted. This climatology is based on an ocean mask from the National Snow and Ice Data Centre (NSIDC), available here:

http://nsidc.org/data/smmr_ssmi_ancillary/ocean_masks.html.

This climatology has been produced by NSIDC using the Scanning Multichannel Microwave Radiometer (SMMR) and the Special Sensor Microwave/Imager (SSM/I) monthly averaged ice concentrations and finding the maximum extent for each month between 1979 and 2007. A zone of 350 km has been added to the maximum extent NSIDC maps to insure that the masks extend beyond the areas where sea ice is ever likely to occur. This climatology is provided at 12.5 km resolution, on a Lambert Azimuthal projection in NetCDF3 format. Examples are shown in Figure 4-9.

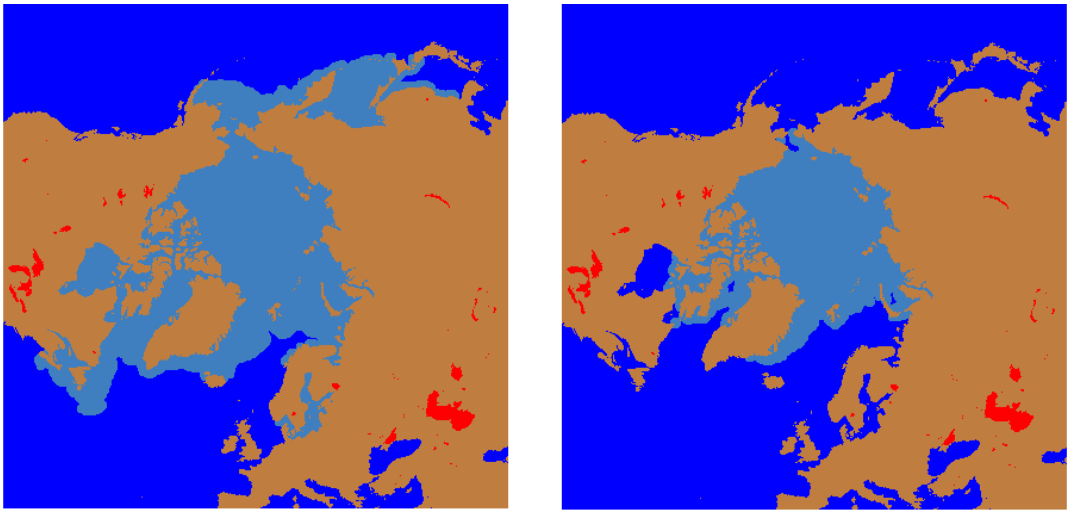

Figure 4-20. Climatological maximum sea ice extent during March (left) and September (right). Lakes without climatology are marked in red.

4.4.3 Mathematical Description of AVHRR High Latitude Extension

This section describes the theoretical parts of the algorithm in more details.

4.4.3.1 Physical principles and equations

This section describes the physical and mathematical symbols and formulas used in the description of the algorithm.

Following is a summary of the symbols used to define the algorithm.

Po_{Clear}

The probability of a pixel being clear-open-water.

Po_{Cloud}

The probability of a pixel being cloud covered.

$\boldsymbol{Po_{\text{Ice}}}$

The probability of a pixel being covered by ice.

$\boldsymbol{LSD(x)}$

Local standard deviation, defined as the standard deviation of the variable x in a 3x3 pixel matrix around the data point in question, including the data point itself. In the case where the data point is on a swath line edge, LSD is defined as the standard deviation of the remaining closest neighbour points around the data point.

$\boldsymbol{dist_{\text{WTP}}(x), dist_{\text{WTP}}(x,y)}$

Distance between observation x in a certain channel feature (channel value or channel combination) and a water tie-point (WTP) of this channel feature. The water tie-point is the mean value for this feature over clear-open-water. The mean value is found by selecting all pixels in the training data set that are classified as clear-open-water and then finding the average of those pixels in the given channel feature. This clear-open-water tie-point might itself depend on another channel feature $\boldsymbol{y}$ (such as solar zenith angle or $bt_{11} - bt_{12}$).

$\boldsymbol{NormalDist(x,M,S)}$

Probability distribution value of x in a normal distribution with mean M and standard deviation S, defined as

$$NormalDist(x,M,S) = S\sqrt{2\pi} * e^{\left(\frac{-pow((x-M),2.0)}{2*pow(S,2.0)}\right)}$$

$\boldsymbol{LogNormalDist(x,M,S)}$

Probability distribution value of x in a log normal distribution. In this distribution the natural logarithm of the variable has a normal distribution with mean M and standard deviation S. The probability distribution function is defined as

$$LogNormalDist(x,M,S) = \frac{1}{C}e^{-0.5z^2}$$

where

$$z = \frac{(\log(x) - M)^2}{S^2}$$

$$C = x * S * \sqrt{2\pi}$$

$\boldsymbol{prob(\text{var}|\text{class},\text{x})}$

Probability of an observation x from the variable var, given that that surface observed is of a given surface class (clear-over-water, sea-ice, or cloud). This probability depends on the probability density function chosen for this variable and class. For the high latitude ice and cloud algorithm only normal and log-normal distributions are used, and hence this probability density function is one of these two functions:

$$prob_N(\text{var}|\text{class},\text{x}) = \text{NormalDist}\big(\text{x}, \text{M}(\text{var},\text{class}), \text{S}(\text{var},\text{class})\big)$$

$$prob_{LN}(\text{var}|\text{class}, x) = LogNormalDist\big(x, M(var, class), S(var, class)\big)$$

Bayesian probabilities for Ice, Water and Cloud

The functions for calculating the Bayesian probabilities of ice, water and cloud depends on how many variables are used. The high latitude ice and cloud masking algorithm uses two variables, var1 and var2. These two variables are the selected AVHRR channel combinations that have been shown to be the best suited for separating ice, water and cloud (e.g. $RE_{1.6}$, $RE_{0.6}$) [RD.318]. As described in SST-CCI RD.274, the probabilities for the three classes given observation x in var_1 and y in var_2 can then be written as follows:

$$BayesProb_{\text{Ice}}(x, y) = prob(var_1|ice, x) * \frac{prob(var_2|ice, y)}{p_{sum}(x, y)}$$

$$BayesProb_{\text{Water}}(x, y) = prob(var_1|water, x) * \frac{prob(var_2|water, y)}{p_{sum}(x, y)}$$

$$BayesProb_{\text{Cloud}}(x, y) = prob(var_1|cloud, x) * \frac{prob(var_2|cloud, y)}{p_{sum}(x, y)}$$

where

$$p_{\text{sum}}(x, y) = prob(var_1|ice, x) * prob(var_2|ice, y) + prob(var_1|water, x) * prob(var_2|water, y) + prob(var_1|cloud, x) * prob(var_2|cloud, y)$$

4.4.3.2 Calculations

This section describes the algorithm calculations in detail.

The high latitude ice and cloud masking extension has three main stages, as described in section 4.3.1.3. The first test (maximum ice climatology check) and the last stage (probability check) are clearly described in section 4.3.1.3, and no further details are provided here. The second test (calculation of probabilities) is more complex and further details are provided here.

The calculation of probabilities for each pixel being covered by ice, cloud or clear-open-water is split into three functions; one for daytime, one for twilight and one for night time conditions. Which function to use is decided by checking the pixel's solar zenith angle (SOZ),

Daytime: 0° <= SOZ <= 70°

Low sun: 70° < SOZ < 90°

Night time: SOZ >= 90°

Daytime probability calculation

The daytime probability calculation uses the naive Bayesian classifier (described in SST-CCI RD.274) with two channel combinations as input. The first channel combination is $RE_{0.9}/RE_{0.6}$. The second depends on which channels are available on the AVHRR instrument. If channel 3A ($RE_{1.6}$) is available, the channel combination $RE_{1.6}/RE_{0.6}$ is used. If $RE_{1.6}$ is not available, the channel combination $BT_{3.7} - BT_{11}$ is used.

The probability of ice, water and cloud is calculated using the functions described in section 4.3.3.1, with these two options of input channels:

$$BayesProb_{\text{Ice}}\left(\frac{RE_{0.9}}{RE_{0.6}}, \frac{RE_{1.6}}{RE_{0.6}}\right)$$

$$BayesProb_{\text{Water}}\left(\frac{RE_{0.9}}{RE_{0.6}}, \frac{RE_{1.6}}{RE_{0.6}}\right)$$

$$BayesProb_{\text{Cloud}}\left(\frac{RE_{0.9}}{RE_{0.6}}, \frac{RE_{1.6}}{RE_{0.6}}\right)$$

or

$$BayesProb_{\text{Ice}}\left(\frac{RE_{0.9}}{RE_{0.6}}, BT_{3.7} - BT_{11}\right)$$

$$BayesProb_{\text{Water}}\left(\frac{RE_{0.9}}{RE_{0.6}}, BT_{3.7} - BT_{11}\right)$$

$$BayesProb_{\text{Cloud}}\left(\frac{RE_{0.9}}{RE_{0.6}}, BT_{3.7} - BT_{11}\right)$$

These Bayesian probability functions depend on the probability density functions for each variable and class. The coefficients for these PDFs are provided in section 4.3.3.3. In these Bayesian functions the normal distribution is used for all the variables and classes. The PDF coefficients are constant for $RE_{0.9}/RE_{0.6}$ and $RE_{1.6}/RE_{0.6}$, and vary linearly as a function of solar zenith angle for $BT_{3.7} - BT_{11}$. The linear functions for the mean (M) and the standard deviation (S) are defined as:

$$M = MA * SOZ + MB$$

$$S = SA * SOZ + SB$$

All the coefficients are provided in Table 4-7.

Low sun probability calculation

For low sun cases (70<SOZ<90), the same Bayesian functions are used as for day. Only normal distributions are used. The only difference is that the PDF coefficients all vary linearly as a function of solar zenith angle. All coefficients are provided in Table 4-8.

Night time probability calculation

For night time cases (SOZ >= 90) the probability of ice, water and cloud depends on a different set of channel combinations:

$$BayesProb_{Ice}\left(dist_{WTP}(BT_{3.7} - BT_{12}, BT_{11} - BT_{12}), LSD(BT_{3.7} - BT_{12})\right)$$

$$BayesProb_{Water}\left(dist_{WTP}(BT_{3.7} - BT_{12}, BT_{11} - BT_{12}), LSD(BT_{3.7} - BT_{12})\right)$$

$$BayesProb_{Cloud}\left(dist_{WTP}(BT_{3.7} - BT_{12}, BT_{11} - BT_{12}), LSD(BT_{3.7} - BT_{12})\right)$$

The distance to water tie-point, $dist_{WTP}$, uses the channel combination $\mathrm{BT}_{3.7} - \mathrm{BT}_{12}$. The water tiepoints in $\mathrm{BT}_{3.7} - \mathrm{BT}_{12}$ depend linearly on $\mathrm{BT}_{11} - \mathrm{BT}_{12}$ in this way:

$$tp_{water} = tp_{WAA} * (BT_{11} - BT_{12}) + tp_{WAB}$$

A normal distribution is used for the $dist_{WTP}$, variable. The local standard deviation, LSD, in the channel combination $\mathrm{BT}_{3.7} - \mathrm{BT}_{12}$ uses normal distribution for water and ice, and log-normal distribution for clouds.

All coefficients are provided in Table 4-9.

4.4.3.3 Look-Up Table Description

This section describes the look-up tables used by the algorithm.

Daytime PDFs

Table 4-19. Coefficients for daytime cloud, water and ice PDFs, mean (M) and standard deviation (S) values. Coefficients A and B are for the linear function which depends on solar zenith angle.

Feature	Satellite	MA Cloud	MB Cloud	SA Cloud	SB Cloud	MA Water	MB Water	SA Water	SB Water	MA Ice	MB Ice	SA Ice	SB Ice
re09/re06	avhrr.12	0.00000	0.85281	0.00000	0.04682	0.00000	0.38893	0.00000	0.07425	0.00000	0.69591	0.00000	0.08343
re09/re06	avhrr.14	0.00000	0.96286	0.00000	0.05668	0.00000	0.46845	0.00000	0.07664	0.00000	0.83564	0.00000	0.10712
re09/re06	avhrr.15	0.00000	0.85934	0.00000	0.04591	0.00000	0.45613	0.00000	0.09711	0.00000	0.71348	0.00000	0.08896
re09/re06	avhrr.16	0.00000	1.00201	0.00000	0.08391	0.00000	0.49379	0.00000	0.05268	0.00000	0.78652	0.00000	0.09502
re09/re06	avhrr.17	0.00000	0.97274	0.00000	0.07145	0.00000	0.49986	0.00000	0.05124	0.00000	0.81967	0.00000	0.10337
re09/re06	avhrr.18	0.00000	0.97274	0.00000	0.07145	0.00000	0.49986	0.00000	0.05124	0.00000	0.81967	0.00000	0.10337
re09/re06	avhrr.19	0.00000	0.97274	0.00000	0.07145	0.00000	0.49986	0.00000	0.05124	0.00000	0.81967	0.00000	0.10337
re09/re06	avhrr.M2	0.00000	0.97274	0.00000	0.07145	0.00000	0.49986	0.00000	0.05124	0.00000	0.81967	0.00000	0.10337
re16/re06	avhrr.17	0.00000	0.72693	0.00000	0.23643	0.00000	0.11614	0.00000	0.06288	0.00000	0.09602	0.00000	0.05110
re16/re06	avhrr.M2	0.00000	0.72313	0.00000	0.23673	0.00000	0.10658	0.00000	0.06581	0.00000	0.08964	0.00000	0.05165
bt37-bt11	avhrr.12	-0.56348	69.35526	0.00000	13.63244	-0.00018	-0.22443	0.00000	0.40911	-0.13988	11.35302	0.00000	1.43857
bt37-bt11	avhrr.14	-0.34541	45.87440	-0.04061	12.95126	-0.00363	-0.00948	-0.00371	0.65188	-0.11360	10.27040	-0.05884	5.66529
bt37-bt11	avhrr.15	-0.25533	48.29366	0.00000	14.09327	-0.00130	0.53671	0.00000	0.58704	-0.09010	8.76945	0.00000	1.31814
bt37-bt11	avhrr.16	-0.38364	60.66684	0.00000	14.71542	0.00880	-0.19203	0.00000	0.56054	-0.09794	8.63588	0.00000	1.17303
bt37-bt11	avhrr.17	-0.31430	44.17989	-0.02694	12.65744	-0.00702	0.28810	-0.00607	0.80616	-0.05909	5.86810	-0.04862	4.85154
bt37-bt11	avhrr.18	-0.31430	44.17989	-0.02694	12.65744	-0.00702	0.28810	-0.00607	0.80616	-0.05909	5.86810	-0.04862	4.85154
bt37-bt11	avhrr.19	-0.31977	44.41623	-0.04062	13.43065	-0.00199	0.20798	-0.00434	0.68304	-0.02195	3.63142	-0.03212	3.76327
bt37-bt11	avhrr.M2	-0.31977	44.41623	-0.04062	13.43065	-0.00199	0.20798	-0.00434	0.68304	-0.02195	3.63142	-0.03212	3.763

Low sun PDFs

Table 4-20. Coefficients for low sun cloud, water and ice PDFs, mean (M) and standard deviation (S) values. Coefficients A and B are for the linear function which depends on solar zenith angle.

Feature	Satellite	MA Cloud	MB Cloud	SA Cloud	SB Cloud	MA Water	MB Water	SA Water	SB Water	MA Ice	MB Ice	SA Ice	SB Ice
re09/re06	avhrr.12	0.00583	0.45108	0.00453	-0.26367	0.00156	0.26167	0.00081	0.00522	0.00085	0.61656	0.00001	0.08067
re09/re06	avhrr.14	0.00249	0.81170	0.00322	-0.16418	0.00680	-0.02092	-0.00151	0.16632	-0.00176	0.96871	-0.00175	0.23960
re09/re06	avhrr.15	0.00742	0.37190	0.00461	-0.26915	-0.00460	0.78057	-0.00037	0.10901	-0.00215	0.93308	-0.00008	0.09755
re09/re06	avhrr.16	0.00352	0.79392	0.00212	-0.06511	0.00366	0.24588	-0.00193	0.18403	0.00316	0.55905	0.00220	-0.06487
re09/re06	avhrr.17	0.00432	0.69152	0.00261	-0.10628	0.00228	0.36877	-0.00128	0.12892	0.00025	0.78506	-0.00024	0.12318
re09/re06	avhrr.18	0.00554	0.61246	0.00259	-0.10782	0.00422	0.20235	-0.00123	0.13233	-0.00114	0.89733	0.00017	0.10009
re09/re06	avhrr.19	0.00641	0.53107	0.00241	-0.09328	0.00460	0.18173	-0.00189	0.17628	-0.00240	1.04805	0.00151	-0.01988
re09/re06	avhrr.M2	0.00441	0.68548	0.00265	-0.10751	0.00372	0.25285	-0.00213	0.19982	0.00117	0.71995	-0.00034	0.13009
re16/re06	avhrr.17	-0.00035	0.74791	0.00001	0.22789	0.00005	0.11209	-0.00111	0.13291	-0.00013	0.11627	-0.00014	0.05621
re16/re06	avhrr.M2	-0.00097	0.77669	-0.00056	0.27837	0.00121	0.02402	-0.00116	0.13967	0.00013	0.09111	-0.00020	0.06397
bt37-bt11	avhrr.12	-1.00387	100.18210	-0.15530	24.50319	0.00534	-0.61087	0.00872	-0.20153	-0.06709	6.25776	-0.00693	1.92355
bt37-bt11	avhrr.14	-0.81486	78.73564	-0.14252	20.08538	0.01219	-1.11710	0.00240	0.22361	-0.09941	9.27680	-0.02231	3.10805
bt37-bt11	avhrr.15	-1.00285	100.62026	-0.17166	26.10963	-0.02880	2.46204	-0.01085	1.34667	-0.11211	10.30992	-0.01966	2.69413
bt37-bt11	avhrr.16	-1.46363	136.26590	-0.32002	37.11670	-0.02121	1.90920	-0.01203	1.40245	-0.07151	6.78563	-0.01865	2.47865
bt37-bt11	avhrr.17	-0.86394	82.65454	-0.25658	28.73197	-0.01483	0.83486	-0.00069	0.42907	-0.09409	8.31815	-0.04490	4.59092
bt37-bt11	avhrr.18	-0.86394	82.65454	-0.25658	28.73197	-0.01483	0.83486	-0.00069	0.42907	-0.09409	8.31815	-0.04490	4.59092
bt37-bt11	avhrr.19	-0.83436	80.43717	-0.20255	24.76542	-0.02043	1.49843	-0.00797	0.93716	-0.10423	9.39069	-0.04826	4.89320
bt37-bt11	avhrr.M2	-0.83436	80.43717	-0.20255	24.76542	-0.02043	1.49843	-0.00797	0.93716	-0.10423	9.39069	-0.04826	4.89320

Night time PDFs

Table 4-21. Coefficients for night time cloud, water and ice PDFs, mean (M) and standard deviation (S) values. The water tie-point coefficients are given in TA Water and TB Water. Empty cells mean that the coefficients are not used. Normal distribution mean and standard deviation coefficients are provided under LSD(bt37-bt12) and log-normal under ln(LSD(bt37-bt12)).

Satellite	M Cloud	S Cloud	M Water	S Water	M Ice	S Ice	TA Water	TB Water
avhrr.12	0.000	2.078	0.000	0.323	0.000	0.968	0.874	0.076
avhrr.14	0.000	2.187	0.000	0.295	0.000	0.884	1.067	-0.040
avhrr.15	0.000	2.094	0.000	0.258	0.000	0.774	0.906	0.037
avhrr.16	0.000	2.061	0.000	0.261	0.000	0.783	0.835	-0.018
avhrr.17	0.300	2.066	0.000	0.183	0.000	0.548	0.703	-0.152
avhrr.18	0.100	2.009	0.000	0.164	0.000	0.492	0.904	-0.433
avhrr.19	0.500	2.103	0.000	0.153	0.000	0.460	0.996	-0.397
avhrr.M2	0.100	2.057	0.000	0.144	0.000	0.433	0.767	-0.307
avhrr.12			0.310	0.118	0.920	0.236		
avhrr.14			0.190	0.074	0.539	0.148		
avhrr.15			0.130	0.054	0.385	0.108		
avhrr.16			0.140	0.054	0.375	0.109		
avhrr.17			0.130	0.056	0.357	0.113		
avhrr.18			0.100	0.056	0.336	0.113		
avhrr.19			0.100	0.055	0.316	0.111		
avhrr.M2			0.100	0.058	0.340	0.116		
avhrr.12	-0.392	0.425						
avhrr.14	-0.622	0.588						
avhrr.15	-0.711	0.688						
avhrr.16	-0.721	0.690						
avhrr.17	-0.767	0.716						
avhrr.18	-0.795	0.752						
avhrr.19	-0.817	0.773						
avhrr.M2	-0.817	0.751						

4.4.3.4 Algorithm Output

The output of the AVHRR cloud and ice mask algorithm is the probability of each pixel being clear-open-water, ice covered and cloud covered. Each of these numbers is non-dimensional, is between 0.0 and 1.0 and together they sum up to 1.0. The three numbers are used to mark the respective pixels as clear-open-water, cloud covered or ice covered.

4.4.4 Assumptions and Limitations

4.4.4.1 Algorithm Performance

During the development and tuning of the high latitude ice and cloud masking algorithm, some assumptions that might influence the algorithm have been made. These assumptions are listed in this section.

For the PDFs that have been developed, it has been assumed that they are Gaussian normal distributions. This is a simplification that holds for a large part of the range of observations for the chosen channel combinations, but not for all. Under very low sun conditions or at very high satellite zenith angles the observed distributions might deviate from Gaussian distributions. Still, in most cases the Gaussian distribution holds and this assumption is a good one.

In some cases, the defined PDFs have shorter overlaps between the classes in one variable than is observed. This sometimes happens in the range of observations where it is very difficult to separate the classes with the variable in question. This might lead to a more certain classification than it should.

It is assumed that the PDFs do not change with satellite zenith angle. The PDFs have been developed using data covering all satellite zenith angles. This will have a small impact on textural features such as local standard deviation (LSD), which is smoother at higher satellite zenith angles.

For this algorithm it is assumed that there is no difference in prior probability between ice, water and cloud.

Under twilight conditions, the ability to separate the different classes decreases with increasing solar zenith angle, mainly for solar zenith angles between 80° and 90°. So the algorithm performance is worse with increasing solar zenith angle during twilight.

Under night time conditions it is very difficult to discriminate between clouds and ice, due to the spectral characteristics of ice and clouds being very similar in the three available AVHRR channels. Therefore the night time algorithm cannot be expected to perform well in separating clouds and ice, but should work reasonably well in separating clear-open-water from clouds or ice.

4.4.4.2 Sensor Performance

Some assumptions have been made concerning the sensor performance during the algorithm development. The assumptions are listed in this section.

It is assumed that the radiometric data are consistently calibrated over time. It is also assumed that the radiometric data do not degrade over time and that the radiometric noise is constant. This is necessary for using PDFs that do not vary with time. The check on the calibration of the radiometric data must be handled elsewhere in the processing chain.

4.4.5 Future Enhancements

A possible enhancement is to introduce different prior probabilities to the three classes: ice, water and cloud. The ice and water prior probabilities could for example depend on a sea ice concentration product.

The future switch to ERA-5 is expected to improve the prior state. The overall impact on cloud detection is unknown, and effort may be required to adapt thresholds and assumptions to maintain a good balance of false alarm rate and hit rate. The prior uncertainty of TCWV will also change (and likely not be known initially). Once these adaptations have bedded down, the new NWP is likely to bring improvement.

5. RETRIEVAL OF SKIN SEA SURFACE TEMPERATURE FROM THERMAL INFRARED SENSORS

5.1 General considerations and setup

5.1.1 Naming conventions for channel combinations

SST retrieval is done using difference channel combinations. For day-time observations, generally 11 and 12 μm channels are used and for night-time, 3.7, 11 and 12 μm. The exception is for AVHRR instruments with no 12 μm channel, for which only night-time retrievals using 3.7 and 11 μm are undertaken.

The SST retrieval and cloud detection steps use a three-character identifier to record which combination of IR and Vis/NIR channels used.

- The first character indicates which view is used, and is either “n” for “nadir” (which applies even to off-nadir angles of single view sensors) or “d” for “dual”, which applies only to ATSRs and, in future, the oblique swath-width for SLSTR.
- The second character indicates which IR channels are used, and is a number ranging between 2 (the classic split window combination) and 4 (the unusual 3.7-11 combination).
- The third character indicates which reflectance channels are used. A two-character identifier is used when only the thermal IR channels have been included.

The full convention is set out in Table 5-1.

Table 5-1: Retrieval naming conventions for channel combinations

First part (view)		Second part (IR)		Third part (Vis/NIR)	
n	Nadir	1	11 μm		Not provided: No reflectance channels
d	Dual	2	11, 12 μm	a	1.6 μm
		3	3.7, 11, 12 μm	b	0.6, 0.8 μm
		4	3.7, 12 μm	c	0.6, 0.8, 1.6 μm

The use of Vis/NIR reflectance channels is expected to have little or no effect on the SST retrieval in most cases as these channels are not sensitive to SST. However, they can affect add some information on the atmospheric water vapour present. Or if the 3.7 μm channel is required during the day, then Vis/NIR could help determine the level of reflected solar radiation in the SWIR. These possibilities are not exploited in Phase II because the SST benefit is understood to be modest, while adding those channels could entail some risk. Thus, during CCI Phase 2 the Vis/NIR channels are used for cloud detection only, not the SST retrieval, and the ability to use them has been implemented for internal consistency checks, future work on daytime AVHRR/1 retrievals, and future work on extended retrievals. Therefore, the final letter code at present indicates what reflectance channels are used for cloud detection, but all retrievals are thermal-only.

Thus, in v2, the retrieval combinations used are as shown in Table 5-2.

Table 5-2: Channel combinations used in v2 for SST retrieval.

Sensor	Day	Night	Twilight
ATSR	d2a	d3	d2
AVHRR/2	n2b	n3	n2
AVHRR/3	n2b	n3	n2

5.2 Optimal estimator for AVHRRs

5.2.1 General formulation for reduced-state vector optimal estimation for SST

Optimal estimation (OE) was first discussed in reference to SST retrieval in Merchant et al., 2008 [RD.221] and extended with a smooth-atmosphere assumption in Merchant et al., 2012 [RD.295].

A variant of smooth-atmosphere OE is used for AVHRR SST retrieval in this reprocessing.

In the OE methodology, *a priori* expectations, $\boldsymbol{x}_a$, about the state of the atmosphere and ocean are used as inputs to a forward model, $\boldsymbol{F}$, to simulate prior observations, $\boldsymbol{y}_a$, which represent the expected brightness temperatures (BT), i.e. $\boldsymbol{y}_a = \boldsymbol{F}(\boldsymbol{x}_a)$. The state variables $\boldsymbol{x}_a$ are from numerical weather prediction (NWP) data and the forward model $\boldsymbol{F}$ is the radiative transfer model RTTOV11.3. The sea surface emissivity is taken from the ATSR Reprocessing for Climate (ARC) emissivity model and a reflectivity correction based on the method of Watts et al. [RD.297] has been applied. The sensitivity of the simulated BTs to variations in the state variables, $\boldsymbol{K}$, is defined using the tangent linears to the forward model. These sensitivities are combined with the difference between the observed and simulated BTs ($\boldsymbol{y}_o - \boldsymbol{F}(\boldsymbol{x}_a)$), to optimally modify the prior estimate of the state, which includes the SST. The retrieved state variables, $\hat{\boldsymbol{x}}$, are estimated using:

$$\hat{\boldsymbol{x}} = \boldsymbol{x}_a + \mathrm{G}\left(\boldsymbol{y}_o - \mathrm{F}(\boldsymbol{x}_a)\right) = \boldsymbol{x}_a + (\boldsymbol{K}^T\boldsymbol{S}_\varepsilon^{-1}\boldsymbol{K} + \boldsymbol{S}_a^{-1})^{-1}\boldsymbol{K}^T\boldsymbol{S}_\varepsilon^{-1}(\boldsymbol{y}_o + \mathrm{F}(\boldsymbol{x}_a)) \quad \textbf{(5-1)}$$

G is the gain matrix that operates on the observed minus simulated BT difference (this is described in detail in RD.307). $\boldsymbol{S}_\varepsilon$ is the error covariance of the model and satellite observations of the BTs. These are a combination of the radiometric noise in the observations and estimated uncertainty of the forward model. It is assumed that the radiometric noise and the forward model errors are uncorrelated between channels. The impact of this assumption is discussed in RD.221. $\boldsymbol{S}_a$ is the error covariance matrix for the prior state variables. Using 3.1, the retrieved state is optimal in the sense that it will give an unbiased, minimum standard deviation estimate of the state if (i) the prior information are unbiased and (ii) the forward model is unbiased [RD.221].

It was shown in RD.221 that a reduced state vector based on the leading modes of variability can be used in the optimal estimation of the state. The SST and TCWV variability are associated with the first two dominant modes of variability in the BTs, so these two state variables are used to define the reduced state vector ($\boldsymbol{z}(\boldsymbol{x}) = \begin{bmatrix} x \\ w \end{bmatrix}$), where *x* represents the SST and *w* represents the TCWV. (Strictly speaking, windspeed, marine AOD and stratospheric AOD also appear in the state vector, but these play a minor role and for the present purpose can be neglected.) It should be noted that the full state vector

$\boldsymbol{x}_a$ is still used to calculate the simulated BTs. Use of the reduced state vector in the OE reduces the size of the $\boldsymbol{S}_a$ error covariance matrix to 2×2. In this case it can be assumed that the errors in the state variables are uncorrelated.

Merchant et al. [RD.295] demonstrate that the uncertainty in the OE retrieved SST is reduced if the prior TCWV error variance is constructed so as to account for the limitations in the NWP fields used to define the prior state. The prior TCWV error variance used in generating the SST CCI data is detailed in Table 5-3. There is a trade-off between the SST error variance (the dispersion of uncertainty in the retrieval) and both the SST bias and SST sensitivity [RD.295].

The OE formulation operates on a reduced state vector $\mathbf{z}=\begin{bmatrix} x \\ \bar{x} \\ \bar{w} \end{bmatrix}$, which includes only SST (x), the average SST of the surrounding *n* clear-sky pixels and TCWV ($\bar{w}$). For SST CCI purposes, only the first retrieved variables are of interest and used in products. The assumption is made that the same water vapour loading applies to the target pixel and the surrounding clear-sky pixels: this reduces the retrieved SST noise somewhat (atmospheric correction smoothing: RD.396). The formulations used in the reduced state-vector OE for AVHRRs are listed in Table 5-3.

The optimal estimator formulated in this way is a *maximum a posteriori* solution, although in order to avoid low SST sensitivity (i.e., heavy dependence on the prior) the assumed error covariance on prior SST is larger than is realistic. Heavy dependence on the prior would be inappropriate for a climate data record, particularly since the prior comes from a number of sources over time (see next section). Inflated SST error variance makes the solution approximately equal to a *maximum likelihood* solution (which is the limit of a MAP solution in the limit of infinite assumed prior SST error variance) with respect to SST. At the same time, a realistic error variance is assumed for water vapour, retaining the benefit of some of the regularisation of the inversion that is a feature of the MAP solution. We refer to the OE formulation as “ML-like”, which refers to its properties as far as SST is concerned.

Table 5-3. Parameters in the SST CCI optimal estimator for AVHRRs

Aspect of optimal estimator	Assumption/configuration
Reduced state vector	$\mathbf{z}=\begin{bmatrix} x \\ \bar{x} \\ \bar{w} \end{bmatrix}$
Prior SST, x_a	'ERA Interim' skin sea surface temperature, adjusted for diurnal cycle
Error SD in prior, e_{xa}	Varies between 0.6 and 1.5 K, geographically
Prior full state vector, x_a	'ERA Interim' surface pressure plus atmospheric profiles of temperature and humidity on ECMWF model pressure levels
Prior TCWV, w_a	The vertical integral of the water vapour absolute humidity from the full state vector x_a
Error in prior TCWV, e_{wa}	$w(ae^{-bw}+c)$ [w in kg m^{-2}] a = 0.42; b = 0.05; c = 0.042
Prior error covariance matrix,	$\begin{bmatrix} e_{xa}^{\ 2} & & \\ & e_{xa}^{\ 2} & \\ & & e_{wa}^{\ 2} \end{bmatrix}$
Forward model for simulated BTs	RTTOV11
Forward model error, ε_{RT}	e_{RT} sec(θ), where θ is the satellite zenith angle and e_{RT} = 0.15 K for 3.7 μm; 0.16 for 11 μm; 0.17 for 12 μm
Pixel-level BT noise equivalent differential temperature / K	0.06 K at 300 K Scaled by Planck function at other temperatures (i.e., assumes constant radiance error standard deviation).
Prior BT covariance matrix. [1]	$\begin{bmatrix} \varepsilon_{3.7}^{\ 2}+\varepsilon_{RT}^{\ 2} & & & & & \\ & \varepsilon_{11}^{\ 2}+\varepsilon_{RT}^{\ 2} & & & & \\ & & \frac{1}{n}\varepsilon_{12}^{\ 2}+\varepsilon_{RT}^{\ 2} & & & \\ & & & \frac{1}{n}\varepsilon_{3.7}^{\ 2}+\varepsilon_{RT}^{\ 2} & & \\ & & & & \frac{1}{n}\varepsilon_{11}^{\ 2}+\varepsilon_{RT}^{\ 2} & \\ & & & & & \varepsilon_{12}^{\ 2}+\varepsilon_{RT}^{\ 2} \end{bmatrix}$
Tangent linear matrix [2], K	$\begin{bmatrix} \frac{\partial y_{3.7}}{\partial x} & 0 & \frac{\partial y_{3.7}}{\partial \bar{w}} \\ \frac{\partial y_{11}}{\partial x} & 0 & \frac{\partial y_{11}}{\partial \bar{w}} \\ \frac{\partial y_{12}}{\partial x} & 0 & \frac{\partial y_{12}}{\partial \bar{w}} \\ 0 & \frac{\partial \bar{y}_{3.7}}{\partial \bar{x}} & \frac{\partial \bar{y}_{3.7}}{\partial \bar{w}} \\ 0 & \frac{\partial \bar{y}_{11}}{\partial \bar{x}} & \frac{\partial \bar{y}_{11}}{\partial \bar{x}} \\ 0 & \frac{\partial \bar{y}_{12}}{\partial \bar{x}} & \frac{\partial \bar{y}_{12}}{\partial \bar{x}} \end{bmatrix}$

[1] Here ε_x indicates the channel at wavelength x μm. When using fewer channels, the corresponding rows and columns are omitted. $\boldsymbol{\varepsilon}_{RT}$ depends on channel wavelength and satellite zenith angle.

[2] y_x indicates the channel at wavelength x μm. The partial derivatives with respect to w require an assumption about how water vapour changes at different altitudes are related. The assumption made is that the fractional change in absolute humidity is the same for all altitudes. When a particular channel/view is not included in the retrieval, the corresponding column of K is omitted.

The prior SST The SST supplied (see Table 5-4) with ERA-interim NWP is a daily value, typically a “foundation” or pre-dawn buoy equivalent SST. As such it is a suitable prior at night but can underestimate the true SST during the day, particularly in conditions of low wind speed as shown in (left). In order to adjust the prior to the actual observation time we use the Morak-Bozzo empirical DV model, this improves the agreement between NWP SST and in situ drifters as shown in Figure 5-1(right). The empirical model under-corrects for very low wind speeds (< 3 ms^{-1}), but it is a significant improvement on the uncorrected prior.

For Bayesian Cloud detection this reduces chance that strong diurnal warming events will incorrectly screened as cloud (as they are “too warm”). For the OE SST retrieval the adjustment will have a small impact on the OE retrieval which is proportional to 1 minus the SST sensitivity, a factor that, using the “ML-like” formulation, is generally less than 5%.

Table 5-4: Sources of SST and sea-ice concentration used in ERA-interim

ERA-Interim dates	SST and SIC product used
Start – October 1981	HADISST
November 1981	HADISST + NCEP 2D-Var
December 1981 – June 2001	NCEP 2D-Var sea surface temperature (NCEP 2D-Var)
July 2001 – December 2001	NOAA Optimum Interpolation Sea Surface Temperature v2 (NCEP OISST v2)
January 2002 – January 2009	NCEP Real-Time Global sea surface temperature (NCEP RTG)
February 2009 – onwards	Operational Sea Surface Temperature and Sea-Ice Analysis (OSTIA)

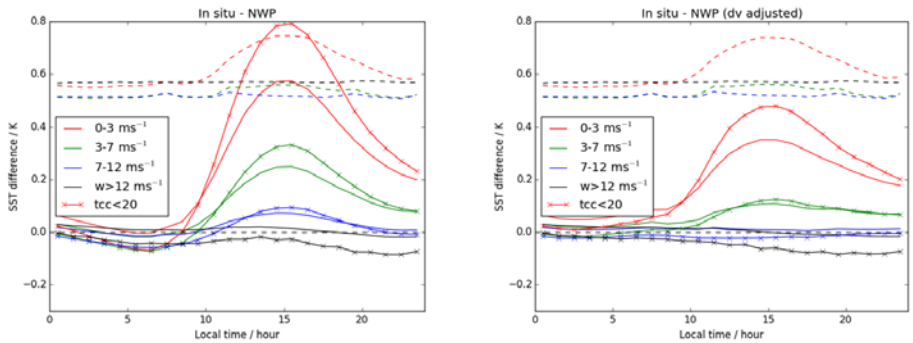

Figure 5-1: Left: (solid, no crosses) mean difference between in situ drifter SST and ERA-interim SST in SST CCI match-up data’; (solid with crosses) as solid lines, but for low total cloud cover (tcc < 20%); (dashed lines) standard deviation of differences. Right: same as left, but after applying Morak-Bozzo empirical adjustment (RD.396).

5.2.2 Aerosol capabilities in forward model for OE

The version of RTTOV (v11.3) now available and used in v2 has capability to represent aerosol in thermal calculations, which is an upgrade relative to the previous ATBD.

5.2.2.1 Marine Aerosol

Marine aerosol is now included in the RTTOV forward model simulations (affects both Bayesian cloud detection, and Optimal Estimation of SST (used for AVHRR instruments).

The marine aerosol profile uses the OPAC (Hess et al. 1998) “Maritime clean” components with the Koepke et al. 1997 wind speed dependence:

Water soluble: $N_0 = 1500$

Sea salt (acc.): $N_0 = \exp(0.18u + 1.4)$

Sea salt (coa.): $N_0 = \exp(0.23u - 7.8)$

The marine aerosol layer is assumed to be 2 km thick with a 1 km height scaling. Number density is given by:

$$N(z) = N_0 exp\left(-\frac{z}{h_s}\right)$$

Uncertainty in the aerosol column is taken as 10%

5.2.2.2 Stratospheric Aerosol

Stratospheric sulphate aerosol is modelled using the OPAC sulphate component (75% H_2SO_4) in a uniform layer between 20 and 24 km altitude. The OPAC sulphate component uses a particle size distribution appropriate for background conditions $r_{\text{mod N}} = 0.0695$μm. While $r_{\text{mod N}}$ did increase by an order of magnitude immediately after the eruption of Mount Pinatubo, this primarily affected the total optical depth and did not affect the relative impacts at different thermal wavelengths (Embury et al. 2012).

To check the RTTOV aerosol calculations we derived ARC-style aerosol robustness mode from the RTTOV simulations and compared it against the Pinatubo aerosol mode calculated in the ARC project. The two modes are compared in Figure 5-2 the two calculations show slight differences in the relative impacts when all six ATSR channels are considered (three wavelengths and two views) – this is primarily due to differences in the 3.7 μm channel, when the comparison is restricted to just the 11 and 12 μm channels the ARC and RTTOV calculations produce virtually identical modes. The better agreement at longer wavelengths can be explained by the use of a fast forward model (RTTOV) which has to use a very crude approximation for scattering, while the ARC aerosol calculations used a much slower, but more accurate model (DISORT).

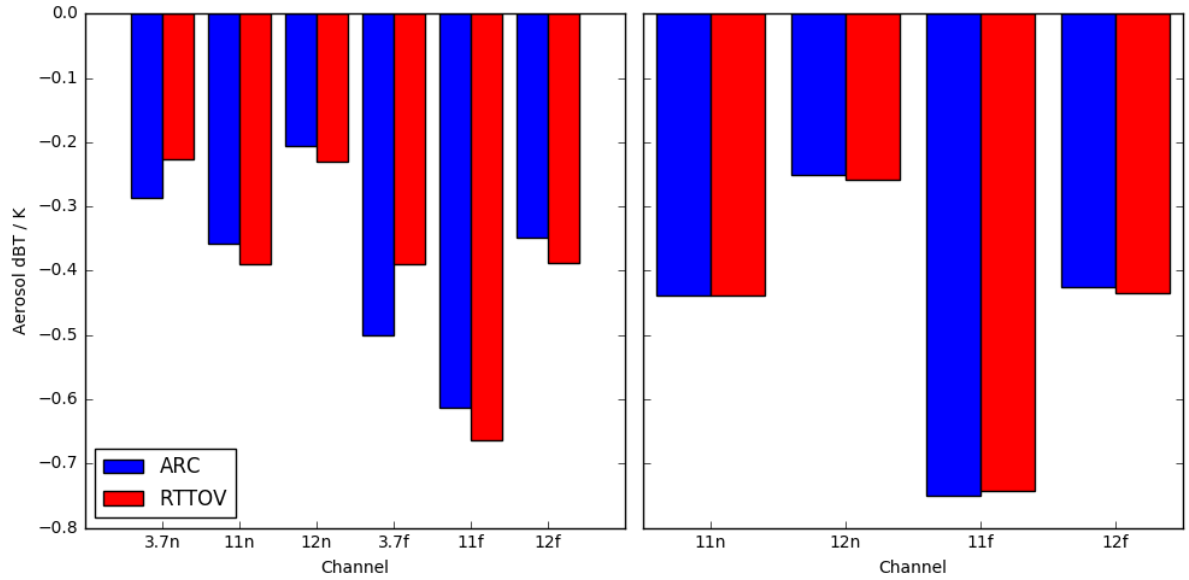

Figure 5-2: Stratospheric aerosol delta-BTs calculated for the ARC project and fast calculations using RTTOV. Left using all ATSR channels; right using only 11 and 12 μm

The sulphate aerosol number density in the stratospheric layer is taken from a lookup tables for the two main eruptions (Mount Pinatubo and El Chichón), as describe in 4.1.5.2.

5.3 Estimator for ATSR SSTs

For the ATSR series, retrieval coefficients are used in this reprocessing. These are based on the ARC retrieval coefficients, where the full description of ARC SST retrieval process is given in RD.184, RD.185 and RD.186. However, the coefficient definition and harmonisation process has been repeated in its entirety to account for more up-to-date radiative transfer and recommendations of an Anomaly Review Board (ARB) recommendation on the calibration of the AATSR 12 μm channel (RD.397). The following sections present key points on the calculation of the retrieval coefficients.

5.3.1 Basis in radiative transfer

With improvements in the spectroscopic data describing water vapour continuum absorption, the coefficients used for SST retrieval are routinely calculated using radiative transfer modelling of TOA radiances. Compared with empirical regression methods, this approach has the advantage that the retrieval coefficients are independent of in situ observations which is beneficial for climate research. Figure 5-2 provides a schematic illustration of the process used to generate SST retrieval coefficients using simulated data. The calculation of the retrieval coefficients requires the simulation of the clear-sky TOA radiances that would be measured by infrared sensors. The forward model used to simulate the TOA clear-sky radiance values consists of a radiative transfer model (RTM), spectroscopic data, sensor spectral response functions, and a representative set of states describing the atmosphere and sea surface on which to perform the simulations. The simulated TOA radiance values are compared with observed radiance for clear-sky conditions to determine uncertainties and bias. The simulated TOA radiance values and the corresponding state SSTs are used to calculate the SST retrieval coefficients. The SST retrieval is then applied to the observed TOA radiance values and the retrieved SSTs are validated against in situ observations of the SST.

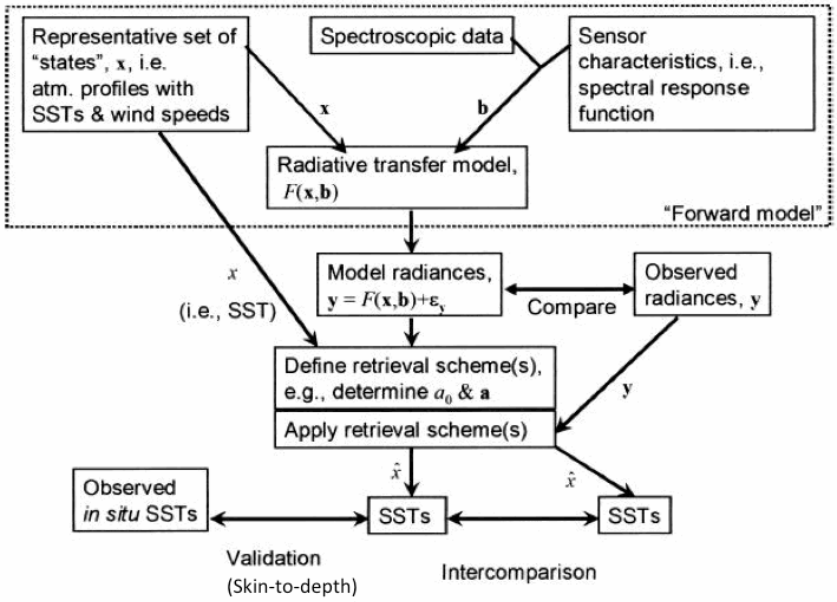

Figure 5-3. Schematic of the process for defining and validating coefficients for sea surface temperature retrieval using radiative transfer modelling [RD.253].

5.3.1.1 Clear-sky radiative transfer model

To achieve the required accuracy in the TOA radiance values, - the Line-By-Line Radiative Transfer Model (LBLRTM; http://rtweb.aer.com/) was used. The effects of tropospheric and stratospheric aerosols and gases interacting with radiation must be simulated. For the ARC reprocessing, the scattering by aerosol particles with radii comparable to the wavelengths of thermal infrared radiation measured by the sensors, was calculated using the DISORT scattering model [RD.300]. This was applied to channel integrated clear-sky transmittances derived from the line-by-line LBLRTM calculations.

LBLRTM was used as it meets the following criteria [RD.301] for simulation of brightness temperatures suitable for determining SST coefficients:

- It is capable of simulating radiances at a spectral resolution of 0.01 cm^{-1} or better.
- It includes CO_2 line mixing.
- It is capable of modelling continuum features for water vapour and nitrogen.
- It can calculate radiance with the assumption that the Planck function varies linearly with altitude and that optical depth varies linearly with path within each layer.
- It can enable linear interpolation for profiles of absorber quantities.
- Voigt line shapes are used for all molecules as default (Lorentz and Doppler line shapes can be selected individually).
- It includes all trace gases that have an impact of >0.001 K on TOA BTs, for any channel e.g. H_2O, CO_2, O_3, N_2O, CH_4, NH_3, HNO_3, OCS, H_2CO, N_2, C_2H_6, F11, F12, F22, F113, F114, CCl_4, HNO_4.
- IT uses the HITRAN spectroscopic database.

5.3.1.2 Spectral Emissivity Model

The spectral emissivity model described in RD.186 was adopted for the calculation of the ARC coefficients. The emissivity model uses an isotropic wave facet model to include the wavelength dependence on the refractive index of seawater, temperature, wind roughening of the sea surface and incident and emission angles of radiation relative to the ocean surface.

We found the salinity effect on refractive index to be negligible, so this factor is not included in this model. The model results have been tabulated and are available in RD.320. The emissivity data are presented as a function of wavenumber (600-3350 cm^{-1}), view angle (0-85°), temperature (270-310 K), and wind speed (0-25 m s^{-1} at 12.5m).

5.3.1.3 Atmospheric Meteorological Profiles for Radiative Transfer

A representative distribution of simulated TOA BTs is required to calculate the SST retrieval coefficients. This requires a representative distribution of atmospheric states – i.e. profiles of atmospheric temperature, water vapour and associated surface variables. There are two distinct sources of suitable data: (i) measurements in the form of radiosondes, and (ii) simulated data from numerical weather prediction (NWP) models. For the calculation of the ARC retrieval coefficients [RD.185], NWP data from the ECMWF 40-year reanalysis (ERA-40) were used as these give a more representative global sample compared with radiosonde data. These were assessed to span all the necessary variability, which is the key requirement for this profile set; the potential biases known to be present in such a dataset were found not to be critical [RD.185]. ERA-40 consists of 6-hourly surface and profile data (on 60 pressure levels) covering the years 1957 to 2001, on a 2.5° horizontal grid. Due to resource restrictions such a large data set could not be processed, so basic temporal sampling was applied leaving a subset of data covering all times of day for all seasons. These were extracted from the "60L-SD" data set [RD.302], used as the starting point for the ARC project database. This subset of the data was then filtered to remove:

- All land or mixed land/ocean profiles
- All profiles with >95% sea ice
- All profiles outside RTTOV's validity range for water vapour
- All profiles with >95% relative humidity for any layer (such profiles are indicative of near-total cloud cover conditions, not representative of clear skies under which SST retrievals are possible).

5.3.1.4 Trace gas profiles

Trace gases that affect simulated BTs by 1 mK or more were included in the simulations for ARC. Some gases have geographic or temporal variations that have a significant impact on BTs, whereas for less influential/variable trace gases, global profiles may be used. The trace gases used in ARC along with whether annual or latitudinal variations were represented are listed in Table 5-3. All the trace gases have secular trends that were accounted for. Details of the trends, annual and latitudinal variations used are given in RD.301 and RD.186.

Table 5-5. Trace gases included in simulations for coefficients and the aspects of variability accounted for in each case.

Gas	Long Term Trend	Annual Cycle	Latitudinal Variation
NH_4	Y	N	N
HNO_3	Y	Y	Y
N_2O	Y	N	Y
CH_4	Y	N	Y
CFC 11	Y	N	Y
CFC 12	Y	N	Y
CO_2	Y	N	N

5.3.1.5 Aerosol simulations

Tropospheric aerosol number density was assumed to follow an exponential height distribution

$$N(z) = N(0)e^{(-z/h)} \quad \textbf{(5-2)}$$

where $N(0)$ is the aerosol concentration at the surface, h is the scale height in kilometres, and z is the altitude. The OPAC dataset contains a set of aerosol profiles of this form. These aerosol profiles are associated with a range of different geographical locations, and differ in terms of the components present and surface concentrations. The Global Aerosol Data Set (GADS) was used alongside the optical property dataset (OPAC) to give a good representation of the tropospheric aerosol profiles.

Major volcanic eruptions (Mt. Pinatubo and Mt. Hudson, both in 1991) significantly changed the stratospheric aerosol throughout the ATSR-1 mission. Stratospheric aerosols produced by major volcanic eruptions need to be simulated in order to ensure aerosol robustness of coefficients. In situ measurements of stratospheric aerosol size distribution are available for a 30 year period at Laramie, Wyoming [RD.304]. These data provided vertical profiles of both the number density and size distribution fitted using a bimodal lognormal function. The primary mode represents the more numerous small particles, the secondary mode the larger particles which have a greater impact on infra-red scattering. These data were used to define a background number density and the change associated with volcanic aerosols. The primary mode showed negligible variation with time so a single number distribution was derived from the data using equation 3.6, where the coefficients based on height are:

z = 12 – 24 km,	$N(0)$ = 2146.9 cm^{-3},	h = 2.85921 km
z = 24 – 32 km,	$N(z)$ = 4 cm^{-3}	
z < 12km or > 32 km,	$N(z)$ = 0 cm^{-3}.	

The particle radius was fixed at 0.025 μm.

The secondary mode was found to vary from year to year, however it was sufficient to define a single number density profile which was scaled by year for the background.

z = 12 – 24 km,	$N(z)$ = 0.173 cm^{-3}	
z = 24 – 32 km,	$N(0)$ = 4.04370×10^{6} cm^{-3},	h = 1.41467 km
z < 12km or > 32 km,	$N(z)$ = 0 cm^{-3}.	

The scale factors for the stratospheric number density profile by year are [RD.186]:

Table 5-6: Scale factors for the stratospheric aerosol number density profile as a function of year.

Year	1991	1992	1993	1994	1995	1996	1997+
Scale	1.0	20.0	9.0	4.0	1.5	0.5	0.3

The particle radius for the secondary mode was constant at 0.35 μm for the background level, but during the years affected by volcanic aerosol (1992-1994) the lower level aerosol distribution increased linearly with decreasing height. During 1992/1993 the particle size increased from 0.35 μm at 24 km to 0.75 μm at 12 km, while during 1994 the size increased from 0.35 μm at 24 km to 0.55 μm at 12 km.

5.3.2 Calculation of retrieval coefficients

The ARC SST estimate, $\hat{x}$, is formed from a weighted combination of BTs.

$$\hat{x} = a_0 + \boldsymbol{a}^T \boldsymbol{y} \qquad \textbf{(5-3)}$$

Here a_0 is the offset coefficient, and $\boldsymbol{a}^T = [a_1, \ldots, a_n]$ is a vector of n weighting coefficients for the n BTs in the observation vector ($\boldsymbol{y}$). These observations may consist of infrared observations at different wavelengths and/or view angles. The superscript ^{T} indicates the transpose of the vector.

The offset and weighting coefficients are found using least squares minimization techniques. These minimize the mean square difference between the "true" SST input to the RTM and the "retrieved" SST, for the population of atmospheric and surface states and associated RTM BTs outlined in section 5.2.1. The weights and offset term are given by the formulas:

$$\boldsymbol{a} = \boldsymbol{S}'^{-1}_{yy} \left[\boldsymbol{S}_{xy} - \boldsymbol{K}\left(\boldsymbol{K}^T \boldsymbol{S}'^{-1}_{yy} \boldsymbol{K}\right)^{-1} \left(\boldsymbol{K}^T \boldsymbol{S}'^{-1}_{yy} \boldsymbol{s}_{xy}\right) \right] \qquad \textbf{(5-4)}$$

$$a_0 = \bar{x} - \boldsymbol{a}^T \bar{\boldsymbol{y}} \qquad \textbf{(5-5)}$$

where

$$\boldsymbol{S}'^{-1}_{yy} = \boldsymbol{S}_{yy} + \boldsymbol{S}_{\varepsilon}$$

x is the "true" SST associated with a given set of simulated BTs ($\boldsymbol{y}$)

$\boldsymbol{S}_{yy}$ is the covariance matrix of observations

$\boldsymbol{S}_{\varepsilon}$ is the covariance matrix for the noise equivalent differential temperature [RD.321]

$\boldsymbol{s}_{xy}$ is the covariance vector of SST and observations.

$\boldsymbol{K}$ is a matrix containing the impacts on BTs of the presence of stratospheric aerosol, $\partial y / \partial \sigma$, where σ is the stratospheric aerosol optical depth. The over-bars indicate mean values are used. The covariance matrix of the observations $\boldsymbol{s}_{yy}$ is defined as:

$$\boldsymbol{S}_{yy} = \overline{\boldsymbol{y}\boldsymbol{y}^T} - \bar{\boldsymbol{y}}\bar{\boldsymbol{y}}^T \qquad \textbf{(5-6)}$$

and the covariance vector of SST and the observations, $\boldsymbol{s}_{xy}$, is given by:

$$\boldsymbol{s}_{xy} = \overline{x\boldsymbol{y}^T} - \overline{x}\,\overline{\boldsymbol{y}}^T \quad \textbf{(5-7)}$$

Use of the $\boldsymbol{K}$ matrix to represent the effects of aerosol ensures the retrieval coefficients are robust to the presence of stratospheric aerosol since this formulation forces the coefficients to be orthogonal to the effects of the aerosols.

The coefficients are calculated at predefined values of the following parameters:

- satellite zenith angle in the nadir view
- satellite zenith angle in the forward view
- prior TCWV
- instrument detector temperature
- year

The coefficients applied for a given SST retrieval are found by interpolating the tabulated values based on these parameters. Bilinear interpolation is used to interpolate the satellite zenith angles, and linear interpolation used for the other parameters.

5.3.3 Atmospheric correction smoothing for L2P

The discussion to this point considers the retrieval of SST for a single clear-sky pixel in isolation. In fact, since the water vapour of the atmosphere varies smoothly on few-km scales, this fact can be used to reduce noise in full resolution SST products, through "atmospheric correction smoothing". Hereafter, the term "atmospheric correction smoothing" will be referred to simply as "smoothing" for readability. Always bear in mind that it is not the aim to smooth the SST which is being retrieved. Instead, the aim is to minimize smoothing of SST, while yet exploiting the longer spatial scales of atmospheric variability in order to reduce SST noise.

Let x represent SST, and let the brightness temperatures (BTs) from which SST is to be estimated be listed in a column vector $\mathbf{y}$, such that $\mathbf{y}^{\mathrm{T}} = [y_1 \quad y_2 \quad \cdots]$, where y_i is the BT of the i^{th} thermal channel being used for retrieval. "Atmospheric correction" is the difference between the SST and the top of atmosphere brightness temperature. Since we have more than one channel, a generalised definition of multi-channel atmospheric correction is

$$\boldsymbol{\delta} = \boldsymbol{x} - \mathbf{b}^{\mathrm{T}}\mathbf{y} \;\; ; \;\; \boldsymbol{b_i} > 0 \; for \; all \; \boldsymbol{i} \quad \textbf{(5-8)}$$

The fundamental smoothing assumption is that we have two independent estimates of the true atmospheric correction appropriate to a particular pixel in the thermal image. The first estimate comes from evaluating the atmospheric correction for the target pixel (that for which SST is being retrieved). The second estimate comes from surrounding clear-sky pixels from a box centred on the target pixel. The SSTs for these surrounding pixels may vary, but the assumption is that the atmospheric correction is essentially the same.

Since the coefficient-based estimate of SST is $\hat{x} = a_0 + \mathbf{a}^{\mathrm{T}}\mathbf{y}$, the estimated atmospheric correction for the target pixel is

$$\widehat{\boldsymbol{\delta}} = \hat{\boldsymbol{x}} - \mathbf{b}^{\mathrm{T}}\mathbf{y} = \boldsymbol{a_0} + (\mathbf{a} - \mathbf{b})^{\mathrm{T}}\mathbf{y} \quad \textbf{(5-9)}$$

If we form an average of the BTs of the clear-sky pixels surrounding the target pixel, $\bar{\mathbf{y}}$, then the box-mean estimate of clear-sky atmospheric correction (excluding the target pixel) is, $\bar{\delta} = \overline{a_0} + (\bar{\mathbf{a}} - \mathbf{b})^{\mathrm{T}}\bar{\mathbf{y}}$, where an overbar indicates an average over surround clear-sky pixels. If coefficients vary with satellite viewing geometry, the retrieval coefficients for surrounding pixels may differ from the target pixel, but over a reasonable box size, this will be small; therefore we make the good approximations that $\bar{\mathbf{a}} = \mathbf{a}$ and $\overline{a_0} = a_0$ hereafter.

Combining the target and box estimates of atmospheric correction, we can make a single best estimate. Assuming independence of radiometric noise between pixels, the random errors in $\hat{\delta}$ and $\bar{\delta}$ are uncorrelated. We can also assume that the noise-related uncertainty is constant for all the pixels in the box: this is justifiable for a stable instrument observing the relatively narrow range of scene BT across the box. The noise in atmospheric correction therefore scales as the square root of the number of pixels contributing to each estimate. This number is 1 for the target pixel. Let the number of clear-sky box pixels be *N*. According to the standard result for combining estimates with independent, normally distributed errors, the best estimate for the target pixel atmospheric correction is

$$\tilde{\boldsymbol{\delta}} = \frac{\mathbf{1}}{\mathbf{1}+\boldsymbol{N}}\left(\boldsymbol{N}\bar{\boldsymbol{\delta}} + \hat{\boldsymbol{\delta}}\right) \qquad \textbf{(5-10)}$$

i.e., is a weighted average, the weights being in proportion to the inverse of the error variance. This is identical to the estimate of atmospheric correction that would be obtained by evaluating it as the mean of all the clear-sky pixels in the box including the target pixel, as one would expect. However, separating the target and surrounding pixels in this way will make the relationship between non-smoothed and smoothed estimates of SST explicit, as will be shown below.

Let the SST estimate for the target pixel after atmospheric correction smoothing be $\tilde{x}$. The objective of the smoothing is that this SST will be less noisy than the single pixel retrieval, $\hat{x}$. We can derive $\tilde{x}$ by imposing on the smoothed SST the requirement that its atmospheric correction be $\tilde{\delta}$ rather than $\hat{\delta}$. This implies, combining the definition of atmospheric correction in Equation and Equation (5-12).

$$\tilde{\boldsymbol{x}} - \mathbf{b}^{\mathrm{T}}\mathbf{y} = \frac{\mathbf{1}}{\mathbf{1}+\boldsymbol{N}}\left(\boldsymbol{N}\bar{\boldsymbol{\delta}} + \hat{\boldsymbol{\delta}}\right) = \frac{\boldsymbol{N}}{\mathbf{1}+\boldsymbol{N}}\left(\boldsymbol{a_0} + (\mathbf{a}-\mathbf{b})^{\mathrm{T}}\bar{\mathbf{y}}\right) + \frac{\mathbf{1}}{\mathbf{1}+\boldsymbol{N}}\left(\boldsymbol{a_0} + (\mathbf{a}-\mathbf{b})^{\mathrm{T}}\mathbf{y}\right) \qquad \textbf{(5-11)}$$

Re-arranging this to write the smoothed SST estimate as a single-pixel retrieval plus an adjustment gives

$$\tilde{\boldsymbol{x}} = \boldsymbol{a_0} + \mathbf{a}^{\mathrm{T}}\mathbf{y} - \frac{\boldsymbol{N}}{\mathbf{1}+\boldsymbol{N}}(\mathbf{a}-\mathbf{b})^{\mathrm{T}}(\mathbf{y}-\bar{\mathbf{y}}) = \hat{\boldsymbol{x}} - \frac{\boldsymbol{N}}{\mathbf{1}+\boldsymbol{N}}(\mathbf{a}-\mathbf{b})^{\mathrm{T}}(\mathbf{y}-\bar{\mathbf{y}}) \qquad \textbf{(5-12)}$$

The right hand side comprises the single-pixel retrieval for the target pixel plus a correction term. This correction term is proportional to $(\mathbf{a}-\mathbf{b})^{\mathrm{T}}(\mathbf{y}-\bar{\mathbf{y}})$, which equals the difference in estimated atmospheric correction between the target and surrounding pixels, $\hat{\delta} - \bar{\delta}$. Were $\bar{\delta}$ an infinitely precise estimate of atmospheric correction, then this difference

would exactly equal the noise error in the single-pixel retrieval, and therefore subtracting this difference would correct the noise error in $\hat{x}$. This is represented by the limit $N \to \infty$ in Equation (5-14). However, it is wrong to infer that this implies that the box should be made as large as possible, since too large a box would lead to violation of the conditions for validity of smoothing discussed earlier. Instead, *N* is finite, and varies between 0 (no pixels other than the target pixel is clear in box) and an upper limit determined by the box size. The scaling in Equation (5-14). is always <1, and down-weights the correction term according to the number of surrounding pixels: when *N* is smaller, the additional information on atmospheric correction from the surrounding pixels is less precise, and therefore the $\hat{\delta} - \bar{\delta}$ correction estimate receives less weight in determining $\tilde{x}$. Thus, a generalised form of atmospheric correction smoothing has been derived that has clear physical and statistical justification.

Noting that

$$\frac{N}{1+N}(\mathbf{y} - \bar{\mathbf{y}}) = \left(\frac{N}{1+N}\mathbf{y} - \frac{N}{1+N}\bar{\mathbf{y}} + \frac{1}{1+N}\mathbf{y} - \frac{1}{1+N}\mathbf{y}\right) = (\mathbf{y} - \langle \mathbf{y} \rangle) \qquad \textbf{(5-13)}$$

where $\langle \mathbf{y} \rangle$ is the mean observation vector across all clear-sky pixels in the box, we can rewrite Equation (5-15) as

$$\tilde{x} = a_0 + \mathbf{a}^{\mathrm{T}}\langle \mathbf{y} \rangle + \mathbf{b}^{\mathrm{T}}(\mathbf{y} - \langle \mathbf{y} \rangle) = \langle x \rangle + \mathbf{b}^{\mathrm{T}}(\mathbf{y} - \langle \mathbf{y} \rangle) \qquad \textbf{(5-14)}$$

which expresses the same retrieval as an adjustment term, $\mathbf{b}^{\mathrm{T}}(\mathbf{y} - \langle \mathbf{y} \rangle)$, added to the box-mean SST, $\langle x \rangle$. This version is computationally rather cleaner, and is the form most convenient to code in practice.

The last aspect to be defined is the weighting of channels in the smoothing adjustment, **b**. The sum of elements of **b** should add to 1 to create a weighted average atmospheric correction across the channels. This could be done be (1) preferring a specific channel, which gets the full weight of 1, (2) weighting all channels evenly, or (3) weighting channels by the inverse of their radiometric noise variance, so that we rely more on low-noise channels for the smoothing. The first of these options has been used in operational centres, but suffers from privileging a single channel arbitrarily. In this reprocessing, the third choice is adopted in order to use the channels optimally, and therefore:

$$b_i = \frac{1/\sigma_i^2}{\sum_i (1/\sigma_i^2)} \qquad \textbf{(5-15)}$$

5.4 Estimates of Uncertainty

Estimates are generated for four sources of uncertainty [RD.306]: (i) uncertainty due to radiometric noise, (ii) uncertainty in retrieval (e.g. insufficient information in the channel to derive an SST estimate), (iii) uncertainty due to large scale effects, and (iv) the uncertainty in the adjustment for diurnal variability (method described in section 8).

For optimal estimation, the uncertainty due to radiometric noise and uncertainty in retrieval are defined respectively as [RD.307]:

$$\sqrt{\boldsymbol{G}\begin{bmatrix}\varepsilon_{3.7}{}^2 & \mathbf{0} & \cdots \\ \mathbf{0} & \varepsilon_{11}{}^2 & \cdots \\ \vdots & \vdots & \ddots\end{bmatrix}\boldsymbol{G}^T} \qquad \textbf{(5-16)}$$

and

$$\sqrt{\boldsymbol{G}\left(\begin{bmatrix}\varepsilon_{RT}{}^2 & \mathbf{0} & \cdots \\ \mathbf{0} & \varepsilon_{RT}{}^2 & \cdots \\ \vdots & \vdots & \ddots\end{bmatrix} + \boldsymbol{K}\boldsymbol{S}_a\boldsymbol{K}^T\right)\boldsymbol{G}^T} \qquad \textbf{(5-17)}$$

where **G** is the gain matrix described in section 3.1.1. (Note: $\boldsymbol{\varepsilon}_{RT}$ depends on the channel wavelength and the satellite zenith angle).

The radiometric noise is assumed to be independent between pixels in an image; (5-17) estimates the SST uncertainty associated with uncorrelated effects. The remainder of the retrieval uncertainty is assumed to be partly correlated between pixels with length scales that are, at present, not well quantified, and are assumed to reflect the length scales of the atmosphere (synoptic length scales), with magnitude obtained from

$$\sqrt{\mathrm{G}\left(\begin{bmatrix}\varepsilon_{\mathrm{RT}}{}^2 & 0 & \cdots \\ 0 & \varepsilon_{\mathrm{RT}}{}^2 & \cdots \\ \vdots & \vdots & \ddots\end{bmatrix} + \mathrm{KS_aK^T}\right)\mathrm{G^T}} \qquad \textbf{(5-19)}$$

For the ATSR-series coefficient-based SST, uncertainty due to radiometric noise is estimated by the propagation of the noise through the retrieval equation. The uncertainty is given by the equation

$$\sqrt{\sum_i \boldsymbol{a}_i^2\boldsymbol{\varepsilon}_i^2} \qquad \textbf{(5-18)}$$

where

i is the channel

εi is the radiometric noise in channel i

a_i are the corresponding channel retrieval coefficients for channel i

The above equation applies for the case of no atmospheric correction smoothing, and is used for single-pixel retrievals that are then averaged in L3U (smoothing is not used in this case). Where atmospheric correction smoothing is applied (for full resolution products), the equivalent expression is:

$$\sqrt{\sum_i \frac{\boldsymbol{\varepsilon}_i{}^2}{\mathbf{1}+\boldsymbol{N}}\left\{\boldsymbol{a}_i{}^2 + \boldsymbol{N}\boldsymbol{b}_i{}^2\right\}} \qquad \textbf{(5-19)}$$

For the uncertainty in the retrieval from algorithm effects, the magnitude is estimated from the residuals in representative simulations of the retrieval process. It is presently assumed that the same correlation length scales apply for the partly correlated effects in both coefficient-based and OE retrievals.

The uncertainty due to large-scale effects is set to be constant (0.1 K) representative of regional, seasonally persistent mean differences against validation values [RD.184].

5.5 SST-level harmonisation

5.5.1 Predictors

Optimal estimation is needed for AVHRR retrieval, particularly with only two channels, in order to constrain biases arising from ambiguous solutions to the atmospheric state. However, OE is also a theory that assumes zero mean biases, whereas instrument calibration errors and RTM errors ensure that there generally are biases that are not zero mean. For this reason, a final step of SST-level harmonisation is required. Having optimised all previous steps to remove biases, this harmonisation step addresses the residual biases between OE SSTs that remain.

SST-level harmonisation is derived from MD. For AVHRRs that overlap with reference sensors (i.e., ATSR-series instruments) the exploited MD consists of AVHRR-ATSR matches. For the ATSR period (and for the Metop-A era after AATSR), harmonisation is therefore to ATSR SSTs. Prior to ATSR-1 (1991) this is not possible; and the 1980s AVHRRs are not sufficiently stable nor have sufficient overlaps to do sensor-sensor harmonisation using current knowledge. Therefore for “the 1980s” the harmonisation MD exploits in situ reference data. Independence from in situ observations for the SST CCI data is therefore violated for the 1980s in the current version. This is justified because users have a stronger requirement for length of record than for independence (RD.385), although independence is preferred.

Thus: Harmonisation is done by fitting difference between AVHRR SST and reference SST.

- For NOAA-12 onwards the reference is ATSR SST retrieval
- For earlier sensors we use ship data (from even days) to fit the predictors, then adjust the constant term to match non-ship data (drifters, bottle, ctd, mbt, xbt)

The primary predictors are listed in Table 5-7 and are calculated separately for N2 and N3 OE retrievals using night-time observations. (N2 is needed for day-time retrievals, but for consistency with N3, the night-time retrieval, it is better to tune it on night-time data.)

Among the harmonisation predictors, there are two terms representing the instrument temperature: T_{inst} is the instantaneous temperature of the internal calibration target (ICT); T_{avg} is the average temperature of the ICT over the orbit. Depending on the instrument either one or neither of these terms is used, as shown in 5-9.

For the recent AVHRRs an additional bias was observed in the daytime N2 retrieval. This is fitted using the predictors in 5-8. As before there are three instrument temperature terms which are used for some instruments.

Table 5-7: List of harmonisation predictors

	Predictor	Comment
1	1	Constant term
2	TCWV	Integrated nadir water vapour path, since SRF uncertainty is often manifested as a dependence on TCWV and functions of the same.
3	TCWV $\sec(\theta_{sat})$	Slant water vapour path
4	$TCWV^2$	Higher-order water vapour dependence
5	$\cos(\theta_{sat})^2$	Across track dependencies
6	jd2000	Julian date relative to 2000-01-01 00:00:00. Enables time variation in harmonisation.
7	T_{inst} - 285	AVHRR internal calibration target temperature, shown to have been predictive of BT biases.
8	T_{avg} - 285	AVHRR "orbital average" temperature, shown to have been predictive of BT biases.

Table 5-8: List of additional daytime predictors

	Predictor	Comment
1	1	
2	θ_{sol}	Orientation of platform to Sun
3	x	Across-track position
4	T_{inst} - 285	AVHRR "ICT" temperature
5	T_{avg} - 285	AVHRR "orbital average" temperature
6	T_{inst} - T_{avg}	Difference between "ICT" and "average"

Table 5-9: Predictors used for each instrument.

Instrument	Reference	Predictors	Additional Daytime Predictors
NOAA-07	In situ	1–6, 8	n/a
NOAA-09	In situ	1–6, 8	n/a
NOAA-11	In situ	1–6, 8	n/a
NOAA-12	ATSR1 + ATSR2	1–6, 7	1–3, 6
NOAA-14	ATSR2	1–6, 7	1–3
NOAA-15	ATSR2 + AATSR	1–6	1–3
NOAA-16	AATSR	1–6	1–3
NOAA-17	AATSR	1–6, 8	1–3, 5
NOAA-18	AATSR	1–6	1–3
NOAA-19	AATSR	1–6, 7	1–3, 4
Metop-A	AATSR	1–6, 7	1–3, 4

5.5.2 Example results

Example results are shown for AVHRR on NOAA 11.

a.

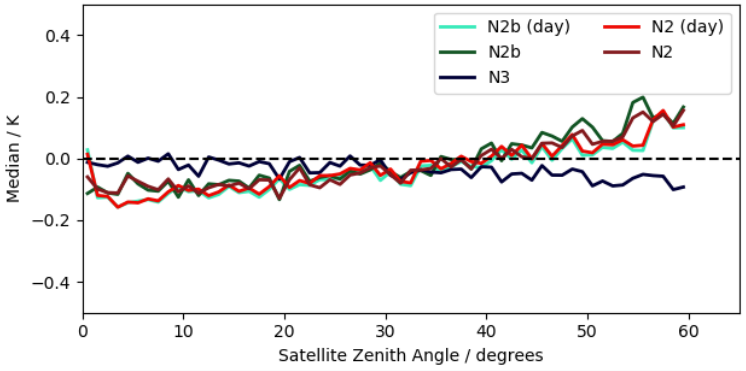

b.

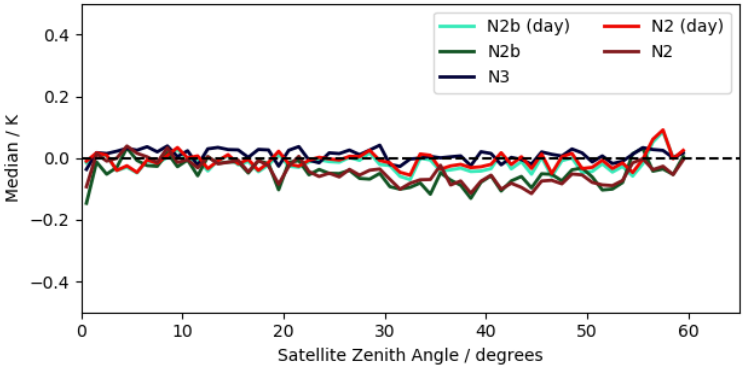

c.

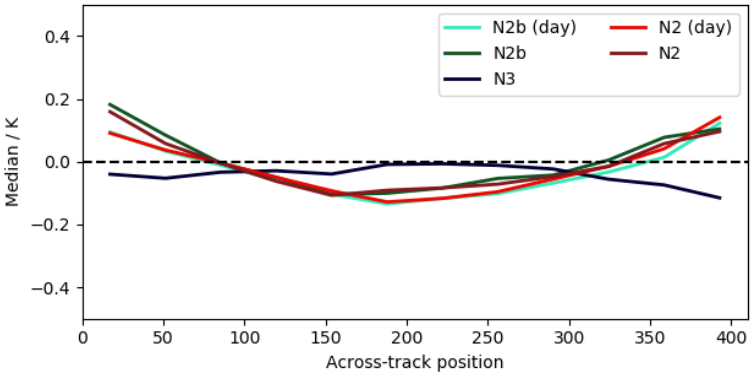

d.

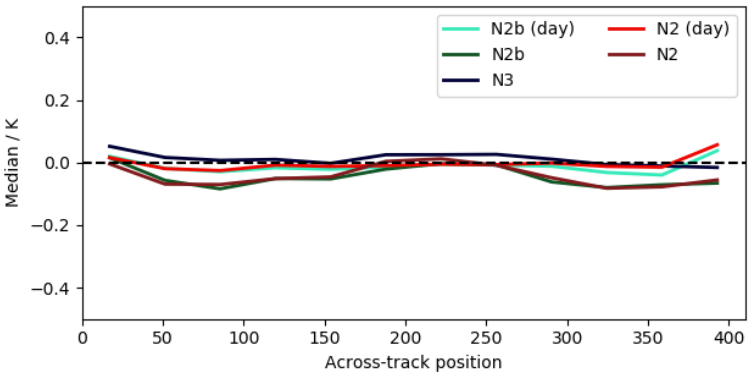

Fig. 5-4 OE-SST dependencies addressed by SST-level harmonisation. Pre-harmonisation (a, c) and post-harmonisation (b, d) dependence on satellite zenith angle and across track position respectively. Example shown is NOAA-11 against ship-based in situ measurements. Harmonisation is done on the N2 night-time data (dark red curves) and results for N2 day-time comparisons are in bright red. N3 is

the night time algorithm (black). The N2b algorithms are alternative algorithms not used in SST CCI processing.

5.5.3 Future enhancements

The SST-level harmonisation of OE here is effective, but heavily reliant on expert judgement. A more systematic approach that integrates more closely with the OE framework would be preferable.

The need for SST-level harmonisation is reduced as AVHRR BT biases are reduced. Exploitation of improved level-1 (from the project FIDUCEO) will reduce but may not remove the need to harmonise OE SSTs to an external reference.

Integrated exploitation of AVHRR BTs with HIRS BTs will further reduce systematic effects in AVHRR OE SSTs, because (1) differing biases in different sensors will to some degree cancel and (2) it will allow additional AVHRRs to be used in at least some circumstances (with different error characteristics). This is the focus of IR algorithm development proposed for Phase 3.

6. GENERATION OF L2P AND L3U PRODUCTS AND PROPOGATION OF UNCERTAINTIES

This section describes the processing chain used to generate L2P and L3U outputs from the L1B satellite observations. The individual steps referred to are described in detail in other sections of the document as follows; cloud clearing (section 4), SST retrieval (section 5) and SST depth and time adjustments (sections 7 and 8).

6.1 Generating L2P with Quality Level

The first step in the processing chain is to cloud screen the input data (section 2). This is done using a Bayesian methodology for both the ATSR and AVHRR instruments, taking L1B observations and NWP data as input. For cloud free scenes the skin SST is retrieved using optimal estimation for the AVHRRs and coefficient based retrieval for ATSRs. Skin SST is then adjusted for both time and depth to provide a bulk SST at one of the two reference times, 10.30 or 22.30 local times that are used as estimates for the daily mean SST (sections 7 and 8). For AVHRR instruments this per pixel data along with the associated uncertainties is output in L2P product format. Uncertainties associated with the SST retrieval are broken down into uncertainty from

- large scale correlated effects,
- synoptically correlated effects
- uncorrelated effects, and
- time and depth adjustment.

In addition to uncertainty calculation, a quality level is defined. We treat quality level as a concept that is distinct from uncertainty: a highly uncertain SST can have the highest quality level if all the conditions for giving a valid SST and valid SST uncertainty are met: the quality level reflects the degree of confidence in the validity of the uncertainty estimate, not the data uncertainty.

The quality_level assigned to a pixel will be the lowest level (row of table) which matches any of the conditions shown in the table below. The assignments are compatible with GHRSST conventions: i.e., a particular level is given if none of the conditions higher up any column of the table are met.

Table 6-1: Quality level definitions

level	meaning	P(clear)	sensitivity	χ2	Other			
0	no_data	< 0			No data	Is Land		
1	bad_data	< 0.5	< 0.5	> 3	T11 < 260	SST < 271.15	ice detected	NWP missing
2	worst_quality	< 0.8	< 0.9	> 2	θsat > 62			
3	low_quality	< 0.9	< 0.95	> 1	87.5 < θsol < 92.5			
4	acceptable_quality				abs(ASDI) > 0.2			
5	best_quality							

For instance, any pixel where P(clear) is unavailable (value is less than zero), required input BTs are unavailable, or which is over land will be assigned quality level of 0. Next, any pixels which have P(clear) < 0.5, calculated SST sensitivity < 0.1 etc. will be assigned quality level of 1 and so on.

Quality level 0 pixels should contain no other data (except land flag in l2p_flags)

Quality level 2-5 pixels should always contain valid data

Quality level 1 pixels may contain data in some variables but the data is not suitable for use (bad_data). For instance, the SST retrieval may have been attempted, but rejected as bad_data due to low sensitivity etc. Or if the retrieved SST is out of range (< 271.15 K) then the value will be missing in the output file.

The processor performs SST retrieval for all pixels with P(clear) > 0.1

6.1.1.1 Interaction of quality level and L3 Regridding

When regridding the SST data to the L3 grid, only the highest quality_level data in each cell will be used as specified in GDS 2.0r5.

L3 data is generated from the unsmoothed (single-pixel) SST retrieval. This is done:

- to simplify the propagation of uncertainties
- because atmospheric correction smoothing is unnecessary for L3 as regridding to lower resolution reduces the uncorrelated uncertainty in a similar way

6.1.1.2 Interaction of quality level with L2P atmospheric correction smoothing

When applying atmospheric correction smoothing or the smoothed optimal estimation algorithm, only pixels with quality level equal or greater than the central pixel shall be considered.

For instance, a quality_level 5 pixel will only use surrounding pixels of quality_level 5 for the smoothing step. Whereas a quality_level 3 pixel may use surrounding pixels of quality_level 3 or greater.

6.2 Generating L3U Data from L2P Data

For the ATSR instruments the data are averaged across 0.05° grid cells and provided as L3U products. Skin and depth SSTs are calculated within each grid cell using data classified as clear-sky during the cloud screening process. Uncertainties are also propagated onto the reduced resolution grid with the addition of a sampling uncertainty (next subsection) and provided with same components as those described in section 6.1.

6.3 Sampling uncertainty estimate on the L3U grid

Sampling uncertainty is introduced in gridded products where the data are not fully sampled due to the presence of cloud. We implement a sampling uncertainty model dependent on the percentage of clear-sky pixels in the grid cell and the standard deviation of the SST in the observed pixels. This model is applicable to SST retrieved using any instrument or algorithm provided that the uncertainties due to radiometric noise are correctly propagated and removed prior to calculation of the sampling uncertainty (Bulgin et al, 2015).

Sampling uncertainty is calculated for each L3 grid cell using all available clear-sky pixels. The standard deviation of SST in the available clear-sky pixels in calculated following subtraction of the uncertainty due to radiometric noise in variance space.

$$SST_{std} = \sqrt{\mathrm{var}(SST_{clear\_pixels}) - \mathrm{var}(radiometric_{clear\_pixels})} \qquad \textbf{(6-1)}$$

Sampling uncertainty is modelled using a cubic fit for six bands of SST_{std} which range between 0.0-0.6 K with a width of 0.1 K (Bulgin et al, 2015). The sampling uncertainty model is shown in Figure 6.3.1. At present we implement only the curve for 25 pixel extracts (5x5 pixels) which represents 0.05° sampling. The effect of small variations in pixel number within a given grid cell on sampling uncertainty is negligible as shown by the close similarity between curves for 5x5 and 10x10 pixel areas (Figure 6-1), so this model is applicable at all latitudes.

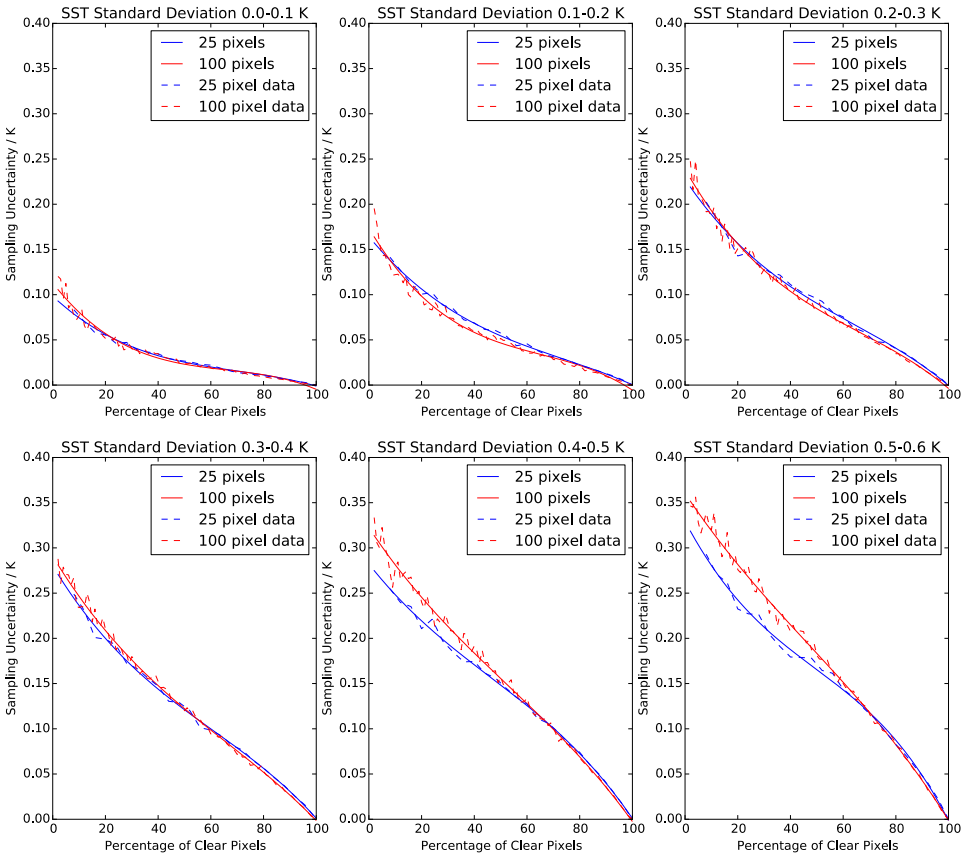

Figure 6-1: Modelled sampling uncertainty as a function of the percentage of clear-sky pixels for six bands of SST_{std}. Blue lines show data calculated for 25 pixel extracts corresponding to 0.05° at the equator and blue lines show 100 pixel extracts corresponding to 0.1° at the equator. Dashed lines show the raw data and solid lines the cubic fit.

Having calculated the percentage of clear-sky pixels in a given grid cell ($clear_{percent}$), a cubic fit in the form:

$$Sampling\_Uncert = af_{\%clear}{}^{3} + bf_{\%clear}{}^{2} + cf_{\%clear}{}^{1} + d \qquad \textbf{(6-2)}$$

is found (solid lines in Figure)

The coefficients for the curves are given in Table 6-2.

Table 6-2: Sampling uncertainty cubic function coefficients.

SST_{std}	a	b	c	d
0.0-0.1 K	-1.53×10^{-7}	3.22×10^{-5}	-2.69×10^{-3}	9.82×10^{-2}
0.1-0.2 K	-1.54×10^{-7}	3.42×10^{-5}	-3.52×10^{-3}	0.16
0.2-0.3 K	-2.16×10^{-7}	4.17×10^{-5}	-4.28×10^{-3}	0.23
0.3-0.4 K	-2.48×10^{-7}	4.49×10^{-5}	-4.81×10^{-3}	0.28
0.4-0.5 K	-2.31×10^{-7}	3.19×10^{-5}	-3.69×10^{-3}	0.28
0.5-0.6 K	-4.53×10^{-7}	6.73×10^{-5}	-5.51×10^{-3}	0.33

6.4 Other Data Provided in the L2P and L3U Files

The L2P and L3U files also contain flags to assign each pixel or grid cell as land/ocean or sea ice and to record how many channels were used in the SST retrieval. If a pixel or grid cell crosses a boundary then both of the applicable conditions will be flagged.

7. MODEL OF SKIN-SUBSKIN DIFFERENCE IN SEA SURFACE TEMPERATURE

7.1 Background

The upper few millimetres of the ocean is referred to as the skin layer. This is cooler than the sub-skin layer immediately below due to latent and sensible heat exchanges with the atmosphere and surface emission of infrared radiation. The sub-skin layer exhibits a diurnal variation in temperature and depth, governed by absorption of solar radiation and wind driven mixing. The deeper mixed layer of the ocean lies below this and is largely unaffected by surface processes. The temperature of this layer is often referred to as the bulk sea surface temperature, and is best characterised by SSTs at named depths below the surface.

Space-borne infrared instruments measure the temperature of the upper few microns of the sea surface whilst in-situ data from buoys or ships are typically a measure of the bulk SST. Depth adjustment of the retrieved SST is necessary to meet user requirements of consistency between satellite and in-situ data records. The SST at a target depth is calculated from the skin SST in a two-step process, first adjusting for the cooler skin layer and then for the warm sub-skin layer. This section describes the algorithm used to calculate the sub-skin SST from the skin SST and section 6 details the adjustment from the sub-skin temperature to the bulk SST.

7.2 Model Setup

The temperature difference (ΔT) between the skin and sub-skin SST is described by the following relationship [RD.319].

$$\Delta \boldsymbol{T} = \frac{\boldsymbol{\lambda Q_{\upsilon}}}{\boldsymbol{k u_{*}}} \qquad \textbf{(7-1)}$$

where

ΔT_c temperature difference across the skin to sub-skin layer (K)

Q total cooling at the ocean-atmosphere interface (W m^{-2})

Δ thickness of the cool skin layer (m)

K thermal conductivity of water (Wm^{-1} K^{-1})

This can be parameterised under shear and buoyancy driven conditions denoted by subscripts (s) and (b) respectively [RD.227].

$$\Delta T_{cs} = \frac{\lambda Q v}{k u_{*w}} \qquad \textbf{(7-2)}$$

$$\Delta T_{cb} = \left(\frac{v}{A^3 g \alpha \rho c_p k^2}\right)^{1/4} Q / Q_b^{1/4} \qquad \textbf{(7-3)}$$

where

λ	empirical coefficient
v	kinematic viscosity of water (m^2 s^{-1})
ρ	density of sea water (kg m^{-2})
u_{*w}	friction velocity in the ocean for turbulence generated by convection (m s^{-1})
A	empirical constant
g	gravitational acceleration (m s^{-2})
α	thermal expansion coefficient for water (K^{-1})
c_p	specific heat capacity of water (J kg^{-1} K^{-1})

The Fairall model combines the shear and convective effects to define λ used in the calculation of the thickness of the cool skin layer (δ). This gives an expression for the skin depth that is valid both at low-wind speeds (when convective effects dominate) and at higher wind speeds (when shear dominates). In the Fairall model, λ is given by equation 7.4 where λ_0 and *A* are pre-determined coefficients, set to 6.0 and 0.23 respectively [RD.227].

$$\boldsymbol{\lambda = \lambda_0 \left[1 + \left(\frac{\lambda_0^4 A^3 Q g \alpha \rho c_p v^b}{u_{*a}^4 \left(\rho_a/\rho\right)^2 k^2} \right)^{3/4} \right]^{-1/3}} \qquad \textbf{(7-4)}$$

We drive the Fairall model with ERA-Interim numerical weather prediction (NWP) data, available globally at 6 hour time intervals from 1979 [RD.38]. A weakness of the approach is that any trend in NWP wind speed bias will introduce an artefact in the depth-adjusted SST record (both here, and in the subskin to depth adjustment). On the other hand, this approach also allows larger trend artefacts related to the diurnal cycle and satellite overpass times to be reduced. NWP re-analysis data are the only usable source of data that are relatively consistent across the required period since 1981.

Over a wind speed range of 0-10 m s^{-1} the Fairall model has been shown to give the best estimate of the skin to sub-skin temperature difference [RD.262]. In RD.266 the optimal parameterisations of *A* and λ were considered and an alternative proposed set of coefficients (*A* = 0.15, λ = 4.1) [RD.266] derived, which are used for EXP 1.8.

7.3 Forcing Data for the Skin to Sub-Skin Model

The NWP data used is ERA-Interim, which has a resolution of 0.75° latitude and longitude. The model implementation follows that of the UK Met Office [RD.262] and is designed to use 6-hourly fields, using 3-hourly forecast fields coincident with the 6-hourly analysis fields. Table 7-1 lists the fields used to force the skin-to-sub-skin SST model.

Table 7-1. NWP inputs to the Fairall-Kantha-Clayson model. ERA-Interim codes are provided in brackets, acronyms 'an' and 'fc' refer to analysis and forecast fields respectively.

ERA-Interim Field and Code	Fairall Kantha-Clayson Field
SST (34, an)	SST (Fairall, and to initialise KC)
10m E wind (165, an)	10m wind speed (to initialise KC)
10m N wind (166, an)	10m wind speed (to initialise KC)
Sensible heat flux (146, fc)	Non-solar heat flux
Latent heat flux (147, fc)	Non-solar heat flux and latent heat flux
Net surface thermal radiation (177, fc)	Non-solar heat flux
Net surface solar radiation (176, fc)	Solar heat flux
E turbulent stress (180, fc)	Wind mixing energy (friction velocity)
N turbulent stress (181, fc)	Wind mixing energy (friction velocity)

7.4 Uncertainty estimate

It is necessary to estimate the uncertainty in the skin model when forced by the ERA-interim NWP. The data used above (Figure 7-2). consist of a double difference between day and night, skin minus sub-skin SSTs; in each case, this double difference removes the satellite SST minus buoy bias (which is the same for the day and night). The uncertainty estimate therefore includes variance in both the satellite and buoy measurements and variance in the cool skin temperature. The random uncertainty in the buoy measurements is estimated as 0.04 K [RD.266]. For group three, defined in section 5.2, where all 81 pixels in the match-up were classified as clear–sky, the model minus observation variance is defined below [RD.266]. The time window was reduced to ±1 h to reduce the variation due to changes in the slope of the mean difference.

$$\sigma^2_{\text{model-obs,day-night}} \approx 0.045\ K^2 \qquad \textbf{(7-5)}$$

The estimated variance due to instrument and buoy noise and is

$$\sigma^2_{\text{AATSR+buoy,day-night}} \approx 0.014\ K^2 \qquad \textbf{(7-6)}$$

implying a total uncertainty of

$$\sigma^2_{\text{skin-0.2m,day-night}} \approx 0.031\ K^2 \qquad \textbf{(7-7)}$$

which is approximately 4 times larger than the model variance [RD.266].

7.4.1 Model for Residual Bias and Uncertainty

The skin minus sub-skin SST differences between day and nighttime observations in Figure 5.2 indicate that the residual bias can be assumed to be zero. The residual variance (σ^2) within ±6 h of the adjustment time can be approximated using a linear fit

$$\sigma^2 = b\,[t - t_0] \qquad \textbf{(7-8)}$$

where

t observation time

t_0 adjustment time

b constant

b is defined with respect to the adjustment and observation times:

b = 0.0040 for: t_0 = 10:30, 04:30 < t < 10:30

b = 0.0012 for: t_0 = 10:30, 10:30 < t < 16:30

b = 0.0012 for: t_0 = 22:30, 16:30 < t < 22:30

b = 0.0009 for: t_0 = 22:30, 22:30 < t < 04:30

7.4.2 Temporal and spatial correlations

The temporal and spatial correlation of the skin SSTs will be dependent on the meteorological situation. The cool skin is an instantaneous effect of solar insolation and wind speed, independent of their history, and therefore the correlation scales are likely to be smaller than those for the sub-skin layer (section 8.4.1). The correlation time is in the region of 6 hours with a correlation distance compatible with the NWP grid resolution of 0.75° [RD.266].

8. MODEL OF SUBSKIN-DEPTH DIFFERENCE AND TIME-ADJUSTMENT DIFFERENCE

8.1 Background

As described in Section 5.1, to derive bulk SST from satellite observations of skin SST two corrections have to be applied: first an adjustment from the cool skin to the warmer sub-skin layer and second an adjustment from the sub-skin layer to the bulk SST. This second step requires an estimation of the stratification of the near-surface ocean between the sub-skin and the target depth, as the sub-skin layer exhibits a depth dependent diurnal cycle in SST. The CCI project generates SST retrievals from a number of satellite instruments, making observations at different local times. In order to compare these observations with one another and with historical in-situ observations of SST a time adjustment is also applied. Both depth and time adjustments will be described in this section.

8.2 The Model

8.2.1 Model Choice

The Kantha-Clayson model is used to make the sub-skin to bulk SST correction. This is coupled with the Fairall model for skin to sub-skin temperature conversion described in Section 5. The Kantha-Clayson model describes turbulence in geophysical boundary layers on the basis of second order closure models. It includes shear instability mixing in the stratified ocean, below the sub-skin layer, and diffusive heat transfer [RD.263, RD.262]. As with the Fairall model, it uses NWP data to describe local ocean-atmosphere conditions.

8.2.2 Model Setup for Sub-Skin to Bulk SST Adjustment

The Kantha-Clayson warm layer model is implemented using code provided by the UK Met Office. The model vertical resolution decreases with depth: from two centimetres at the surface to sixty centimetres at a depth of ten metres, and is run at a temporal resolution of ten minutes. In the UK Met Office implementation, the evolution of temperature (T) over time (t) for a single layer is defined as

$$\frac{T}{t} = \frac{1}{z}\,\frac{v}{\sigma_p} + K_H\,\frac{T}{z} + \frac{Q}{\rho C_p} \qquad \textbf{(8-1)}$$

where

- z layer depth
- v molecular viscosity
- σ_p molecular Prandtl number
- K_H turbulent diffusion
- Q heat source
- ρ layer density
- C_p specific heat capacity of seawater

The molecular mixing terms defined in the model (K_{HB} and K_{MB}) were modified to represent the diurnal thermocline rather than the entire oceanic mixed layer [RD.262]. Background salinity is set at 35 PSU and modified by evaporation although no precipitation is included in the model [RD.262, RD.266]. ERA-Interim NWP fields are used as input at a 6 hourly temporal resolution. At each time step, the sub-skin to depth temperature differences are output for depths of 0.2, 1.0 and 1.5 metres.

8.2.3 Model Setup for Time Adjustment

As the Kantha-Clayson model needs a few hours to stabilise, it is initialised from a start time 17 hours earlier than the first dawn prior to the reference time: 12 hours for the adjustment period and a further 5 hours for the model initialisation. This gives a maximum lead time of 24 plus 17 hours prior to the SST adjustment time as the model has to be initialised just before dawn. The first stage of the implementation is to produce the fields in the second column of Table 7-1 at a six hour temporal resolution.

The input fluxes are then interpolated to the model temporal resolution of ten minutes. Non-solar fluxes and fields are interpolated using Lanczos re-sampling, over a period of 12 hours (i.e. two 6-hour NWP model time-steps). The UK Met Office method [RD.264] is used to interpolate the solar flux. The equivalent peak insolation is calculated from the six hourly fluxes, linearly interpolated in time, and used to derive the solar flux.

8.2.4 Model Parameter values

The parameters recommended for the Kantha-Clayson model set-up are described in detail in RD.266.

8.3 Model Performance and Criteria for Time Adjustment

Model performance is assessed using data from the Multi-Match-up Database (MMD) [RD.266]. For each match-up a time series of buoy measurements is available. Assuming two or more measurements, a dataset of temperature differences between the reference and adjustment times is constructed, using each measurement in turn as the reference time. Similarly, the same set of differences is calculated from the model time series and using the model minus measurement differences. The results are binned into ten minute time steps corresponding with the model output. For each match-up the time range for inclusion of satellite observations or in-situ measurements is ±12 h around the reference time.

The mean diurnal cycle of temperature differences are shown in Fig 8.1, compared against buoy data. The model follows the measured diurnal cycle very closely with a lead of approximately 1.5 h, giving a residual difference of about 1/5 of the observed diurnal cycle. The phase shift may be due to errors with the NWP fields of their interpolation; it is not clear what physical effect would give a phase lead in the Kantha-Clayson model [RD.266].

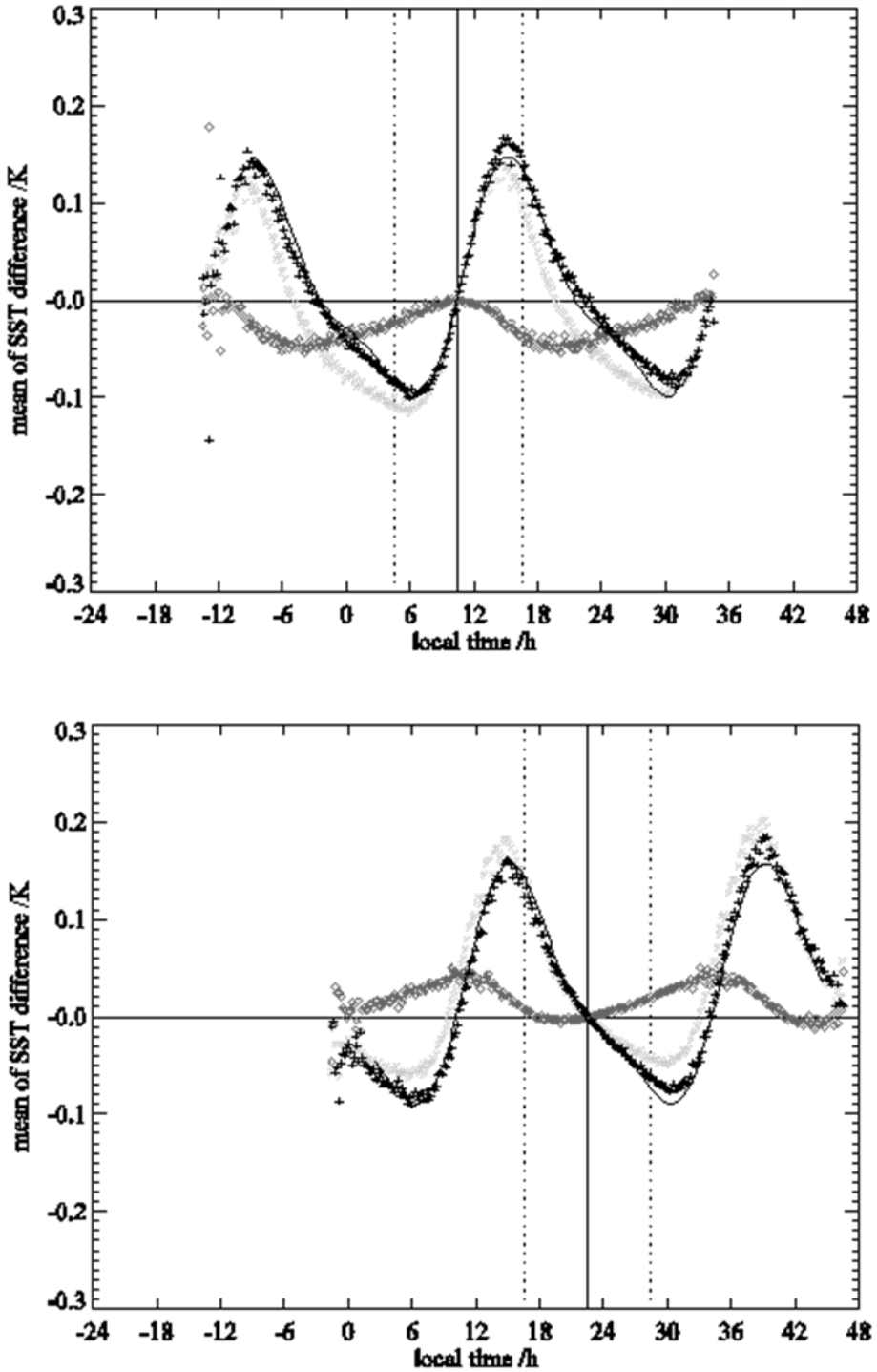

Figure 8-1. Plots show the mean change in SST difference away from the adjusted times (10.30 for the top panel, 22.30 for the bottom panel). Specifically, we plot T0.2m (reference time) − T0.2m (adjustment-time). Black +, drifting buoy measurements; pale grey x, Kantha-Clayson model; grey ◊, model−buoy. The lines through the points show the fit to diurnal and semi-diurnal harmonics (section 6.4). Dotted lines are ±6h from the adjustment time.

Satellite observations are adjusted to the standard observation times of 10.30 and 22.30 when the sub-skin temperature is closest to the mean daily temperature. The ATSR instruments most closely match these observation times and currently provide the most accurate SST retrievals. Figure 6.2 shows the variance between the time-adjusted SST and reference SST for buoy and model measurements at both 10.30 and 22.30, using data from the MMD. One option for choosing the reference time against which to adjust the observation is to pick the condition under which the variances are approximately equal. Figure 8-2 shows that this would result in more observations being corrected to 22.30 than 10.30. The observations are therefore adjusted by choosing the closest reference time. This has the advantage over assigning 'day' and 'night' conditions of achieving a maximum time difference between the observation and reference time of six hours.

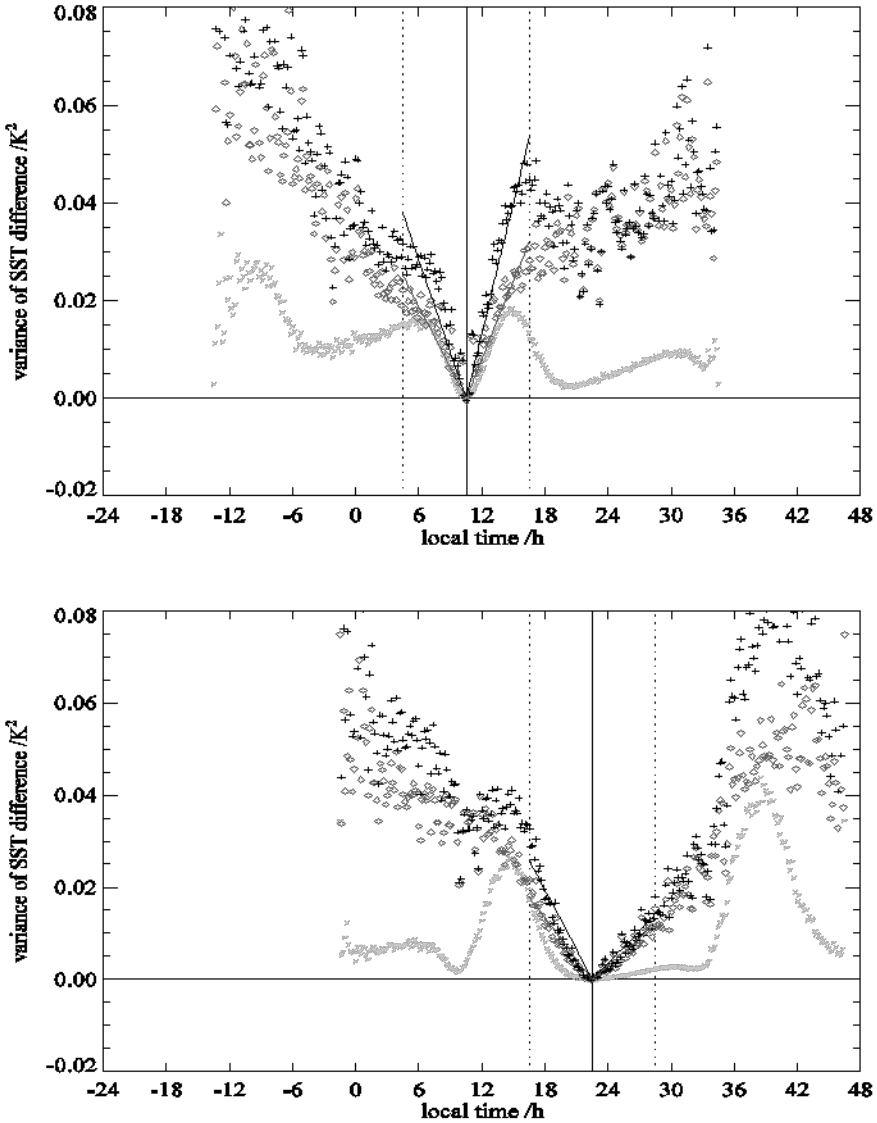

Figure 8-2. Variance of $T_{0.2m}$(reference time) − $T_{0.2m}$(adjusted-time). Black +, drifting buoy measurements; pale grey x, Kantha-Clayson model; grey ◊, model−buoy. The lines through the points are linear fits constrained to zero at 10.30 (top panel) and 22:30 (bottom panel). Dotted lines are ±6h from 10.30 and 22:30. Buoy and model−buoy have the estimated combined buoy random noise and discretisation error (variance=0.04^2) subtracted. The curves for the measurements and the difference have been reduced by the estimated variance for the buoy temperature differences of 0.0016 K^2.

8.4 Quantification of Uncertainty

The residual bias shown in Figure 8.1 can be fitted to a combination of diurnal and semi-diurnal harmonics:

$$e = a_0(t_0) + a_1 \cos\left(\frac{2\pi(t-\varphi_1)}{24}\right) + a_2 \cos\left(\frac{2\pi(t-\varphi_2)}{24}\right) \quad \textbf{(8-1)}$$

where

$a_1 = 0.022$

$a_2 = 0.0043$

$\varphi_1 = 9.5$

$\varphi_2 = 11.6$

$a_0(10.30) = -0.025$

$a_0(22.30) = 0.017$

These functions are plotted in Figure 8-2 and the fit is excellent within ±6 h of the reference times. The residual variance can be approximated within ±6 h of the reference time by a linear fit:

$$\sigma^2 = b\,[t - t_0] \quad \textbf{(8-2)}$$

where

t observation time

t_0 adjustment time

b constant

b is defined with respect to the adjustment and observation times:

b = 0.0042 for: t_0 = 10:30, 04:30 < t < 10:30

b = 0.0054 for: t_0 = 10:30, 10:30 < t < 16:30

b = 0.0030 for: t_0 = 22:30, 16:30 < t < 22:30

b = 0.0020 for: t_0 = 22:30, 22:30 < t < 04:30

8.4.1 Temporal and spatial correlations

The temporal and spatial correlation of time and depth adjusted SSTs are dependent on the meteorological situation. At small scales, correlation times can be less than an hour [RD.222] and correlation distances can be less than 25 km [RD.265].

An estimate of the correlation time for the residual error can be made from the variance curves (Figure 8.2). The errors appear to be correlated to about 6 h for the 10:30 adjustments and 8 h for 22:30 adjustments. Variance curves calculated for other reference times have a similar shape and scale with a correlation time near 6 h.

The in-situ information in a match-up is at a single point, so there is no information from which to estimate the spatial correlation. This is assumed to be similar to NWP grid scale at 0.75°.

$$BT_{channel} = BT_{channel} + (aerosol\_mode_{channel} \times aerosol\_index_{channel}) \quad \textbf{(4-2)}$$

8.5 Skin and diurnal models: limitations and future enhancements

The diurnal and skin models work well and are well-justified, but are implemented in non-maintainable legacy code from the UK Met Office [RD.266]. Moreover, Wick et al. [RD.398] have demonstrated scientific improvements in the low-wind regime for use in K-C models of this sort, which are not included in this code base. Therefore, it is desirable to use to the more recent and maintainable code base of Mittaz et al. [RD.399].

Users [RD.400] have a clear preference for adjustment of the instantaneous depth SST to a daily mean rather than a reference time. The diurnal cycle of SST is such that the reference times chosen give a reasonable estimate of the daily mean on average [RD.396], but future work will develop a technique to estimate the daily mean and the adjustment uncertainty directly.

9. QUALITY LEVEL ATTRIBUTION

Quality indication. A confidence level on a scale 0 to 5 is provided for each SST as a quality indicator, following GHRSST conventions. Five (QL = 5) indicates the highest confidence. Levels 4 and 5 should be used for climate applications where absolute accuracy of SST is important. Some users may find lower quality level data useful, e.g., where SST front locations are detectable in the SST fields, which requires only relative, not absolute, accuracy.

The quality indicator represents the confidence we have that the SST uncertainty estimate for a given SST is valid. SSTs with relatively high uncertainty can still therefore be flagged as good quality, provided there is nothing to indicate that the assumptions made in estimating the uncertainty are compromised. The most significant quality factors are undetected cloud and coarse-mode aerosol (primarily desert dust): the uncertainty estimates for SST are valid under clear-sky, low-aerosol conditions, and therefore the quality levels 4 and 5 are attributed only for high clear-sky probability and acceptable desert dust index[i]. (The desert dust index is only available to check for the ATSR series sensors, since it relies on having dual-view observations.)

In the case of optimally estimated SSTs, the goodness-of-fit of posteriori simulated and observed brightness temperatures is calculated, using a χ^2 statistic. Large values of χ^2 indicate that the inter-relationships of the brightness temperatures are not as expected for a clear-sky observation given the background information. The quality levels of pixels with large χ^2 are therefore downgraded.

In order to maximise the use of this dataset for assessing in situ based SST estimates and for model testing, it is important for the SSTs to have high sensitivity to true SST variations (which means minimal dependence on the prior SST information). For this reason, SSTs with low sensitivity are downgraded.

The thresholds and logic for quality level assignment are shown in Figure 3. Note that, because the desert dust indicator is only available for the ATSR series, AVHRR SSTs are not expected to have quality level equal to 4.

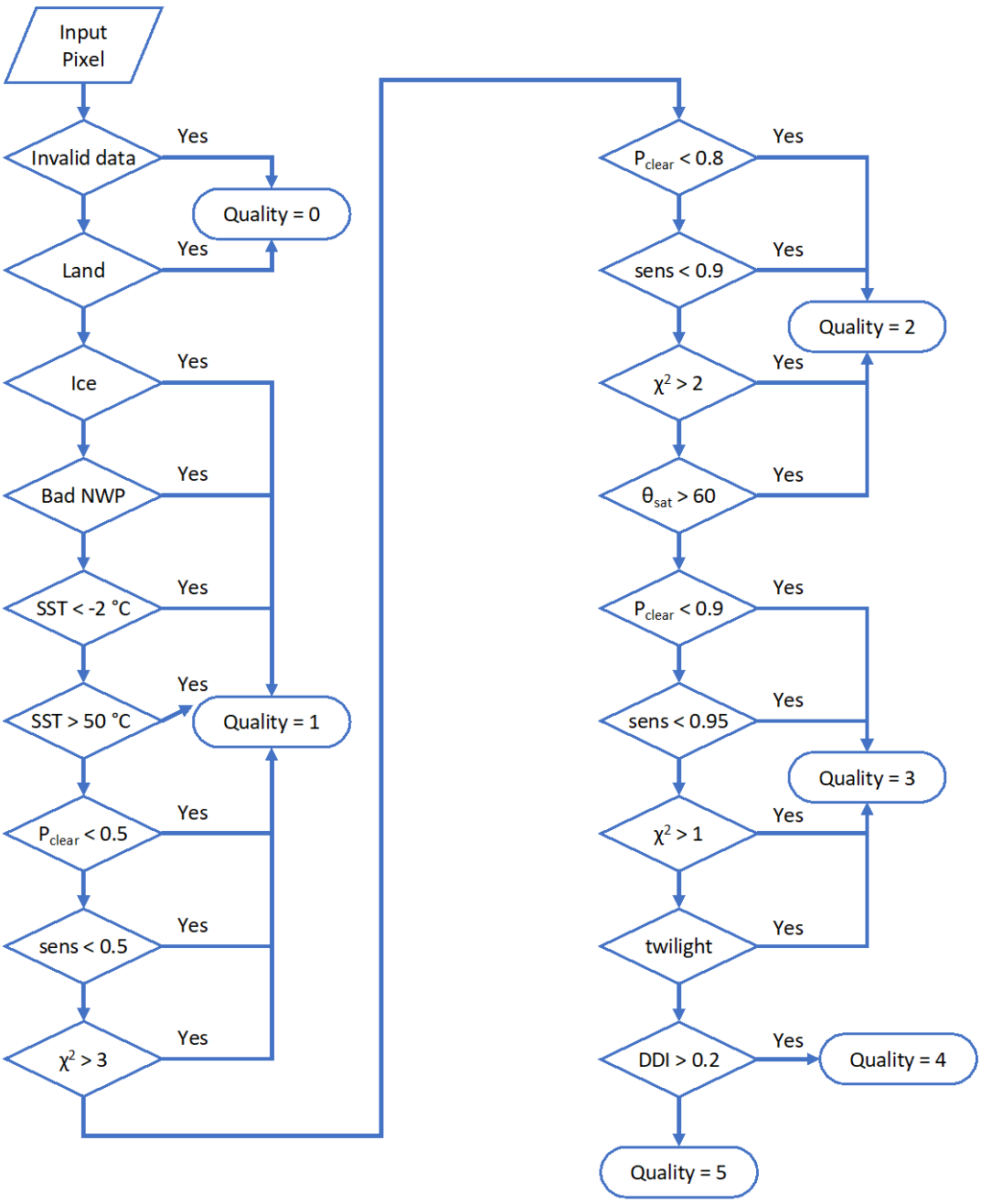

Fig. 9-1. Flowchart for quality indication in "Quality Levels". Quantities tested for QL are: SST grossly out of range; P_{clear} (the result of the Bayesian cloud detection calculation); SST sensitivity ("sens"), which estimates the fractional change in retrieved SST for a unit change in true SST; and the goodness of fit (in the case of OE retrievals) after retrieval (χ^2). The P_{clear} threshold for QL 5, namely 0.9, applies for the case of ATSR-series instruments and AVHRR night-time; for AVHRR day-time the value is 0.99.

10. L4 ANALYSIS

The SST CCI L4 analysis system is the Operational Sea Surface Temperature and Sea Ice Analysis (OSTIA) system. It was developed at the Met Office where it is run in near-real time (NRT) daily [RD.213]. OSTIA uses satellite and in-situ SST data, together with sea ice concentration data, to produce a global gridded SST and sea ice analysis on a 0.05° grid with no data gaps (known as a 'Level 4' data product). OSTIA reanalysis systems have been developed largely based on the near real time (NRT) system and have been used to produce a SST reanalysis for the period 1985 to 2007 (OSTIA reanalysis v1.0) [RD.239]. This reanalysis system was used in the first phase of the CCI SST project to produce the Level 4 product using satellite data only [RD.175]. The analysis process in OSTIA is not described in detail here; instead the reader is referred to OSTIA publications [RD.213, RD.239] and upgrade descriptions for OSTIA work under SST CCI in a previous ATBD release [RD.387].

10.1 Background

Since 2018, the operational OSTIA analysis has been a variational assimilation scheme, called NEMOVAR. Under SST CCI, this change has included introduction of flow-dependent background error correlation length scales. This provides upgraded feature resolution compared to previous analyses.

A full description for publication is in preparation [RD.407]. To generate a spatially complete L4 analysis involves gap-filling relative to the input satellite data (which because of swath and cloud limitations are never spatially complete for a given day). Gap-filling algorithms tend to have the side effect of smoothing results, even where observations are plentiful and spatially contiguous, the degree of smoothing being heavily influenced by length-scale parameters

Briefly, the principle of variational assimilation for solving this problem is to minimise a cost function

$$J(\delta x) = \frac{1}{2}\delta x^{\mathrm{T}} B^{-1}\delta x + \frac{1}{2}(d - H\delta x)^{\mathrm{T}} R^{-1}(d - H\delta x)$$

Where x describes the system state (the field of SST), δx is the change of ocean state for the present day's analysis relative to the background (which is an estimate of the current day's SSTs from persisting anomalies from the previous day's analysis), B is the error covariance matrix estimate representing how wrong the background can be as an estimate for today, R is an error covariance matrix for observations, *d* contains the differences between the observations and the background and *H* is the linearised observation operator which interpolates the analysis grid to the observation locations; therefore $d - H\delta x$ is the difference between observed SSTs (at their particular times and places) and the corresponding expected SSTs given a particular solution for δx. The minimisation is therefore a compromise between the prior expectations for the SST field given the previous day's result and the new SST observations, weighted according to their respective degree of uncertainty. B is too large a matrix to store and invert and is therefore parameterised.

The core of the improvements to OSTIA in this phase II work is the improvement in the parameterisation of B. The concept of flow-dependent length-scale formulation is to make a length-scale (smoothing) parameter within the B parameterisation shorter (less smoothing on medium and long scales) where possible and useful – essentially, in situations where there are data and where the background (prior field from previous analysis) suggests that SST gradients are strong. (Smoothing is not detrimental where SST gradients are weak or zero.)

10.2 Algorithm concept

This is actually done by adjusting the weighting between a long and short length scale in the assimilation scheme: increasing the weighting given to the short length scale better preserves features. This is illustrated below.

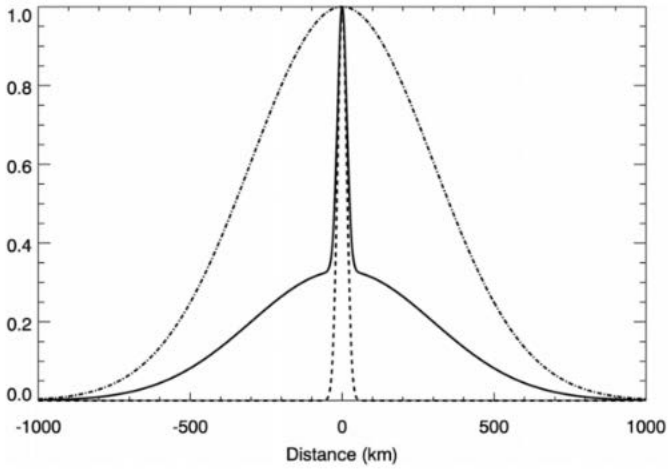

Fig. 10-1. Control over long versus short error correlation length scales in variational assimilation. The correlation as a function of separation distance is shown, modelled as a linear combination (solid line) of Gaussian functions (dashed line). The relative weight of the Gaussian functions is changed using a flow-dependent parameterisation. This is an innovation introduced for the v2 SST CCI analysis that improves the feature resolution of the analysis product.

The parameterisation takes as input the total SST gradient in the previous day's analysis, e.g. Fig 10-2. Where the total gradient is less than 20 mK km^{-1}, the long length scale is highly weighted and where the total gradient exceeds 50 mK km^{-1}, the short length scale is highly weighted. For intermediate gradients the linear interpolation of these extremes is applied.

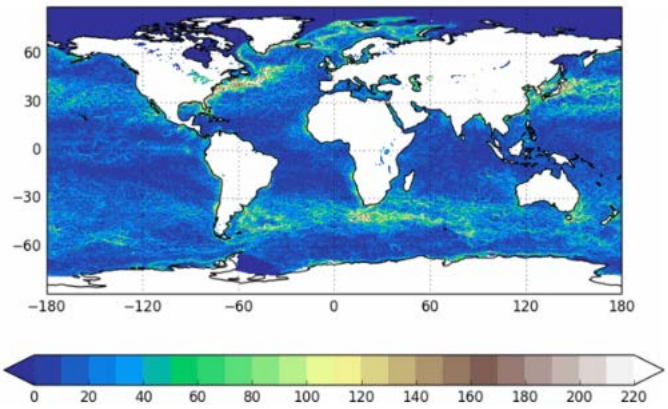

Fig. 10-2. Example field of total SST gradient in the new OSTIA analysis system, in mK km^{-1}. The relative weight of the long-scale Gaussian shown in Fig 10-1 is reduced wherever the gradient exceeds 20 mK km^{-1}, and takes a minimum value for locations where the gradient exceeds 50 mK km^{-1}.

In this way, B is adapted to the local flow conditions (i.e., the strengths of SST gradients).

10.3 Example results

The standard deviation between the new OSTIA analysis and VIIRS SST measurements is a measure of the relative uncertainty in different versions of the analysis. Using a configuration in which the flow dependence is introduced and a short length scale of 15 km is adopted, this measure is improved in all basins (SD reduces, Fig 10-3).

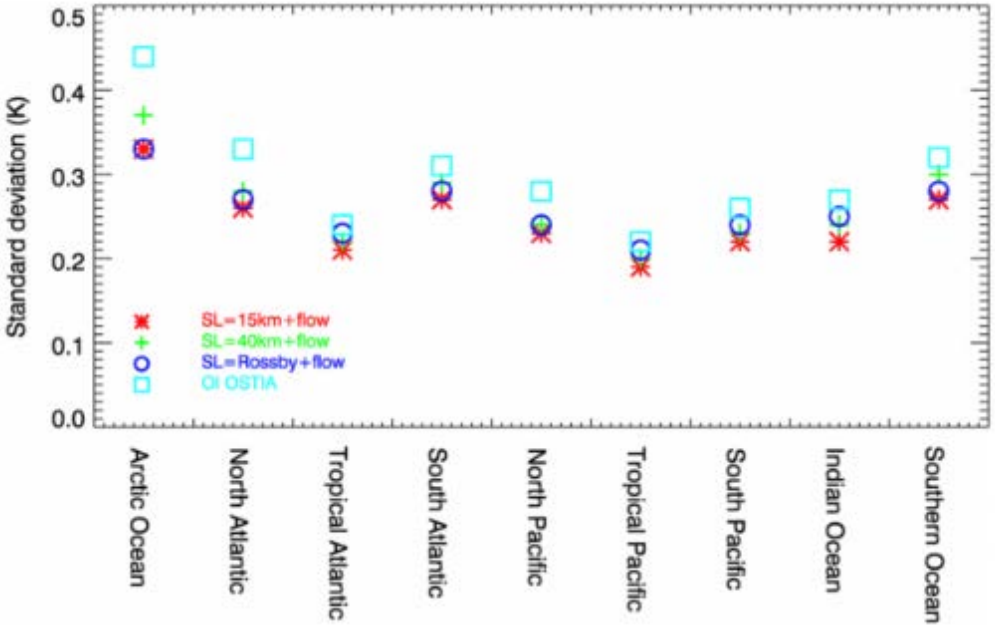

Fig. 10-3. Standard deviations between selected night-time satellite observations and the NEMOVAR and OI OSTIA analyses, for basis as labelled. Squares are the OSTIA system as used in the previous SST CCI analysis, and the red stars are the system now used for v2. Other symbols refer to other configurations tried experimentally.

In terms of the SST fields produced, the impact is best seen looking, again, at SST gradients. The improved feature resolution is shown in figure 10-4 by the presence of stronger gradients, associated with mesoscale variability that was in the former system suppressed by greater smoothing.

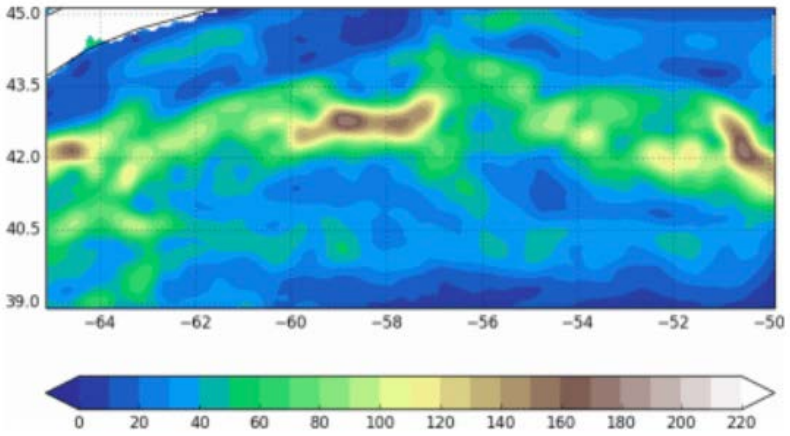

a.

b.

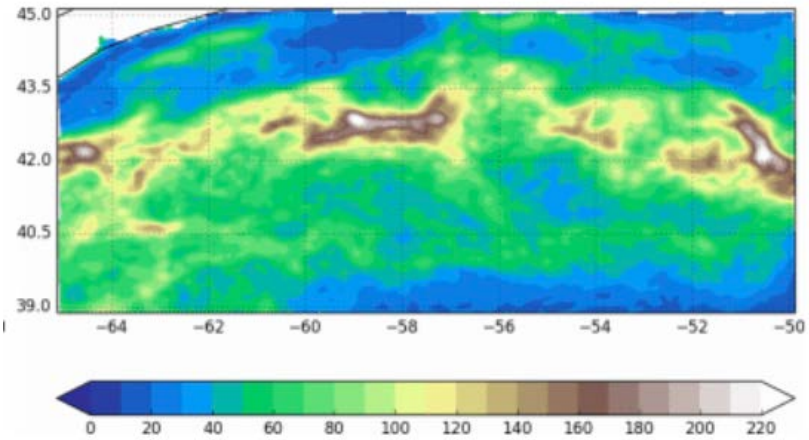

Fig 10-4. Total SST gradient from two analysis versions. (a) The configuration for SST CCI v1, (b) the configuration for SST CCI v2. The plots show the Jan-Mar 2017 averaged horizontal SST gradients in mK km^{-1} for the Gulf Stream region (axes are labelled with longitudes and latitudes).

10.4 Future enhancements

Given the performance of the L4 analysis illustrated above, further improvement of the SST aspect of the analysis system is not foreseen under SST CCI funding towards v3. Work will be done to manually inspect and improve sea ice concentration data (sourced from the sea ice CCI). Moreover, any progress in the analysis system made through other funding and having reached maturity will be made available to SST CCI v3 by agreement.